HZDR-069

Wissenschaftlich-Technische Berichte
HZDR-069 2016 · ISSN 2191-8708

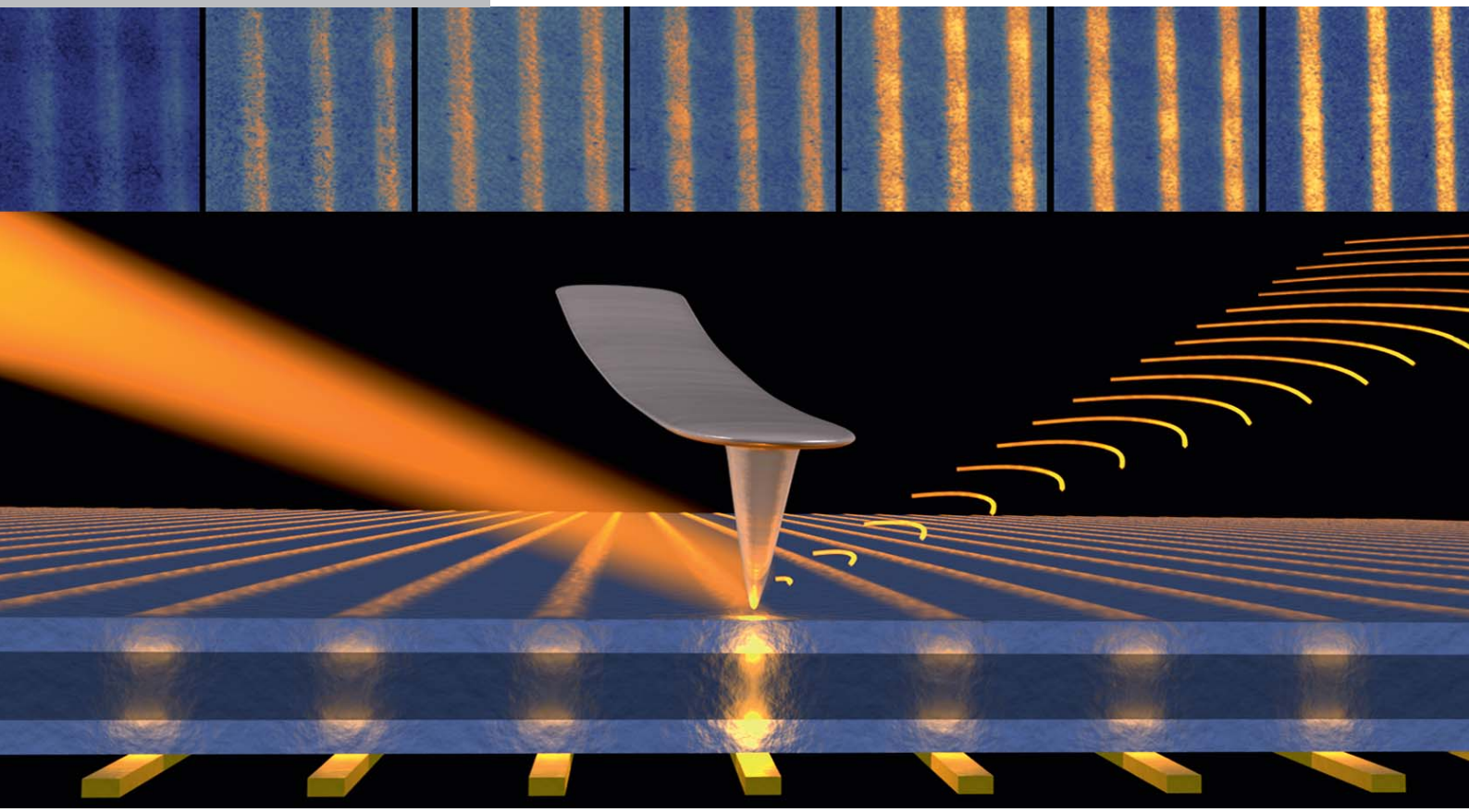

ANNUAL REPORT 2015

INSTITUTE OF ION BEAM PHYSICS AND MATERIALS RESEARCH

HZDR

HELMHOLTZ
ZENTRUM DRESDEN
ROSSENDORF

Wissenschaftlich-Technische Berichte
HZDR–069

Annual Report 2015

Institute of Ion Beam Physics and Materials Research

Editors

J. Fassbender, V. Heera,
M. Helm, P. Zahn

HZDR

HELMHOLTZ
ZENTRUM DRESDEN
ROSSENDORF

Cover Picture

The cover picture illustrates scanning near-field infrared microscopy (SNIM) through a so-called superlens. The superlens is based on a doped GaAs layer, which exhibits a negative permittivity below the plasma frequency. The top row shows images of 36x36 μm^2 of a buried nanostructure formed by gold stripes taken at different infrared wavelengths. In a narrow spectral region around a wavelength of 20 micrometers the image exhibits the best visibility and the highest spatial resolution, far below the diffraction limit. Advantageously, the spectral position of the resonance can be tailored by adjusting the doping level of the GaAs layer.

Image: HZDR / M. Fehrenbacher

For further information see:

M. Fehrenbacher et al., Nano Letters **15**, 1057 (2015),
reprinted at pp. 11–15 of this Annual Report.

Print edition: ISSN 2191-8708
Electronic edition: ISSN 2191-8716

urn:nbn:de:bsz:d120-qucosa-207048
www.hzdr.de/publications/Publ-23926
Published by Helmholtz-Zentrum Dresden - Rossendorf e.V.

This report is also available at https://www.hzdr.de/FWI.

Helmholtz-Zentrum Dresden - Rossendorf e.V.
Institute of Ion Beam Physics and Materials Research
Bautzner Landstraße 400
01328 Dresden
Germany

Directors	Prof. Dr. M. Helm	Prof. Dr. J. Faßbender
Phone	+ 49 (351) 260 2260	+ 49 (351) 260 3096
Fax	+ 49 (351) 260 3285	+ 49 (351) 260 3285
Email	m.helm@hzdr.de	j.fassbender@hzdr.de

www.hzdr.de/FWI

Preface by the directors

After the successful evaluation in 2015 we started research and further development of our large-scale facilities, in particular the Ion Beam Center (IBC), in the framework of Helmholtz's Programme-oriented Funding scheme (POF) which coordinates scientific cooperation on a national and international scale. Most of our activities are assigned to the Helmholtz program "**From Matter to Materials and Life**" within the research area "Matter", in cooperation with several other German Helmholtz Centers. Our in-house research is performed in three so-called research themes, as depicted in the schematic below. What is missing there for simplicity is a minor part of our activities in the program "Nuclear Waste Management and Safety" within the research area "Energy".

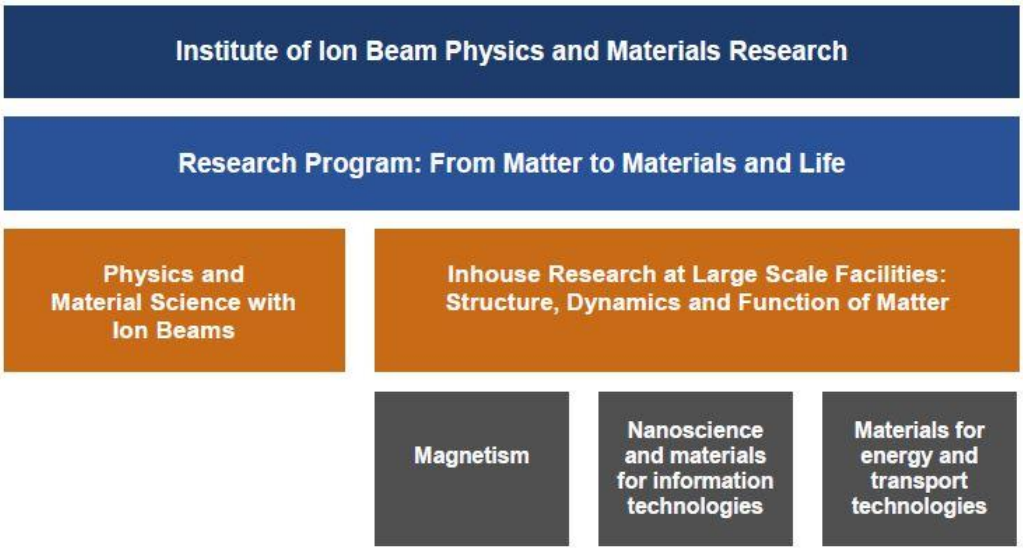

A few highlights which have been published in 2015 are reprinted in this annual report in order to show the variety of the research being performed at the Institute, ranging from self-organized pattern formation during ion erosion or DNA origami patterning, over ferromagnetism in SiC and TiO_2 to plasmonics and THz-spectroscopy of III-V semiconductors. A technological highlight published recently is the demonstration of nanometer scale elemental analysis in a Helium ion microscope, making use of a time-of-flight detector that has been developed at the IBC. In addition to these in-house research highlights, also users of the IBC, in particular of the accelerator mass spectrometry (AMS), succeeded in publishing their research on geomorphology in Nepal in the high-impact journal Science (W. Schwanghart et al., Science **351**, 147 (2015)), which demonstrates impressively the added value of transdisciplinary research at the IBC.

In order to further develop the IBC, we have started in 2015 the design and construction of our new low energy ion nanoengineering platform which was highly recommended by the POF evaluators. It will consist of two-dimensional materials synthesis and modification, high-resolution ion beam analysis and high-resolution electron beam analysis and will come into full operation in 2019.

With respect to personnel the Institute was able to attract Dr. Arkady Krasheninnikov and Dr. Denys Makarov within the high-potential program established by the HZDR. Dr. Krasheninnikov became group leader for atomistic simulations of irradiation-induced phenomena within the IBC; Dr. Denys Makarov is group leader for intelligent materials and devices within the magnetism division. Both have established their groups already, hired several PhD students and postdocs, and started to interact with the other groups and divisions of the Institute. In addition, the HGF Young Investigator

Group “Ion beam processed functional materials for spintronics and photovoltaics” led by Dr. S. Zhou was positively evaluated and is now a permanently established group within the semiconductor materials division.

We are very pleased that the research on magnetic domain walls as reconfigurable spin-wave nanochannels by Dr. Helmut Schultheiß, Andreas Henschke, Dr. Thomas Sebastian and Kai Wagner was honored by the HZDR-Forschungspreis 2015, which demonstrates nicely that focused work is already recognized within a short term.

Another great success in 2015 was the approval of the EU-ICT project “Ion-Irradiation-Induced Si Nanodot Self-Assembly for Hybrid SET-CMOS Technology” (IONS4SET) coordinated by Dr. J. von Borany and Dr. K.-H. Heinig from our institute. This collaborative project funded by the European Union with 4 million Euro brings together scientists from HZDR, CEA-LETI Grenoble, France, CSIC Madrid, Spain, the Fraunhofer Institute IISB in Erlangen, the Institute for Microelectronics and Microsystems IMM at the CNR in Italy and the University of Helsinki in Finland.

Last but not least, we organized in 2015 the first “German THz Conference” held in the “Dreikönigskirche” with over 120 participants, among them some prominent international invited speakers. Remarkably, 13 companies sponsored this very successful event, which from now on will be held every two years.

Finally, we would like to cordially thank all partners, friends, and organizations who supported our progress in 2015. Special thanks are due to the Executive Board of the Helmholtz-Zentrum Dresden-Rossendorf, the Minister of Science and Arts of the Free State of Saxony, and the Minister of Education and Research of the Federal Government of Germany. Numerous partners from universities, industry and research institutes all around the world contributed essentially, and play a crucial role for the further development of the institute. Last but not least, the directors would like to thank again all IIM staff for their efforts and excellent contributions in 2015.

Prof. Manfred Helm Prof. Jürgen Fassbender

Contents

Selected Publications

Statistics

Selected Publications

Image: HZDR / SIMIT-CAS

Copyright remarks

The following journal articles are reprinted with kind permission from:

Fehrenbacher, M.; Winnerl, S.; Schneider, H.; Döring, J.; Kehr, S.; Eng, L.; Huo, Y.; Schmidt, O.; Yao, K.; Liu, Y.; Helm, M.
Plasmonic Superlensing in Doped GaAs
Nano Letters, Vol. 15, pp. 1057 – 1061

DOI: 10.1021/nl503996q

Ou, X.; Heinig, K.-H.; Hübner, R.; Grenzer, J.; Wang, X.; Helm, M.; Fassbender, J.; Facsko, S.
Faceted nanostructure arrays with extreme regularity controlled vacancy by vacancy
Nanoscale, Vol. 7, pp. 18928 – 18935

DOI: 10.1039/c5nr04297f

Wang, Y.; Liu, Y.; Wang, G.; Anwand, W.; Jenkins, C.; Arenholz, E.; Munnik, F.; Gordan, O.; Salvan, G.; Zahn, D. R. T.; Chen, X.; Gemming, S.; Helm, M.; Zhou, S.
Carbon *p* Electron Ferromagnetism in Silicon Carbide
Scientific Reports, Vol. 5, 8999-1 – 8999-5

DOI: 10.1038/srep08999

Teschome, B.; Facsko, S.; Gothelf, K.V.; Keller, A.
Alignment of Gold Nanoparticle-Decorated DNA Origami Nanotubes: Substrate Prepatterning versus Molecular Combing
Langmuir, Vol. 31, pp. 12823 – 12829

DOI: 10.1021/acs.langmuir.5b02569

Yildirim, O.; Cornelius, S.; Butterling, M.; Anwand, W.; Wagner, A.; Smekhova, A.; Fiedler, J.; Böttger, R.; Bähtz, C.; Potzger, K.
From a non-magnet to a ferromagnet: Mn^+ implantation into different TiO_2 structures
Applied Physics Letters, Vol. 107, pp. 242405-1 – 242405-4

DOI: 10.1063/1.4938069

Eßer, F.; Drachenko, O.; Patanè, A.; Ozerov, M.; Winnerl, S.; Schneider, H.; Helm, M.
Direct determination of the electron effective mass of GaAsN by terahertz cyclotron resonance spectroscopy
Applied Physics Letters, Vol. 107, pp. 062103-1 – 062103-4

DOI: 10.1063/1.4928623

Klingner, N.; Heller, R.; Hlawacek, G.; von Borany, J.; Notte, J.; Huang, J.; Facsko, S.
Nanometer scale elemental analysis in the helium ion microscope using time of flight spectrometry
arXiv:1510.04594v3 [physics.ins-det]

also published in Ultramicroscopy, Vol. 162, pp. 91 – 97 (2016)

NANO LETTERS
Letter
pubs.acs.org/NanoLett

Plasmonic Superlensing in Doped GaAs

Markus Fehrenbacher,*[,†,‡] Stephan Winnerl,*[,†] Harald Schneider,[†] Jonathan Döring,[‡] Susanne C. Kehr,[‡] Lukas M. Eng,[‡] Yongheng Huo,[§] Oliver G. Schmidt,[§] Kan Yao,[∥] Yongmin Liu,[∥] and Manfred Helm[†,‡]

[†]Helmholtz-Zentrum Dresden-Rossendorf, Institute of Ion Beam Physics and Materials Research, Bautzner Landstraße 400, 01328 Dresden, Germany

[‡]Institut für Angewandte Physik, TU Dresden, 01062 Dresden, Germany

[§]Institute for Integrative Nanosciences, IFW Dresden, Helmholtzstrasse 20, 01069 Dresden, Germany

[∥]Department of Electrical and Computer Engineering, Northeastern University, Boston, Massachusetts 02115, United States

ABSTRACT: We demonstrate a semiconductor based broadband near-field superlens in the mid-infrared regime. Here, the Drude response of a highly doped n-GaAs layer induces a resonant enhancement of evanescent waves accompanied by a significantly improved spatial resolution at radiation wavelengths around $\lambda = 20$ μm, adjustable by changing the doping concentration. In our experiments, gold stripes below the GaAs superlens are imaged with a $\lambda/6$ subwavelength resolution by an apertureless near-field optical microscope utilizing infrared radiation from a free-electron laser. The resonant behavior of the observed superlensing effect is in excellent agreement with simulations based on the Drude−Lorentz model. Our results demonstrate a rather simple superlens implementation for infrared nanospectroscopy.

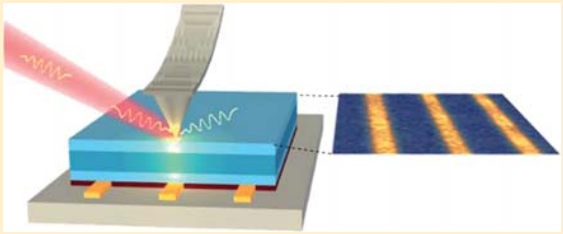

KEYWORDS: *Superlens, diffraction limit, surface plasmons, near-field microscopy, semiconductor*

In classical optical microscopy, spatial resolution is constrained by the wavelength of the applied radiation, limited by diffraction. In 2000, Pendry proposed that a negative refractive-index material[1] could act as a perfect lens,[2] which not only focuses propagating waves but in addition reconstructs information contained in the evanescent fields of an object, thereby creating an image with a resolution beyond the diffraction limit. Pendry also showed that in the near-field regime, negative permittivity alone is sufficient to realize a superlens to recover details on a subwavelength scale, which initiated a number of related experiments. While thin planar silver sheets have been demonstrated to be promising candidates for superlens-based UV nanophotolithography,[3−5] near-field investigations of SiC,[6] perovskites[7,8] and graphene[9] reveal imaging capabilities beyond the diffraction limit at infrared wavelengths. Depending on the material, the spectral position and bandwidth of superlensing is determined by its plasma frequency[3−5,9] and phonon resonances.[6−8] Consequently, accessible wavelengths are restricted by the limited availability of suitable materials. Various approaches have been proposed to overcome these restrictions. On the one hand, multilayered systems with different phonon resonances[10] and the concept of an "unmatched superlens"[11] promise to broaden the operation wavelength range of a superlens. On the other hand, the superlensing wavelength can be tailored by manipulating the electronic properties and, thus, the permittivity of a material. Correspondingly it has been suggested to use doped graphene[12] or metal-dielectric composites[13] as frequency-adjustable subdiffractive imaging systems, continuously covering the visible and infrared range by controlling the respective plasma frequencies. Especially relevant to this work, semiconductors have been suggested to be exploited as plasmonic devices[14−17] where the operational spectral range can be adapted by changing the doping level. However, a superlens consisting of doped semiconductor has not been demonstrated yet.

Our approach to realize a spectrally adjustable plasmonic superlens in the mid- and far-infrared is to use Si-doped GaAs, taking advantage of precisely controllable charge-carrier concentration by standard semiconductor fabrication techniques. Here, the electron density determines the plasma frequency of a conductive layer which in turn determines the superlensing wavelength. In this article, we evidence the performance of such a device by imaging gold stripes below the superlens with a scattering-type scanning near-field optical microscope (s-SNOM)[18] combined with a free-electron laser (FEL).[7,8,19−21] The observed enhancement of both the near-field signal and the spatial resolution is consistent with theoretical considerations based on the Drude−Lorentz model, taking into account free electrons and optical phonons.[22]

Superlensing for evanescent electric fields is related to the excitation of strongly localized surface polariton modes[23] at the interface between two media, A and B, with permittivities of

Received: October 17, 2014
Revised: January 8, 2015
Published: January 13, 2015

DOI: 10.1021/nl503996q
Nano Lett. 2015, 15, 1057−1061

same value and opposite sign,[24] that is, $\mathrm{Re}(\varepsilon_A) = -\mathrm{Re}(\varepsilon_B)$. In our case, subwavelength resolved images arise due to coupled surface plasmon polariton modes confined at the interfaces between a doped semiconductor layer (B) and its neighboring intrinsic layers (A), enhancing the transfer of evanescent waves through the multilayer slab. This superlens structure (cf. Figure 1) consists of a highly n-doped (Si) GaAs film of thickness d sandwiched between two undoped layers of thickness $d/2$. Two superlens samples were prepared with a total thickness $2d$ of 400 and 800 nm, respectively. Additionally, a reference sample consisting of an intrinsic 400 nm thick GaAs layer was investigated. The object to be imaged is a periodic arrangement of gold stripes of 2 μm width at a spacing of 10 μm. All samples were prepared in the following way: At first, a 100 nm thick $Al_{0.9}Ga_{0.1}As$ etch-stop layer was grown by molecular beam epitaxy (MBE) on a GaAs substrate, followed by the three GaAs layers (A−B−A) of the superlens. On top of the last intrinsic layer, the gold stripes were patterned by optical lithography, gold deposition, and lift-off processing. Subsequently, the entire system was glued top-down by instant adhesive onto high-resistive silicon for the ease of handling. Then the GaAs substrate was etched away by citric acid down to the $Al_{0.9}Ga_{0.1}As$ etch stop, which was finally removed by concentrated HCl.

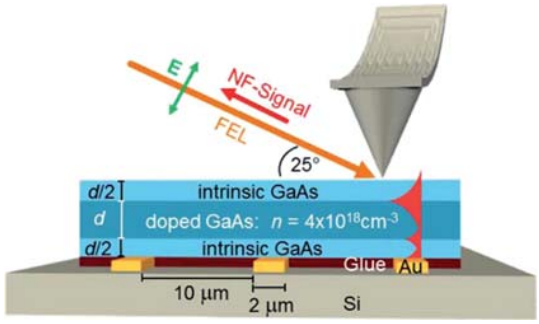

Figure 1. s-SNOM investigation of a GaAs superlens: an AFM tip is illuminated by p-polarized FEL radiation, the scattered light yielding information about the local near-field (NF) of the sample. Gold stripes (width 2 μm, spacing 10 μm) are imaged through the three-layered system. For the investigated samples, the layer thickness d equals 200 and 400 nm, respectively. The red feature in the sample indicates the distribution of the evanescent field along the surface normal in a similar manner as in ref 6.

In order to deduce the dielectric function of the superlens layers, Fourier transform infrared spectroscopy (FTIR) was performed in reflection geometry on the MBE grown samples prior to the lithography step (i.e., on the layer sequence GaAs/n-GaAs/GaAs/AlGaAs on GaAs substrate). Within a large part of the infrared electromagnetic spectrum, the relative permittivity ε can be described well by the Drude−Lorentz model[22]

$$\varepsilon(\omega) = \varepsilon_{\mathrm{optic}} - \frac{(\varepsilon_{\mathrm{static}} - \varepsilon_{\mathrm{optic}})\omega_{\mathrm{TO}}^2}{\omega^2 - \omega_{\mathrm{TO}}^2 + i\omega\gamma_{\mathrm{ph}}} - \frac{\varepsilon_{\mathrm{optic}}\omega_{\mathrm{p}}^2}{\omega^2 + i\omega\gamma_{\mathrm{el}}}$$

where $\varepsilon_{\mathrm{static}}$ and $\varepsilon_{\mathrm{optic}}$ are the static and high-frequency dielectric constants, respectively. While values for the transverse optical phonon frequency ω_{TO} and the phonon damping γ_{ph} are well known from the literature,[22] the plasma frequency ω_{p} (and thus the charge carrier density n) and the electron damping γ_{el} of the doped GaAs layer were determined by fitting a Drude−Lorentz based multilayer reflectivity simulation to the FTIR data. This results in $n = 4 \times 10^{18}$ cm^{-3} and $\gamma_{\mathrm{el}} = 100$ cm^{-1}. In addition, n was confirmed by a Hall measurement in van der Pauw geometry. Using these values the infrared permittivities $\varepsilon_{\text{n-GaAs}}$ and $\varepsilon_{\mathrm{GaAs}}$ of both the conducting and intrinsic GaAs layers were calculated (cf. Figure 2), which govern the spectral response of the superlens. Although the real part $\mathrm{Re}(\varepsilon)$ of intrinsic GaAs, apart from the Reststrahlen band around $\lambda = 37$ μm, is fairly constant in the infrared, the introduction of electrons results in increasingly negative values for longer wavelengths due to free-carrier absorption (cf. Figure 2a). Superlensing is expected for $\mathrm{Re}(\varepsilon_{\text{n-GaAs}}) = -\mathrm{Re}(\varepsilon_{\mathrm{GaAs}})$, which is the case for our sample at $\lambda \sim 20$ μm (cf. Figure 2a, inset). At this wavelength, the imaginary part $\mathrm{Im}(\varepsilon)$ (cf. Figure 2b) of both intrinsic and doped GaAs is comparibly small corresponding to small dissipation, which is a critical parameter for the performance of a superlens. Please note that the precisely controllable doping level n of GaAs offers the potential to adjust the superlensing wavelength, which increases with decreasing free electron concentration.

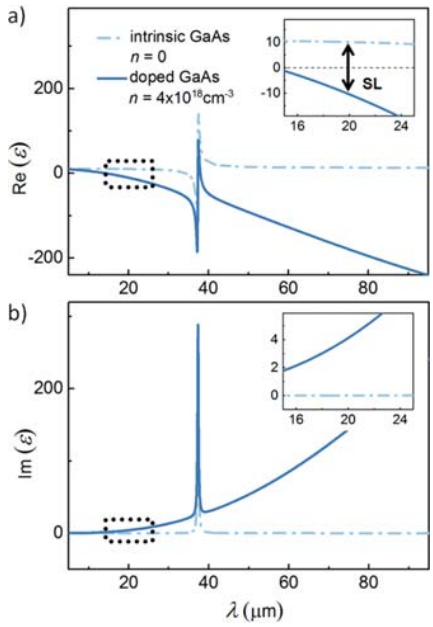

Figure 2. (a) Real part of the dielectric function $\mathrm{Re}(\varepsilon)$ of intrinsic and doped GaAs, as determined by FTIR measurements, fulfilling the superlensing condition $\mathrm{Re}(\varepsilon_{\text{n-GaAs}}) = -\mathrm{Re}(\varepsilon_{\mathrm{GaAs}})$ at $\lambda \sim 20$ μm (see inset). (b) Imaginary part of the dielectric function $\mathrm{Im}(\varepsilon)$. At the superlensing wavelength $\mathrm{Im}(\varepsilon_{\mathrm{GaAs}}) \sim 0$ and $\mathrm{Im}(\varepsilon_{\text{n-GaAs}}) \sim 4$. The value for phonon damping, $\gamma_{\mathrm{ph}} = 2$ cm^{-1}, is taken from ref 22.

The near-field signal of the gold stripes is recorded by s-SNOM (obtained via noninterferometric detection of the backscattered light), which allows imaging with a resolution far below the diffraction limit.[18] Here, an oscillating atomic force microscope (AFM) tip acts as a scatterer for incoming radiation, where the scattering efficiency is modified by tip−sample interaction. Acting as a small antenna, the tip converts the local near-field of the sample into an accessible far-field signal. Scanning the sample in tapping mode, the oscillation of the tip allows us to separate the near-field signal from the far-field background by lock-in demodulation of the measured

DOI: 10.1021/nl503996q
Nano Lett. 2015, 15, 1057−1061

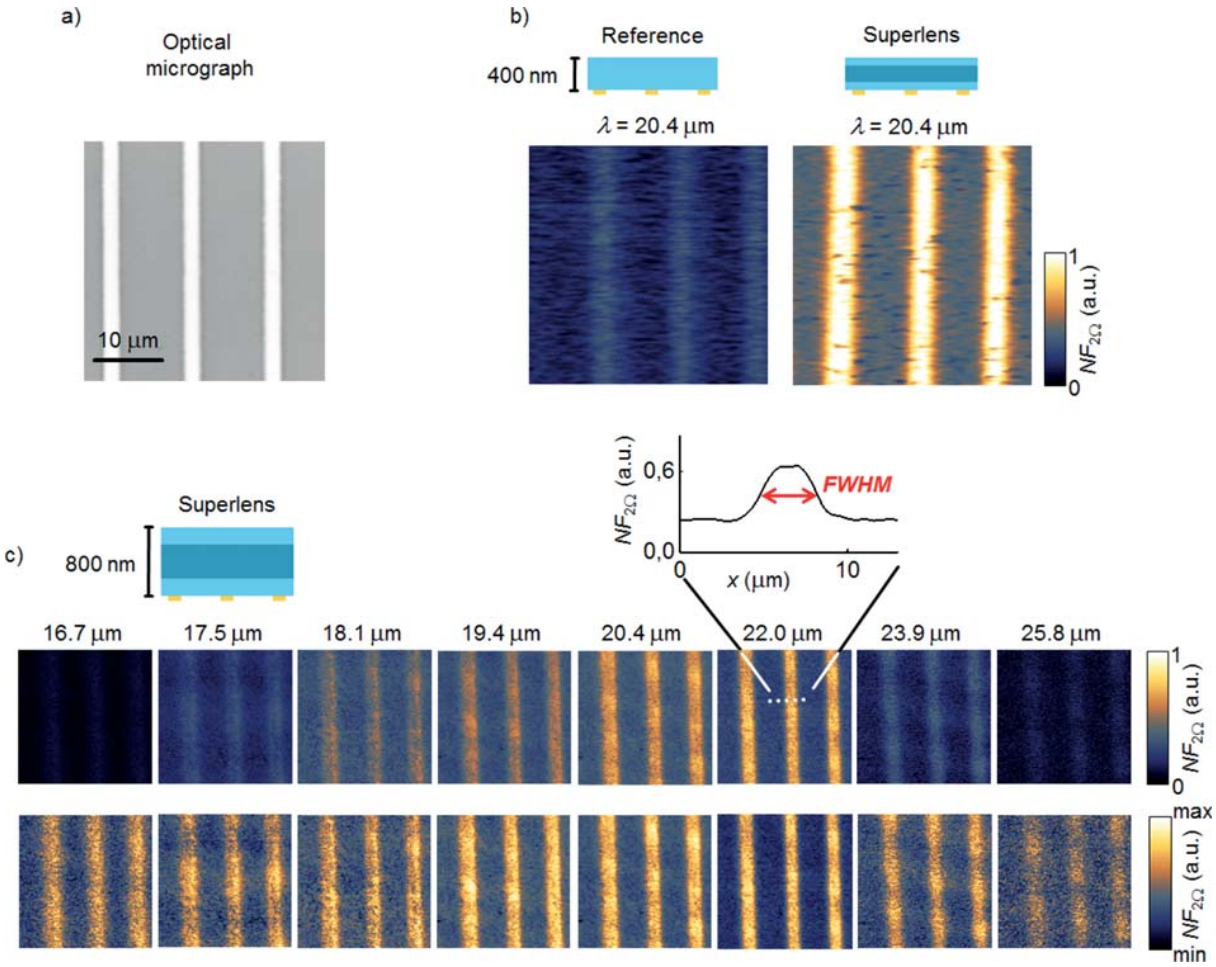

Figure 3. (a) Image of the stripes by optical microscopy for comparison, taken before the pattern was covered by the superlens. (b) Near-field images ($NF_{2\Omega}$) of gold stripes below 400 nm intrinsic GaAs as a reference (left) and below a superlens with the same total thickness, including 200 nm doped GaAs (right). (c) Upper row: near-field images of gold stripes below an 800 nm thick superlens (intrinsic GaAs: 2 × 200 nm, doped GaAs: 400 nm), recorded at radiation wavelengths from λ = 16.7 μm to λ = 25.8 μm. For λ = 22.0 μm a line profile with a full width at half-maximum (fwhm) of 3.4 μm is shown. Bottom row: same measurements but with a full-range color scale applied to each image.

signal at higher harmonics of the cantilever's oscillation frequency Ω.[25] The near-field images in this study were obtained by 2Ω demodulation, denoted as $NF_{2\Omega}$. As a radiation source we employ the widely tunable FEL (radiation wavelength 4–250 μm) at the Helmholtz–Zentrum Dresden–Rossendorf (HZDR). The scattered radiation is detected in backward direction by a mercury–cadmium–telluride (MCT) detector.

In the experiment, we first compare the near-field of the gold-stripe pattern underneath the 400 nm thick superlens and underneath the 400 nm thick intrinsic GaAs reference structure. The measurement was performed at a wavelength of λ = 20.4 μm, which is close to the wavelength where superlensing is expected. As shown in Figure 3b, the stripes are barely visible in the image obtained from the reference sample. In this case, the 400 nm thick intrinsic GaAs layer reduces both the near-field signal and the spatial resolution of the near-field image[26] due to the increased distance between SNOM tip and object. For the doped sample, the signal is highly increased, which provides clear evidence for superlensing. If one did not consider the superlensing effect, one would expect even weaker near-field signals for the sample with the doped layer as compared to the intrinsic reference sample because the doping results in free-carrier absorption that reduces the transmitted field. Nevertheless, absorption is one of the key factors that hinders the formation of a "perfect image". This applies to every superlens, as the requirement of negative permittivity is always accompanied by dissipation. In our case, the 2 μm gold stripes are imaged with an apparent width of about 3 μm, clearly beating the diffraction limit. We emphasize that both for the reference sample and for the sample with superlens, the spatial resolution is not as good as for imaging the objects directly. However, for buried structures, introducing a doped layer into the capping enables us to image with drastically increased contrast while maintaining subwavelength resolution.

Note that the image obtained via the 400 nm thick superlens is not purely induced by the superlensing effect, as can be seen by the nonvanishing near-field in case of the reference structure. In order to suppress this background we increased the thickness of the superlens for further investigations.

The spectral dependence of the superlensing effect was investigated with the superlens sample of doubled thickness (800 nm), as shown in Figure 3c. The upper row depicts near-field signals normalized to laser power, detector response and

DOI: 10.1021/nl503996q
Nano Lett. 2015, 15, 1057–1061

lock-in sensitivity, providing quantitative comparability. The near-field signal is strongest at $\lambda = 22\ \mu$m, clearly decreasing to both sides of the spectrum. In addition, the image is sharpest in this case, while it becomes blurred at shorter and longer wavelengths (cf. Figure 3c, bottom row). A line plot across one stripe reveals a full width at half-maximum (*fwhm*) of 3.4 μm at resonance. Since the width of the stripe itself (2 μm) strongly contributes to the *fwhm*, the actual resolution must be better than 3.4 μm, corresponding to a subwavelength resolution of at least $\lambda/6$. Note that the image of the 400 nm thick superlens (cf. Figure 3b) exhibits a higher near-field signal as compared to the 800 nm thick superlens (cf. Figure 3c) for the same wavelength $\lambda = 20.4\ \mu$m. This can be attributed to less absorption in the thinner layer.

The performance of a near-field superlens can be analyzed by calculating the transmittance T through a sequence of homogeneous dielectric films[27] at normal incidence. Depicted as a function of the tangential wavenumber k_t and radiation wavelength λ, this is often referred to as the transfer function. The transfer function of our GaAs superlens is shown in Figure 4a, assuming a superlens suspended in air. Accordingly, the

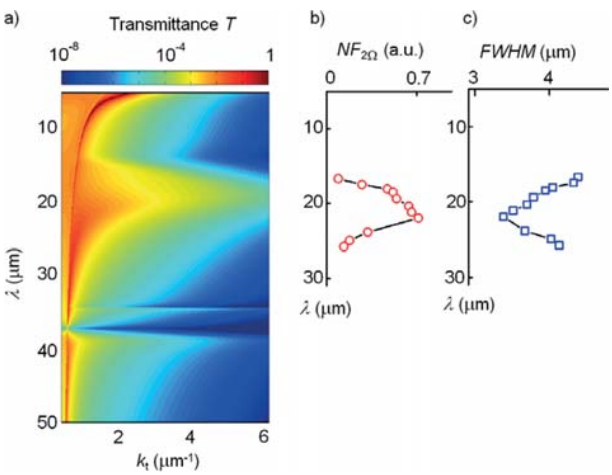

Figure 4. (a) Calculated transfer function T of the GaAs superlens (800 nm total thickness) in the spectral range of interest, plotted in logarithmic scale for better visibility. (b) Experimental result: superlens enhanced near-field signal $NF_{2\Omega}$ on gold stripes and (c) *fwhm* of a stripe's image as a function of radiation wavelength λ.

transmittance of large wavenumbers is resonantly enhanced around $\lambda = 20\ \mu$m, illustrating the increase of imaging quality induced by the superlensing effect. This enhancement is consistent with the simple condition $\mathrm{Re}(\varepsilon_{\text{n-GaAs}}) = -\mathrm{Re}(\varepsilon_{\text{GaAs}})$, which was described above. To relate the transfer function to our experimental findings, we also plot both the near-field signal $NF_{2\Omega}$ at the position of a gold stripe (cf. Figure 4b) and the *fwhm* of the stripe's image versus wavelength λ (cf. Figure 4c). Both the strongest signal and the smallest *fwhm*, according to the best spatial resolution, are observed at $\lambda = 22\ \mu$m, as mentioned above. As can be seen, the resonant behavior is in very good agreement with theory.

The characterization of the subwavelength resolution of a superlens naturally requires a technique that itself provides even higher spatial resolution. In our case, this technique is s-SNOM,[18] featuring a wavelength-independent resolution determined by the radius of the AFM tip (<50 nm). This is much smaller than the wavelength of the infrared radiation and also smaller than the observed resolution of the investigated superlens. Note, however, that the spatial resolution of SNOM significantly degrades with increasing depth for buried objects.[26] In this context, the immediate application potential of our superlens lies in near-field imaging of structures for nanoelectronic applications which are necessarily covered by an intrinsic layer of a certain thickness, for example, to avoid depletion due to surface fields[21,28] or imposed by the penetration depth of ion implantation.[20,29] Here, the introduction of a doped layer turns the intrinsic layer into a superlens at a designed wavelength, enabling near-field studies of buried objects with enhanced sensitivity and better spatial resolution. For instance, nanoscopic imaging of buried quantum dots,[21] doping profiles,[20] and charge carriers in a field-effect transistor[30] can be significantly improved by this concept. Here, the semiconductor-based superlens can enhance the contrast of otherwise blurred images. In many cases, for example, for GaAs based III–V semiconductor compounds, even monolithic integration of the nanoobject and the superlens is possible. For such applications, a broad operation bandwidth may be desirable in order to access as many wavelengths as possible with one and the same structure. Notably, the relative spectral width $\Delta\lambda/\lambda_{SL} \sim 25\%$ (λ_{SL} is the superlensing wavelength) of our plasmonic superlens is significantly larger as compared to previously investigated phonon based systems operating in the mid-infrared, where $\Delta\lambda/\lambda_{SL} < 10\%$ was observed.[6−8] On the one hand, the large bandwidth can be attributed to a slow change of $\mathrm{Re}(\varepsilon(\lambda)/\mathrm{Re}(\varepsilon(\lambda_{SL})$, determining how well the superlensing condition is fulfilled in the spectral proximity of the resonance. On the other hand, damping, which is comparatively large in our case, also broadens the peak in the transfer function. Performing the simulation with artificially reduced $\mathrm{Im}(\varepsilon)$ indicates that the latter aspect is the predominant one (note that large values of $\mathrm{Im}(\varepsilon)$ are accompanied by a decrease of imaging quality). For a deeper understanding, however, a more detailed analysis is required, which is beyond the scope of our study. As mentioned, the center wavelength can easily be tailored by changing the doping level of the intermediate layer. We chose a carrier concentration of $n = 4 \times 10^{18}$ cm^{-3}, which is very close to the upper limit for Si doping of GaAs.[31] This results in a shortest possible superlensing wavelength of about 20 μm. The choice of high n might be surprising at first sight because it leads to large free-carrier absorption, which appears to be undesirable as dissipation strongly impacts the imaging quality of a superlens. However, the critical parameter here is $\mathrm{Im}(\varepsilon)$ *at the superlensing wavelength* λ_{SL}. An increase of n has two consequences: On the one hand, it results in larger values of $\mathrm{Im}(\varepsilon)$ at a given wavelength λ. On the other hand, λ_{SL} decreases accompanied by a decrease of $\mathrm{Im}(\varepsilon)$ (cf. Figure 2b). Altogether calculations (not shown) reveal that high n is preferable since the latter effect dominates. Nevertheless, $\mathrm{Im}(\varepsilon)$ does not increase drastically when going to longer λ_{SL} ($\mathrm{Im}(\varepsilon) \sim 4$, 8, and 12 at $\lambda_{SL} = 20$, 90, and 140 μm, respectively). Therefore, we expect that superlensing in doped GaAs can be transferred well into the terahertz region by less doping. In order to explore shorter wavelengths, the concept of a frequency-adjustable plasmonic superlens can easily be realized with alternative systems providing higher plasma frequencies and, therefore, shorter superlensing wavelengths. In particular, it has recently been shown that the plasma wavelength of InAs can be controlled down to ~5 μm, taking advantage of its small effective mass and the feasibility of extremely high doping.[15,16] In addition, the

DOI: 10.1021/nl503996q
Nano Lett. 2015, 15, 1057−1061

spatial resolution of an InAs-based superlens should be better than for GaAs due to its high electron mobility. In the past few years, a lot of effort was put into the search for low-loss plasmonic materials at telecom or even optical wavelengths.[14,17] In the near-infrared, transparent conducting oxides (TCOs) such as aluminum zinc oxide (AZO) or indium tin oxide (ITO) may be suitable as building blocks for spectrally adjustable superlenses, whereas in the optical regime, silver seems to be the best choice.

In summary, we have demonstrated a GaAs superlens, employing a sequence of intrinsic and doped layers to create subwavelength images in a broad mid-infrared spectral range. Best resolution, about one-sixth of the applied wavelength λ, of imaged gold stripes was observed at $\lambda = 22\ \mu$m, which is in very good agreement with the calculated transfer function based on electronic properties of the doped layer extracted from FTIR reflection measurements. This plasmonic superlens with an adaptable operation wavelength is a versatile device to enhance signal and spatial resolution in near-field imaging of buried structures. Furthermore, it may find application in mid-infrared and terahertz devices that exploit plasmonic coupling of the radiation field to small structures.

■ AUTHOR INFORMATION

Corresponding Authors

*E-mail: m.fehrenbacher@hzdr.de. Phone: +49 351 260 3593. Fax: +49 351 260 3285.
*E-mail: s.winnerl@hzdr.de.

Notes

The authors declare no competing financial interest.

■ ACKNOWLEDGMENTS

We gratefully acknowledge the funding by the German Ministry of Education and Research (BMBF; Grant 05K10BRA and 05K10ODB). We also thank the whole ELBE team for their dedicated support. Special credit goes to Claudia Neisser and Jan Fiedler for preparation and characterization of the samples, respectively.

■ REFERENCES

(1) Veselago, V. G. *Sov. Phys. Uspekhi* **1968**, *10*, 509−514.
(2) Pendry, J. B. *Phys. Rev. Lett.* **2000**, *85*, 3966−3969.
(3) Melville, D. O. S.; Blaikie, R. J.; Wolf, C. R. *Appl. Phys. Lett.* **2004**, *84*, 4403−4405.
(4) Fang, N.; Lee, H.; Sun, C.; Zhang, X. *Science* **2005**, *308*, 534−537.
(5) Liu, H.; Wang, B.; Ke, L.; Deng, J.; Chum, C. C.; Teo, S. L.; Shen, L.; Maier, S. A.; Teng, J. *Nano Lett.* **2012**, *12*, 1549−1554.
(6) Taubner, T.; Korobkin, D.; Urzhumov, Y.; Shvets, G.; Hillenbrand, R. *Science* **2006**, *313*, 1595.
(7) Kehr, S. C.; Yu, P.; Liu, Y. M.; Parzefall, M.; Khan, A. I.; Jacob, R.; Wenzel, M. T.; von Ribbeck, H.-G.; Helm, M.; Zhang, X.; Eng, L. M.; Ramesh, R. *Opt. Mater. Express* **2011**, *1*, 1051−1060.
(8) Kehr, S. C.; Liu, Y. M.; Martin, L. W.; Yu, P.; Gajek, M.; Yang, S.-Y.; Yang, C.-H.; Wenzel, M. T.; Jacob, R.; von Ribbeck, H.-G.; Helm, M.; Zhang, X.; Eng, L. M.; Ramesh, R. *Nat. Commun.* **2011**, *2*, 249.
(9) Li, P.; Wang, T.; Böckmann, H.; Taubner, T. *Nano Lett.* **2014**, *14*, 4400−4405.
(10) Li, P.; Taubner, T. *Opt. Express* **2012**, *20*, A11787−A11795.
(11) Yang, X.; Liu, Y.; Ma, J.; Cui, J.; Xing, H.; Wang, W.; Wang, C.; Luo, X. *Opt. Express* **2008**, *16*, 19686−19694.
(12) Li, P.; Taubner, T. *ASC Nano* **2012**, *6*, 10107−10114.
(13) Cai, W.; Genov, D. A.; Shalaev, V. M. *Phys. Rev. B* **2005**, *72*, 193101.
(14) West, P. R.; Ishii, S.; Naik, G. V.; Emani, N. K.; Shalaev, V. M.; Boltasseva, A. *Laser Photonics Rev.* **2010**, *4*, 795−808.
(15) Law, S.; Adams, D. C.; Taylor, A. M.; Wasserman, D. *Opt. Express* **2012**, *20*, 12155−12165.
(16) Law, S.; Podolskiy, V.; Wasserman, D. *Nanophotonics* **2013**, *2*, 103−130.
(17) Naik, G. V.; Shalaev, V. M.; Boltasseva, A. *Adv. Mater.* **2013**, *25*, 3264−3294.
(18) Novotny, L.; Stranick, S. J. *Annu. Rev. Phys. Chem.* **2006**, *57*, 303−331.
(19) Kehr, S. C.; Cebula, M.; Mieth, O.; Härtling, T.; Seidel, J.; Grafström, S.; Eng, L. M.; Winnerl, S.; Stehr, D.; Helm, M. *Phys. Rev. Lett.* **2008**, *100*, 256403.
(20) Jacob, R.; Winnerl, S.; Schneider, H.; Helm, M.; Wenzel, M. T.; von Ribbeck, H.-G.; Eng, L. M.; Kehr, S. C. *Opt. Express* **2010**, *18*, 26206−26213.
(21) Jacob, R.; Winnerl, S.; Fehrenbacher, M.; Bhattacharyya, J.; Schneider, H.; Wenzel, M. T.; von Ribbeck, H.-G.; Eng, L. M.; Atkinson, P.; Schmidt, O. G.; Helm, M. *Nano Lett.* **2012**, *12*, 4336−4340.
(22) Blakemore, J. S. *J. Appl. Phys.* **1982**, *53*, R123−R181.
(23) Dionne, J. A.; Sweatlock, L. A.; Atwater, H. A.; Polman, A. *Phys. Rev. B* **2005**, *72*, 075405.
(24) Korobkin, D.; Urzhumov, Y.; Shvets, G. *J. Opt. Soc. Am. B* **2006**, *23*, 468−478.
(25) Knoll, B.; Keilmann, F. *Opt. Commun.* **2000**, *182*, 321−328.
(26) Krutokhvostov, R.; Govyadinov, A. A.; Stiegler, J. M.; Huth, F.; Chuvilin, A.; Carney, P. S.; Hillenbrand, R. *Opt. Express* **2012**, *20*, 593−600.
(27) Born, M.; Wolf, E. *Principles of Optics*, 7th ed.; Cambridge University Press: New York, 1999.
(28) Buchwald, W. R.; Cleary, J. W.; Hendrickson, J. *Appl. Phys. Lett.* **2012**, *100*, 051110.
(29) Brice, D. K. *Appl. Phys. Lett.* **1970**, *16*, 103−106.
(30) Huber, A. J.; Keilmann, F.; Wittborn, J.; Aizpurua, J.; Hillenbrand, R. *Nano Lett.* **2008**, *8*, 3766−3770.
(31) Neave, J. H.; Dobson, P. J.; Harris, J. J.; Dawson, P.; Joyce, B. A. *Appl. Phys. A: Mater. Sci. Process.* **1983**, *32*, 195−200.

DOI: 10.1021/nl503996q
Nano Lett. 2015, 15, 1057−1061

Nanoscale

PAPER

View Article Online
View Journal | View Issue

Cite this: *Nanoscale*, 2015, **7**, 18928

Faceted nanostructure arrays with extreme regularity by self-assembly of vacancies

Xin Ou,*[a,b] Karl-Heinz Heinig,[a] René Hübner,[a] Jörg Grenzer,[a] Xi Wang,[b] Manfred Helm,[a,c] Jürgen Fassbender[a,c] and Stefan Facsko*[a]

Received 28th June 2015,
Accepted 18th August 2015

DOI: 10.1039/c5nr04297f

www.rsc.org/nanoscale

Semiconductor quantum dots and wires are important building blocks for future electronic and opto-electronic devices. The common way of producing semiconductor nanostructures is by molecular beam epitaxy (MBE). In this additive growth process atoms are deposited onto crystalline surfaces and self-assemble into 3D structures. Here we present a subtractive process, in which surface vacancies are created by ion impacts. On terraces of crystalline surfaces their nucleation forms depressions which coarsen and finally lead to a self-organized 3D morphology. It is shown that this kind of spontaneous pattern formation is inherent to the ion induced erosion process on crystalline surfaces and is analogous to 3D growth by MBE. However, novel facets are found due to slightly different energetics and kinetics of ad-atoms and surface vacancies, especially at Ehrlich–Schwoebel step-edge barriers. Depending on the crystal orientation, three-fold, four-fold, six-fold symmetry, as well as extremely regular periodic nano-grooves can be produced on different orientations of group IV (Si, Ge) and III–V (GaAs, InAs) semiconductors.

1. Introduction

High-throughput mass production of nanostructure arrays with extreme regularity by self-assembly and self-organization has been a topic of intense research in the last few years. The interest in large-areas of crystalline structures is manifold, from building blocks for electronics[1] and opto-electronics[2] to catalytic surfaces with increased efficiency.[3] Prominent examples of self-assembled nanostructures are found in molecular beam epitaxy (MBE),[4–6] where the growth of 3D nanostructures proceeds by deposition of atoms onto the surface (Fig. 1a). In homoepitaxy these nanostructures are formed due to kinetic restrictions of the diffusing ad-atoms. To cross a terrace step downwards an additional barrier, the Ehrlich–Schwoebel (ES) barrier has to be overcome leading to reflection of ad-atoms and thus to an effective uphill diffusion current on a vicinal surface. This so-called Villain instability has been identified as the main process for 3D growth of structures during MBE.[6]

Ion irradiation, on the other hand, is frequently used to etch materials by sputtering[7] and can be easily scaled up to 300 mm wafer size. It can also be employed for nano-patterning surfaces by a self-organized, bottom-up approach.[8] The resulting patterns are periodic ripple structures with periodicities down to 15 nm[9] and can achieve quite high order as in the case of Si and Ge irradiated with 26 keV Au^- ions.[10] Such ripple patterns can be applied as templates for growing nanostructured thin films with strong anisotropic magnetic or optical properties.[11] Therefore, a broad interest exists for this simple, high-throughput and inexpensive technology for nanopatterning surfaces. The main drawback of this method is that semiconductors are amorphized when ion irradiation is performed at room temperature.[12] At elevated temperature, however, ion induced interstitials and vacancies are mobile enough to recombine or to reach the surface before a new ion hits the same region. Thus ion irradiation performed at temperatures higher than the recrystallization temperature prevents amorphization and leads to an additional surface instability due to the ES barrier for surface vacancies.[13–20] Accordingly, in analogy to the case under growth conditions, this kind of surface instability leads to the formation of 3D nanostructures (Fig. 1a). Vacancies which are created by the ion impacts during irradiation, nucleate and coarsen to form pits that grow inside the surface.[13] The formation of such structures has firstly been observed on metal surfaces, which remain

[a]Helmholtz-Zentrum Dresden-Rossendorf, Institute of Ion Beam Physics and Materials Research, Bautzner Landstr. 400, 01328 Dresden, Germany. E-mail: s.facsko@hzdr.de
[b]State Key Laboratory of Functional Material for Informatics, Shanghai Institute of Microsystem and Information Technology, Chinese Academy of Sciences, Shanghai 200050, China. E-mail: ouxin@mail.sim.ac.cn
[c]Technische Universität Dresden, 01062 Dresden, Germany

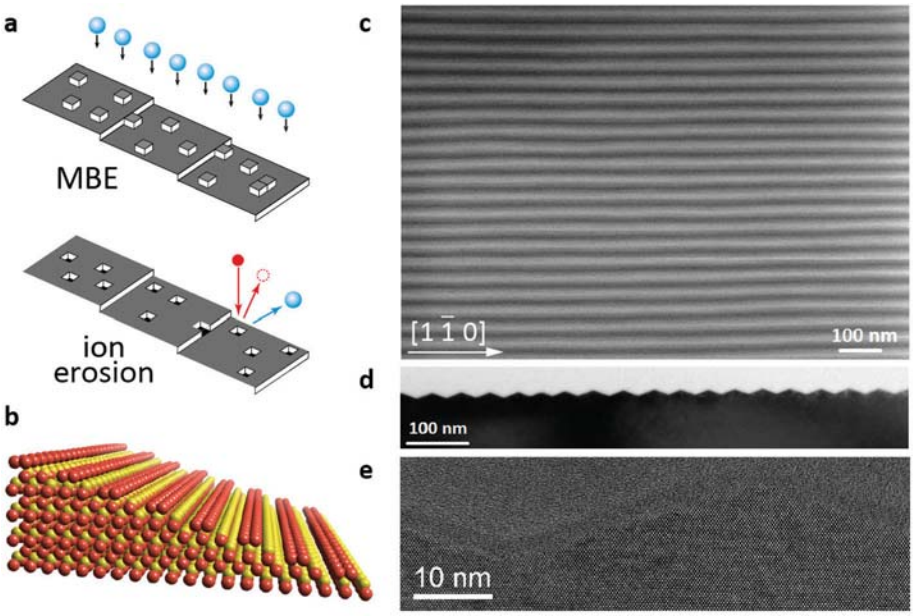

Fig. 1 Regular nanowire patterns on GaAs(001) produced by low-energy ion irradiation. (a) Schematic illustration of the symmetry between growth by ad-atom deposition in MBE and ion erosion by vacancy creation. Due to the step-edge barrier for ad-atoms (ad-vacancies) nucleation and growth of islands (depression) lead to 3D morphologies. (b) A (115) surface of the GaAs with Ga dimer rows along the [1$\bar{1}$0] direction, which is the direction of the grooves. (c) SEM images of highly-ordered nanogroove patterns formed on GaAs (001) surfaces aligned along the [1$\bar{1}$0] direction after 1 keV Ar^+ irradiation at normal incidence for 130 min at 410 °C. (d) and (e) Cross-sectional TEM images of nanogroove pattern on GaAs(001).

crystalline even at room temperature, due to their high diffusion and non-covalent bonding.[14–16]

Recently, we have observed regular, dense patterns of inverse pyramids on Ge(001) surfaces irradiated by high fluence 1 keV Ar^+ at temperature above 250 °C.[21] These patterns exhibit {105} facets and strongly resemble mound patterns grown by MBE if they are reversed. Here, we present the formation of nanogrooves on the (001) surface of group III–V semiconductors (GaAs, InAs) with a zinc-blende structure. Although the symmetry of the surface is four-fold, like the (001) surface of Si and Ge, a symmetry-breaking due to the stacking of alternating planes of Ga (In) and As leads to an almost perfect two-fold symmetry of the resulting patterns even under normal incidence. In combination with enhanced ion-induced surface diffusion this symmetry-breaking driving force leads to faceted periodic nanogroove patterns oriented along the [1$\bar{1}$0] direction with the highest degree of regularity observed so far. Similar ripple patterns have been observed recently by irradiation of GaAs with hyperthermal ion beams (30 eV Ar^+), however with much lower regularity.[22] Furthermore, on the (111) surfaces of Si and Ge with diamond structure irradiated with high fluence we found peculiar {123} and {356} facets that have not been observed so far. All of these ion induced patterns can be described by a universal generalized continuum equation[21,23] by defining a non-equilibrium surface free energy with the required symmetry, giving the formation dynamics with the correct roughening and coarsening behavior.

2. Results

For the erosion process an ion source producing a broad beam of low-energy ions is used to irradiate the surface of single crystalline semiconductors. After ion irradiation with fluences of 10^{17}–10^{19} cm^{-2} performed above the recrystallization temperature ordered patterns appear on the surface. Arrays of nanogroove structures with a periodicity of 46 nm are fabricated on GaAs (001) surfaces (Fig. 1c). The orientation of the grooves is always along the [1$\bar{1}$0] direction on GaAs and InAs, *i.e.* the atomic structure of the facets is similar to Fig. 1b. The degree of order of these nanogroove structures is increasing with the irradiation fluence. Cross-sectional transmission electron microscopy (TEM) images perpendicular to the grooves (Fig. 1d and e) also show clearly the faceting and the high degree of ordering of these structures.

Fig. 2a–f present typical patterns on different semiconductor surfaces after ion irradiation performed at normal incidence above the recrystallization temperature. Faceted nanostructures with different orientations and shapes develop, which are, with respect to the surface, reversed to similar structures found by MBE.[24] The periodicity and the shape of the faceted structures can be tuned by the irradiation conditions (temperature and fluence) as well as by using different orientations of the crystalline surfaces, *i.e.* low-index crystal planes or different miscut angles from these planes. The formation of facets can be also concluded from the corresponding two-dimensional (2D) angle distributions[25] (left) and

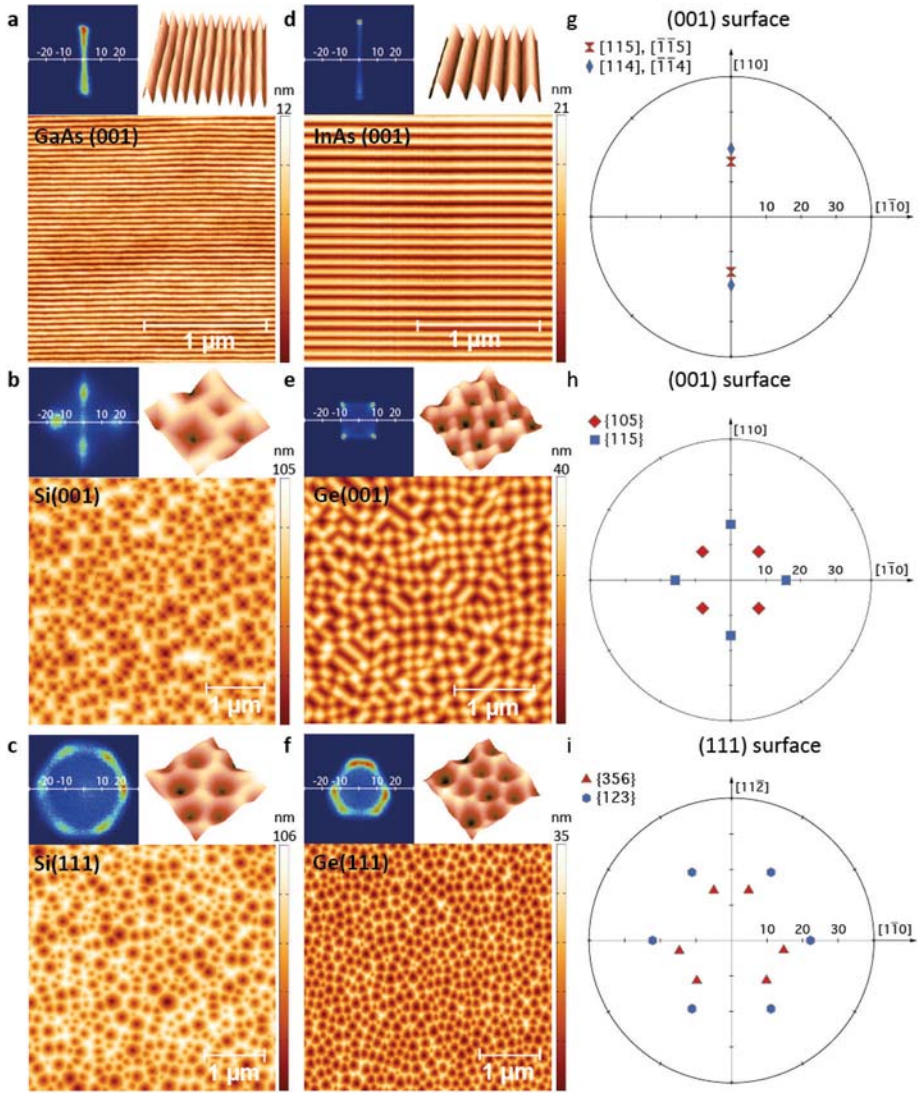

Fig. 2 Atomic force microscopy images of nano-patterns fabricated by ion irradiation on the surfaces of different semiconductors. (a) Nanogrooves on GaAs(001), (b) inverse squared pyramids on Si(001), (c) inverse hexagonal pyramids on Si(111), (d) nanogrooves on InAs(001), (e) inverse squared pyramids on Ge(001), and (f) inverse pyramids on Ge(111), respectively. The two-dimensional angle distributions (left) covering an area of ±30° and the three-dimensional AFM images (right) with scanning size of 500 × 500 nm are shown above the AFM images. The horizontal direction of the AFM images is along the [1$\bar{1}$0] direction. (g–i) Polar plots of the geometrical projections of planes of the diamond lattice with respect to the polar (001) surface (GaAs and InAs), to the (001) surface, and to the (111) surface of the diamond lattice (Si, Ge), respectively. The ion irradiation energy and fluence are 1 keV, 1 × 10^{19} cm^{-2} Ar^+ for (a), (d), (f), 1 keV, 3 × 10^{18} cm^{-2} for (e), and 500 eV, 3 × 10^{18} cm^{-2} Xe^+ for (b) and (c), respectively. The irradiation temperatures are 410 °C for GaAs (a), 320 °C for InAs (d), 530 °C for Si (b, c) and 300 °C for Ge (e, f).

three-dimensional (3D) zoom-in images (right) shown above the AFM images. The symmetry of the patterns reflects the crystal symmetry of the surfaces. For the (001) surface of GaAs (Fig. 2a) and InAs (Fig. 2d) the evolving patterns are periodic, faceted grooves oriented along the [1$\bar{1}$0] direction. This is quite surprising, as the irradiation is performed at normal incidence, thus no asymmetry is imposed by the ion beam. As shown in Fig. 1b, the direction, where dimer rows of Ga (In) are formed due to a (2 × 1) surface reconstruction parallel to the steps,[26] is energetically preferred over the formation of As dimer rows. Furthermore, the [1$\bar{1}$0] direction is also the easy diffusion direction of the Ga (In) atoms.[27] The 2D angle distribution shows two peaks at ±16° and ±19°, respectively. These polar angles can be identified with the {115} (15.79°) and {114} (19.47°) crystal planes, respectively (Fig. 2g).

For Si(001) and Ge(001) a 4-fold symmetry can be identified in Fig. 2b and e. For single-element semiconductors the dimer rows in the [1$\bar{1}$0] and [110] directions consist of the same element, *i.e.* there is no longer a difference in their surface energy, and, consequently, the symmetry breaking disappears. The angle distribution exhibits peaks at 12° for Ge and 16° for Si, which are close to the {105} (11.31°) and {115} (15.79°) planes of the diamond lattice, respectively. The polar plot of the orientation of these facets with respect to the (001) surface

is shown in Fig. 2h. The azimuthal orientation of the structures is different for Si(001) and Ge(001). On Si(001) the structures are oriented along the [110] direction, whereas on Ge (001) the structures align along the [100] direction. This is quite peculiar, because Si and Ge have the same crystal structure and exhibit usually the same (2 × 1) surface reconstruction of the (001) surface. The same facets and the rotation of the pattern by 45° between Si and Ge appear in homoepitaxial growth of Si and Ge as well.[28–31] The emergence of these edges is attributed to an additional barrier at kink sites, similar to the barrier at step edges. However, the origin of the different orientation of the Si and Ge mound facets has not yet been conclusively clarified.

The patterns on the (111) surface of Si (Fig. 2c) and Ge (Fig. 2f) exhibit a different symmetry. On the Ge(111) surface, inverse pyramidal structures with an isotropic distribution are formed. The corresponding 2D angle distribution reveals a three-fold symmetry in the formation of the facets with a polar angle θ of 13°–16°. Noticeable is the development of a double peak structure in the 2D angle distribution separated by an azimuthal angle of ~38°. Inspection of the geometrical projection of the possible facets of the diamond lattice with respect to the (111) surface reveals that the measured angle distribution coincides with the {356} facets. As can be seen in the polar plot of the crystal planes in Fig. 2i, six of these facets have the right polar angle of 15°. They appear as three pairs of two poles with a difference in the azimuthal angle of 38.2° and rotated by 120° to each other, in perfect agreement with the experimentally determined facet angles. These facets are typically not observed in homoepitaxial or heteroepitaxial growth of self-assembled Ge nanostructures. Thus, we can conclude that they are ion induced non-equilibrium stable crystal facets.

On the Si(111) surface inverse hexagonal pyramids are formed during ion irradiation. The structure size of these patterns exhibits a much broader distribution than for the patterns on Ge(111). Thus for Si(111) the wavelength selection at the beginning of the pattern formation is much weaker than for Ge(111). Furthermore, the 2D angle distribution shows six peaks with a polar angle of 21°–23° with a hexagonal symmetry. The facets, which correspond to these values are the {123} crystal planes (22.21°) of the diamond lattice, as can be seen in the geometrical projection of the planes with respect to the (111) surface in Fig. 2i.

Due to the fact that the facets are crystal planes, asymmetric facets can also be formed on surfaces with predefined miscut angles. Fig. 3 shows nanogroove patterns on vicinal GaAs(001) surfaces with miscut angles of 6° and 10° in the [110] direction, respectively. The wavelength of the formed nanogrooves increases from 46 nm on GaAs(001) surfaces without miscut (Fig. 1c) to 65 nm (Fig. 3a) and 90 nm (Fig. 3b) for the surface with 6° and 10° miscut angles, respectively. Fig. 3c and d show the cross-sectional TEM of GaAs(001) with a 10° miscut angle. The shape of these nanogrooves becomes asymmetrical with absolute facet angles to the (100) planes of 20° and 21°, respectively. To keep the same angle of the {114} facet with

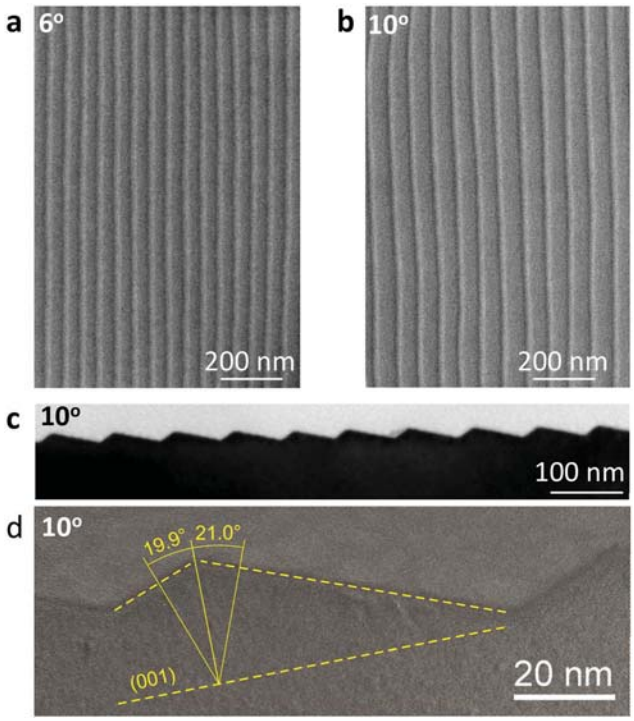

Fig. 3 Ordered, asymmetric nanogroove patterns formed on ion irradiated GaAs(001) surfaces with a miscut angle. (a) SEM image of nanogroove structures formed on GaAs(001) with a miscut angle of 6° and (b) with a miscut angle of 10° towards the [110] direction, respectively. (c, d) Cross-sectional TEM images of the nanogroove patterns. The facet angles with respect to the GaAs(001) plane are indicated.

respect to the (001) surface on both sides one sidewall of the groove is elongated, thus increasing the periodicity of the pattern.[32] These kinds of structures are particularly interesting to be applied as optical grating devices for ultraviolet light.[33]

The formation of 3D nanostructures on ion irradiated surfaces at temperatures above the recrystallization temperature can be regarded as the reverse mechanisms to 3D growth in homoepitaxy.[16,21,24,34,35] The continuous ion irradiation creates a surface vacancy density, which is much higher than the vacancy density under equilibrium conditions, thus driving additional non-equilibrium surface currents. Due to the step edge barriers, the vacancy diffusion currents are "downhill", leading to a surface instability.[6,23,36] The orientation of the patterns along the crystalline directions and the selection of specific facets on the ion irradiated surfaces indicate that the diffusion currents are dominant and sputtering induced effects, like slope/curvature dependent erosion rates and mass redistribution, can be neglected. Thus the continuum equations, which are typically used to describe the morphology evolution on amorphized surfaces under ion irradiation, do not account for the crystal structure and cannot be used here. On binary materials an additional instability is expected[37] due to preferential sputtering of one element changing the stoichiometry of the surface. The coupling of this altered surface layer and the topography can lead to the

formation of periodic patterns as well. However, the crystalline GaAs (InAs) are Ga (In) terminated and no preferential sputtering or segregation of one element has been observed.[38] Furthermore, even at temperatures below the recrystallization temperature we did not observe any pattern formation on GaAs or InAs, thus on these amorphized surfaces ion induced smoothing dominates at normal incidence.

3. Discussion

In order to describe the formation of patterns with the special symmetries on the different surface orientations we generalized and extended the continuum equation used for the Ge (001) case.[21] The evolution of the surface height $h(\mathbf{x},t)$ can be described in a coarse-grain approach by a partial differential equation:

$$\frac{\partial h(x,t)}{\partial t} = -\nabla j + \eta(x,t) = -\nabla(j_{HM} + j_{KPZ} + j_{NE}) + \eta(x,t). \quad (1)$$

The surface current j includes three contributions: $\boldsymbol{j}_{\mathrm{HM}} = \kappa\nabla(\nabla^2 h)$ is the Herring–Mullins surface diffusion, $\boldsymbol{j}_{\mathrm{KPZ}} = \sigma\nabla(\nabla h)^2$ is a nonlinear current (conserved Kardar–Parisi–Zhang term) that breaks the up–down symmetry of the resulting surface, and $\boldsymbol{j}_{\mathrm{NE}}$ is the non-equilibrium surface current that includes the instability due to the ES step edge barrier and the formation of facets. Furthermore, a white noise term $\eta(\boldsymbol{x}, t)$ is included to account for the stochastic nature of the vacancy formation.

Similar to the chemical potential in equilibrium, which determines the vacancy and ad-atom concentrations in thermal equilibrium, a non-equilibrium potential U_{NE} can be defined corresponding to the non-thermal ion induced concentrations of vacancies and ad-atoms. $U_{\mathrm{NE}}(m)$ is proportional to the surface density of atoms and is a function of the local slope $m = \nabla h$. The minimization of the non-equilibrium potential with respect to the surface slope induces a non-equilibrium surface current $j_{\mathrm{NE}}(m) = -\frac{\partial U_{\mathrm{NE}}(m)}{\partial m}$. Due to the high ion induced density of vacancies and their restricted interlayer transport due to the ES barrier the original surface becomes unstable, *i.e.* $U_{\mathrm{NE}}(m)$ has a local maximum at zero slope m = (0,0). The interplay of this instability and the surface diffusion leads to a wavelength selection at the beginning of ion irradiation. At the minima of $U_{\mathrm{NE}}(m)$ the surface current $\boldsymbol{j}_{\mathrm{NE}}$ vanishes leading to a selection of the preferred slopes (facets) at later times.

The different surface patterns in Fig. 4 result from appropriate choices of the non-equilibrium potential $U_{\mathrm{NE}}(\boldsymbol{m})$, reflecting the symmetry of the crystalline surface and possessing minima at the respective, experimentally observed facet angles. In Fig. 4 the chosen non-equilibrium potential and results of the numerical integration of the continuum equation with the corresponding 2D angle distributions are presented. The good agreement between the experimentally observed pattern in Fig. 2 and results of the continuum equation in Fig. 4 indicates that the facet formation is strongly linked to surface currents driven by the minimization of the non-equilibrium effective free energy. In analogy to the determination of the chemical potential by observing the shape of crystals grown under equilibrium conditions, we can thus assess the shape and the first minima of the non-equilibrium potential $U_{\mathrm{NE}}(\boldsymbol{m})$ in the vicinity of the original surface exposed to ion irradiation. It is known that under continuous vacancy creation crystal facets can become unstable and non-equilibrium steady state facets of different orientation can be formed.[39]

4. Methods

Sample preparation

10 mm × 10 mm samples are cut from *epi*-ready Si(001), Ge(001), Ge(111), InAs(001) and GaAs(001) wafers. The ion irradiation is performed in a vacuum chamber with a base pressure of 10^{-8} mbar. The inert gas ions (Ar^+ and Xe^+) are generated by using a Kaufman-type ion source with a single graphite grid extraction of 50 mm in diameter. During irradiation the chamber is backfilled with Ar or Xe gas at 10^{-4} mbar through the ion source which is not differentially pumped. The samples are pasted on a Si plate of 15 mm × 15 mm to avoid metal contamination from the sample holder. The samples are heated by a boron nitride heater behind the sample holder. The surface temperature of the irradiating sample is monitored by a pyrometer operated in the wavelength range of 2–2.8 μm, which was pre-calibrated by using a thermocouple. The optimized irradiation conditions for different semiconductor surfaces are listed in Table 1. Two ion fluences of 3×10^{18} cm^{-2} and 1×10^{19} cm^{-2} are applied in the irradiation process, which corresponds to the irradiation duration of 38 min and 130 min, respectively. The topography of irradiation induced nanopatterns is characterized by atomic force microscopy (AFM) in tapping and non-contact mode and by scanning electron microscopy (SEM). The crystal quality of the nanostructures is investigated by cross-sectional transmission electron microscopy (TEM).

Numerical integration

The numerical integration of the continuum equation (1) for reverse epitaxy is performed on a grid of 500 × 500 points with a spacing of $\Delta x = 1$ and $\Delta t = 0.01$ by a 4th order Runge–Kutta method. The non-equilibrium potentials $U_{\mathrm{NE}}(\boldsymbol{m})$ in Fig. 3 are polynomials up to 8th order in m_x and m_y chosen to have the desired symmetry and minima at slopes corresponding to the observed facets. The non-equilibrium surface currents $\boldsymbol{j}_{\mathrm{NE}}(\boldsymbol{m})$ are calculated analytically from $U_{\mathrm{NE}}(\boldsymbol{m})$ and subsequently used in a Matlab® program to integrate numerically the following continuum equation:

$$\frac{\partial h(x,t)}{\partial t} = -\varepsilon\nabla j_{NE} - \kappa\nabla^2(\nabla^2 h) - \sigma\nabla^2(\nabla h)^2 + \eta(x,t).$$

In every integration step white noise with an amplitude of 0.05 has been added. The coefficients used for the numerical integrations for the different cases in Fig. 4 are as follows:

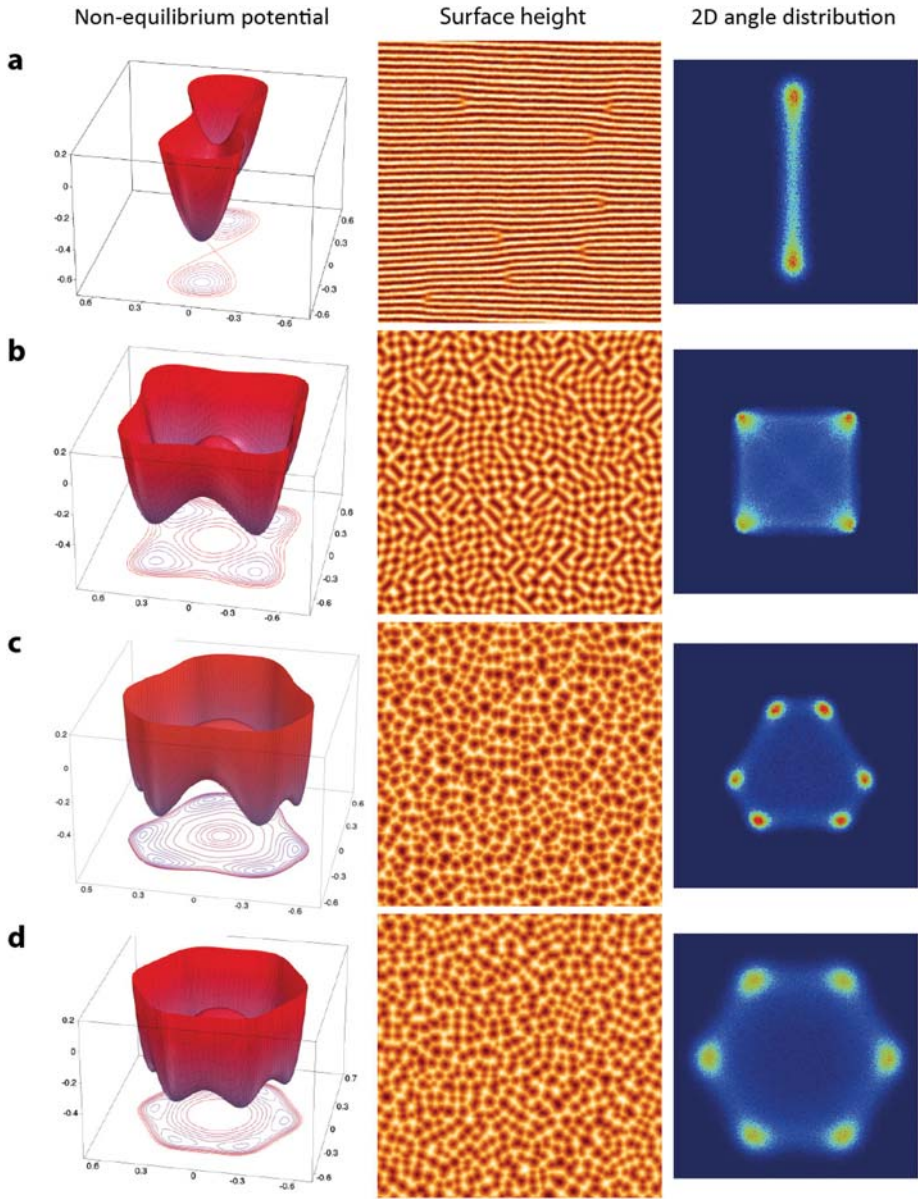

Fig. 4 Non-equilibrium potential, surface height, and 2D angle distributions from numerical integrations of the continuum equation for reverse epitaxy. Non-equilibrium potentials have been chosen to have minima at slopes (m_x, m_y) corresponding to the facet angles and symmetries with (a) two-fold (GaAs(001)), (b) four-fold (Ge(001)), (c) three-fold (Ge(111)), and (d) six-fold (Si(111)) symmetry, respectively.

Table 1 Irradiation parameters for the fabrication of crystalline patterns for different semiconductor surfaces

Materials	Ion species	Ion energy (eV)	Temperature window (°C)
Si(100)	Xe^+	500	480–580
Ge(100)	Ar^+	1000	250–430
Ge(111)	Ar^+	1000	250–380
InAs(100)	Ar^+	1000	180–430
GaAs(100)	Ar^+	1000	200–480

(a) $\varepsilon = 1$, $\kappa = 1$, $\sigma = -1$, (b) $\varepsilon = 1$, $\kappa = 4$, $\sigma = -1$, (c) $\varepsilon = 2$, $\kappa = 4$, $\sigma = -2$, and (d) $\varepsilon = 2$, $\kappa = 4$, $\sigma = -2$. The coefficients for the numerical integration have been chosen solely by the intention to produce patterns with a structure density similar to the AFM images in Fig. 2.

5. Conclusion

In conclusion, we have shown that low-energy ion irradiation of semiconductors above the dynamic recrystallization temperature leads to the spontaneous formation of 3D crystalline structures. To a large extent the here reported erosive pattern formation is analogous to the well-known pattern formation during homoepitaxy and the formation mechanism of these patterns of crystalline structures is universal and can be extended to different crystalline surfaces. These self-assembled

structures form on group III–V semiconductors extremely regular patterns of grooves and on elemental semiconductors patterns of inverse pyramids with specific facets. Depending on the crystal surface orientation different symmetries are found: two-fold in the case of GaAs and InAs due to an additional symmetry-breaking mechanism, three-fold for Ge(111), four-fold for Ge(001) and Si(001) surfaces, and six-fold on Si(111). The present technique of self-organized nanogroove formation on group III–V semiconductors may actually be the one yielding the highest degree of regularity available today without pre-patterning. Due to the parallel formation of the nanopatterns by broad ion beam irradiation, which can be scaled up to 300 mm wafer size, this technique is much faster than serial lithography techniques like e-beam or proton writing techniques. We envision that such highly-ordered nanogroove patterns have a great potential for many applications, *e.g.* as templates for thin film deposition, as catalytic surfaces, and as gratings for UV light.

Acknowledgements

The authors acknowledge support from Deutsche Forschungsgemeinschaft (FOR845). X. O. acknowledges the support from One Hundred Talent Program of CAS and PuJiang Talent Program of Shanghai (15PJ1409700). X. W. acknowledges support by the Creative Research Groups of National Science Foundation of China (Grant Nos. 61321492).

References

1 Y. Huang, X. F. Duan, Q. Q. Wei and C. M. Lieber, *Science*, 2001, **291**, 630–633.
2 E. Dimakis, U. Jahn, M. Ramsteiner, A. Tahraoui, J. Grandal and X. Kong, *Nano Lett.*, 2014, **14**, 2604–2609.
3 H. G. Yang, C. H. Sun, S. Z. Qiao, J. Zou, G. Liu, S. C. Smith, H. M. Cheng and G. Q. Lu, *Nature*, 2008, **453**, 638–644.
4 C. Teichert, *Phys. Rep.*, 2002, **365**, 335–432.
5 J. W. Evans, P. A. Thiel and M. C. Bartelt, *Surf. Sci. Rep.*, 2006, **61**, 1–128.
6 J. J. Villain, *Phys. I*, 1991, **1**, 19–42.
7 M. V. R. Murty, *Surf. Sci.*, 2002, **500**, 523–544.
8 W. L. Chan and E. J. Chason, *J. Appl. Phys.*, 2007, **101**, 121301.
9 S. Facsko, T. Dekorsy, C. Koerdt, C. Trappe, H. Kurz, A. Vogt and H. L. Hartnagel, *Science*, 1999, **285**, 1551–1553.
10 S. A. Mollick, D. Ghose, P. D. Shipman and R. Mark Bradley, *Appl. Phys. Lett.*, 2014, **104**, 043103.
11 J. Fassbender, T. Strache, M. O. Liedke, D. Markó, S. Wintz, K. Lenz, A. Keller, S. Facsko, I. Mönch and J. McCord, *J. New J. Phys.*, 2009, **11**, 125002.
12 R. Stanley Williams, *Solid State Commun.*, 1982, **41**, 153–156.
13 T. Michely, K. H. Besocke and G. Comsa, *Surf. Sci.*, 1990, **230**, L135–L139.
14 C. Teichert, M. Hohage, T. Michely and G. Comsa, *Phys. Rev. Lett.*, 1994, **72**, 1682–1685.
15 S. Rusponi, C. Boragno and U. Valbusa, *Phys. Rev. Lett.*, 1997, **78**, 2795–2798.
16 U. Valbusa, C. Boragno and F. B. de Mongeot, *J. Phys.: Condens. Matter*, 2002, **14**, 8153–8175.
17 E. Chason, T. M. Mayer, B. K. Kellerman, D. T. Mcilroy and A. J. Howard, *Phys. Rev. Lett.*, 1994, **72**, 3040–3043.
18 S. J. Chey, J. E. VanNostrand and D. G. Cahill, *Phys. Rev. B: Condens. Matter*, 1995, **52**, 16696–16701.
19 L. Li, W. Li, L. Qi, M. Lu, X. Yang and C. Gu, *Phys. Rev. B: Condens. Matter*, 2005, **71**, 155329.
20 J. Kim, D. G. Cahill and R. S. Averback, *Phys. Rev. B: Condens. Matter*, 2003, **67**, 045404.
21 X. Ou, A. Keller, M. Helm, J. Fassbender and S. Facsko, *Phys. Rev. Lett.*, 2013, **111**, 016101.
22 D. Chowdhury, D. Ghose, S. A. Mollick, B. Satpati and S. R. Bhattacharyya, *Phys. Status Solidi B*, 2015, **252**, 811–815.
23 D. Moldovan and L. Golubovic, *Phys. Rev. E: Stat., Nonlinear, Soft Matter Phys.*, 2000, **61**, 6190–6214.
24 G. Apostolopoulos, J. Herfort, L. Daweritz and K. H. Ploog, *Phys. Rev. Lett.*, 2000, **84**, 3358–3361.
25 The 2 dimensional (2D) angle distribution represents the 2 dimensional Cartesian histogram of the local surface angles calculated from the gradients of the surface in the x- and y-direction respectively: $(\alpha_x,\alpha_y) = \left(\arctan\left(\frac{\partial h}{\partial x}\right), \arctan\left(\frac{\partial h}{\partial y}\right)\right)$.
26 V. P. LaBella, H. Yang, D. W. Bullock, P. M. Thibado, P. Kratzer and M. Scheffler, *Phys. Rev. Lett.*, 1999, **83**, 2989–2992.
27 K. Shiraishi, *Appl. Phys. Lett.*, 1992, **60**, 1363.
28 K. A. Bratland, Y. L. Foo, J. A. N. T. Soares, T. Spila, P. Desjardins and J. E. Greene, *Phys. Rev. B: Condens. Matter*, 2003, **67**, 125322.
29 J. Van Nostrand, S. Chey and D. Cahill, *Phys. Rev. B: Condens. Matter*, 1999, **57**, 12536–12543.
30 A. Shklyaev and M. Ichikawa, *Phys. Rev. B: Condens. Matter*, 2001, **65**, 045307.
31 N. Galianaa, P. Martina, C. Munueraa, M. Varelab, F. Soriaa, C. Ocala, A. Ruiza and M. Alonsoa, *Surf. Sci.*, 2006, **600**, 3956–3963.
32 J. N. Aqua, I. Berbezier, L. Favre, T. Frisch and A. Ronda, *Phys. Rep.*, 2013, **522**, 59–189.
33 Optical grating effect of nanogroove structure on group III–V surfaces was characterized on PTB (Physikalisch-Technische Bundesanstalt) beamline. The first-order diffraction was clearly observed.
34 T. Michely, M. Kalff, G. Comsa, M. Strobel and K. H. Heinig, *Phys. Rev. Lett.*, 2001, **86**, 2589–2592.
35 G. Costantini, E. B. de Mongeot, C. Boragno and U. Valbusa, *Phys. Rev. Lett.*, 2001, **86**, 838–841.

36 M. Siegert and M. Plischke, *Phys. Rev. Lett.*, 1994, **73**, 1517–1520.
37 R. M. Bradley and P. D. Shipman, *Phys. Rev. Lett.*, 2010, **105**, 145501.
38 Auger Electron Spectroscopy analysis has been done on ion irradiated GaAs (InAs) surfaces at temperature below and above the recrystallization temperature, respectively. In contrast to the low temperature case, where Ga (In) accumulation is seen, no accumulation of Ga (In) is observed at high temperature irradiation.
39 P. Bellon, *Phys. Rev. Lett.*, 1998, **81**, 4176.

APPLIED PHYSICS LETTERS **107**, 062103 (2015)

Direct determination of the electron effective mass of GaAsN by terahertz cyclotron resonance spectroscopy

F. Eßer,[1,2] O. Drachenko,[1,a)] A. Patanè,[3] M. Ozerov,[4,b)] S. Winnerl,[1] H. Schneider,[1,c)] and M. Helm[1,2]

[1]*Helmholtz-Zentrum Dresden-Rossendorf, Institute of Ion Beam Physics and Materials Research, Bautzner Landstraße 400, 01328 Dresden, Germany*
[2]*Technische Universität Dresden, 01062 Dresden, Germany*
[3]*School of Physics and Astronomy, University of Nottingham, Nottingham NG7 2RD, United Kingdom*
[4]*Helmholtz-Zentrum Dresden-Rossendorf, Dresden High Magnetic Field Laboratory, Bautzner Landstraße 400, 01328 Dresden, Germany*

(Received 4 June 2015; accepted 2 August 2015; published online 12 August 2015)

We use cyclotron resonance THz-spectroscopy in pulsed magnetic fields up to 63 T to measure the electron effective mass in Si-doped GaAsN semiconductor alloys with nitrogen content up to 0.2%. This technique directly probes the transport properties of the N-modified conduction band, particularly the electron effective mass, which has been discussed controversially in the experimental and theoretical literature. We report a slight increase of the electron effective mass and nonparabolicity with N-content for different photon energies in agreement with the two-level band anticrossing model calculations. Furthermore, we show a pronounced electron mobility drop with increasing N-content. © *2015 AIP Publishing LLC*. [http://dx.doi.org/10.1063/1.4928623]

The tunability of the band gap energy of GaAs in the range of 1.4 eV − 0.9 eV upon incorporation of a small concentration of N-atoms ($\leq 5\%$)[1,2] makes the GaAsN alloy an attractive candidate for optoelectronic applications. The differences in size and electronegativity between the N- and As-atoms cause unusual effects including a huge band-gap bowing,[2] a drop in the electron mobility,[3] and a reduced pressure dependence.[4] Therefore, the simple virtual crystal approximation, conventionally used to describe semiconductor alloys, cannot be applied to GaAsN. Shan *et al.*[4] introduced the band anticrossing (BAC) model in 1999, which accurately explains the band-gap reduction and its pressure dependence. This model predicts an increase of the electron effective mass m^* with N content. Shtinkov *et al.*[5] presented an empirical tight-binding (TB) model for the electronic structure and showed a similar behavior for the electron effective mass up to 1.5% of nitrogen as in the BAC. A modified $k \cdot p$ calculation was proposed[6] one year later, which predicted a strong increase of the electron effective mass, followed by a non-monotonic composition dependence due to N-clustering. Pseudopotential,[7–9] first-principles[10–12] and several other calculations were applied, resulting in detailed models for the electronic structure of dilute nitrides, but without information on the electron effective mass. A smooth increase of the electron effective mass was determined by magneto-photoluminescence (PL) on GaAsN/GaAs quantum well (QW) samples with a high N content (0.9% − 4%).[13] Using the same method, a steep increase of m^* was observed by Masia *et al.*[14] and Alberi *et al.*[15] on GaAsN films for low N contents up to 0.2%. Also, while Alberi *et al.*[15] found a decrease of the electron effective mass for N contents above 0.2%, Masia *et al.*[14] observed a non-monotonic compositional dependence at high N consistent with the linear combination of isolated nitrogen states (LCINS) model.[6] The effective mass of GaAsN/GaAs QWs with high nitrogen contents (1.2% and 2%) was determined by optically detected cyclotron resonance.[16] A steep increase of m^* with N content was found with this method, which detects microwave-induced photoluminescence changes versus magnetic field. The measured values lie above the BAC model and in the range of the LCINS predictions. There have also been reports on a decrease of the electron effective mass[17,18] with increasing nitrogen content, measured by electroreflectance and transport techniques.

To resolve this long-standing controversy, we apply cyclotron resonance (CR) absorption spectroscopy, a direct method for effective mass determination, to a series of Si-doped bulk GaAsN alloys with low nitrogen content. Our measurements reveal a slight increase of the CR electron effective mass and nonparabolicity with increasing nitrogen content in good agreement with calculations based on the BAC model.[4] Furthermore, we find a pronounced CR mobility drop of about 65%, which explains the challenging aspect of a direct CR investigation in this highly mismatched alloy.

Epitaxial GaAsN:Si samples were grown on a semi-insulating GaAs substrate at a temperature of 500 °C by molecular beam epitaxy with a thickness of 1 μm on top of a 20 nm GaAs buffer layer grown at 580 °C. The n-doping is nominally $1 \times 10^{17}\,\mathrm{cm}^{-3}$. The nitrogen content was determined to be 0%, 0.1%, and 0.2%, respectively, by x-ray diffraction. For the CR spectroscopy investigation, we used the combination of the free-electron laser (FEL) FELBE and the Dresden High Magnetic Field Laboratory (HLD),[19] both located at the Helmholtz-Zentrum Dresden-Rossendorf. Additional experiments were performed with a quantum cascade laser (QCL) with 17.7 ± 0.5 meV using the setup

[a)]Present address: Laboratoire National des Champs Magnétiques Intenses, CNRS-UJF-UPS-INSA, 143 avenue de Rangueil, 31400 Toulouse, France.
[b)]Present address: Radboud University Nijmegen, FELIX Laboratory, Toernooiveld 7c, 6525 ED Nijmegen, The Netherlands.
[c)]Electronic mail: h.schneider@hzdr.de

described in Ref. 20. The FEL wavelength was determined by a Fourier transform spectrometer. The CR transmission was measured in Faraday geometry with a Ge:Ga detector during a pulse cycle of 150 ms and a field maximum of 63 T.

The experiments were performed at 100 K to avoid carrier freeze-out. That effect would result in so called impurity-shifted cyclotron resonance (ICR)[21,22] which appears at lower resonant magnetic fields B_{res} than the CR of free carriers, as shown for comparison in Fig. 1(a). The impurities are ionized at 100 K such that CR relates to free carriers and we can obtain the CR electron effective mass using

$$m^* = \frac{e}{\omega_{\mathrm{FEL}}} B_{\mathrm{res}}. \tag{1}$$

The CR absorption coefficient α of the GaAsN:Si layer can be expressed classically[23] by the real part of the conductivity

$$\Re(\sigma_{xx}) = \sigma_0 \frac{1 + (\omega\tau)^2 + (\omega_c\tau)^2}{\left[1 - (\omega^2 - \omega_c^2)\tau^2\right]^2 + 4(\omega\tau)^2} = \varepsilon_0 c n_1 \alpha \tag{2}$$

for linearly polarized FEL or QCL radiation, and is defined by the DC conductivity $\sigma_0 = ne^2\tau/m^*$, the carrier density n, the relaxation time τ, and the cyclotron frequency $\omega_c = eB/m^*$. We can then express the transmitted THz radiation T with the Beer-Lambert law

$$\frac{T}{T_0} = (1-R)^2 e^{-\alpha z} = (1-R)^2 \exp\left(-\frac{\Re(\sigma_{xx})}{\varepsilon_0 c n_1} z\right), \tag{3}$$

which allows us to deduce the carrier density n, the scattering time τ, the cyclotron frequency ω_c, and thus the electron effective mass m^*, if we use Eq. (3) as a fitting function to our experimental data. Here, T_0 denotes the intensity of the incident THz radiation, R is the reflectivity that we assume to be constant, n_1 is the refractive index, and ε_0 is the vacuum permittivity.

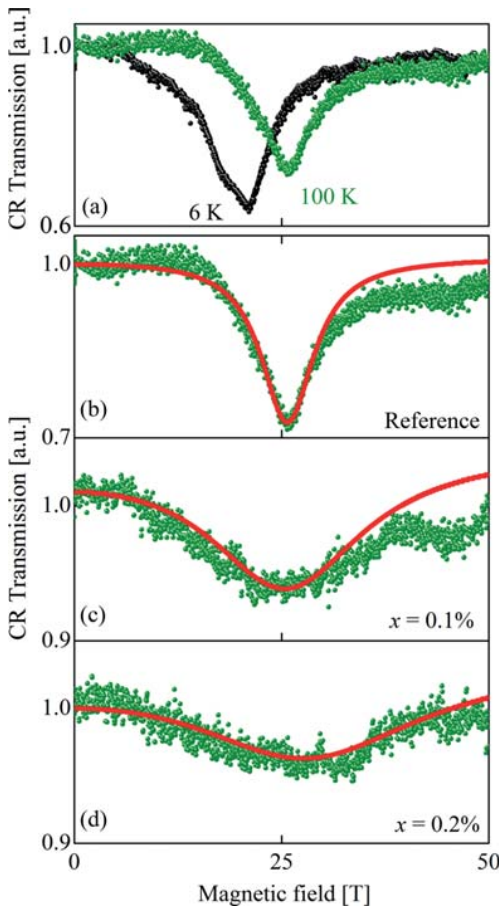

FIG. 1. Transmission spectra with a FEL photon energy of 41.4±0.5 meV: (a) CR (green) and ICR (black) of our reference sample taken at 6 K and 100 K, respectively. (b) – (d) CR transmission of $GaAs_{1-x}N_x$ samples with $x = 0\% - 0.2\%$ at 100 K. Green bullets represent the experimental results and the red line is a classical CR absorption fit to the data using Eq. (3). The minimum at ≈45 T in (c) is an artifact that originates from mechanical noise.

Figures 1(b)–1(d) show CR transmission spectra of GaAsN samples with different N contents taken with the FEL photon energy 41.4±0.5 meV. The comparison of the CR lines indicates that the electron effective mass is not significantly affected by nitrogen content up to $x = 0.2\%$ because of the remarkably small shift of B_{res} between (b) and (d). Due to the energy dependence of m^*, we performed CR spectroscopy experiments with different photon energies below and above the limiting Reststrahlen band of GaAs. The results are summarized in Table I. Figs. 2(a)–2(c) suggest a small increase of m^* with nitrogen content from 0% to 0.2% in the investigated energy range. Furthermore, we calculated the energy dependence of the momentum effective mass[13,24]

$$m^*(k) = \hbar^2 k \left|\frac{dE_-(k)}{dk}\right|^{-1} \tag{4}$$

and use the BAC model[4] for the description of the lowest conduction band

$$E_-(k) = \frac{1}{2}\left(E_N + E_M(k) - \sqrt{(E_N - E_M(k))^2 + 4V_{MN}^2 x}\right) \tag{5}$$

of GaAsN. $E_M(k)$ and $E_N = E_M(0) + 0.23\,\mathrm{eV} = 1.732$ eV are the energies of the GaAs conduction band and of the N level relative to the top of the valence band for 100 K, respectively. $V_{MN} = 2.7$ eV describes the interaction between those two types of states.[25] $E_M(k)$ was calculated in two different ways. We ignored the small nonparabolicity of $E_M(k)$ in the first treatment and described a perfectly parabolic band (solid line). In the second approach, we included the nonparabolicity by a simple two-band $k \cdot p$ approximation[26] (dashed line). The experimental masses of the reference (a) can be perfectly described by the calculated values of the second method. In case of the nitrogen containing samples (b) and (c), we observe an increase of both the CR effective mass and nonparabolicity with increasing N content, which is in good agreement with the energy behavior of the calculated BAC momentum masses. In general, the nonparabolicity is expected to be small at low energies but to increase significantly in proximity of the N-level (>100 meV above $E_M(0)$). Thus, we observe an almost perfectly linear behavior of B_{res} in the inset (d) of Fig. 2 in the energy range up to 40 meV in agreement with calculations based on the BAC model[4] (dashed line).

TABLE I. Results of our CR study for different photon energies (17.7±0.5 meV, 26.7±0.5 meV and 41.4±0.5 meV). The CR electron effective masses m^*, relaxation times τ, and mobilities μ are results of our fit with Eq. (3).

	$h\omega_{QCL} = 17.7\pm0.5$ meV			$h\omega_{FEL} = 26.7\pm0.5$ meV			$h\omega_{FEL} = 41.4\pm0.5$ meV		
N content	0%	0.1%	0.2%	0%	0.1%	0.2%	0%	0.1%	0.2%
m^* (m_0)	0.067 ± 0.002	0.067 ± 0.003	0.069 ± 0.007	0.069 ± 0.001	0.069 ± 0.002	0.072 ± 0.004	0.071 ± 0.001	0.072 ± 0.003	0.08 ± 0.005
τ(fs)	100 ± 20	68 ± 11	43 ± 31	114 ± 10	59 ± 10	45 ± 20	110 ± 15	36 ± 11	36 ± 10
μ (cm^2/V s)	2800 ± 600	1500 ± 300	1100 ± 400	2900 ± 200	1500 ± 200	1100 ± 400	2800 ± 200	900 ± 100	600 ± 200

Another important observation from Fig. 1 is the significant broadening of the CR lines in (c) and (d). This signature is characteristic for the reduction of mobility and relaxation time τ of the nitrogen containing alloys, summarized in Table I. The CR mobilities can be determined by Eqs. (2) and (3) with $\mu = e\tau/m^*$ and are shown in Fig. 3(a) by red triangles. They lie slightly below the Hall mobilities,[27] which are shown with blue diamonds in the same figure. This reflects the weaker sensitivity of the Hall measurement to forward-scattering processes in comparison to CR.[23] TB calculations[28] and Anderson's many-impurity model calculations[29] propose much higher mobility values. Deviations might be explained by not having considered scattering by interstitial nitrogen atoms, ionized impurities (neglected by Ref. 28) or NN-clusters (neglected by Ref. 29). N related scattering can be recognized as the main scattering mechanism.

If we compare our CR effective masses with results in the literature, we find them in good agreement with values obtained from BAC model[4] calculations, as mentioned before, and empirical TB calculations,[5] as can be seen in Fig. 3(b). Magneto-PL,[14,15] on the other hand, yields much larger m^*. Since PL is very sensitive to carrier localization by alloy disorder and clusters, the results in Refs. 14 and 15 can be well described by the LCINS model,[6] which shows that isolated N-impurities and N-clusters form strongly localized energy states in the conduction band. In contrast, CR spectroscopy is only sensitive to delocalized states and thus in agreement with Refs. 4 and 5. Thus, the origin of this difference is that CR probes delocalized states and measures the average mass at the Fermi energy, whereas magneto-PL is dominated by emission from localized states in regions with higher N. Hence, contradicting results in the literature on the electron effective mass determination arise from the use of techniques that are indirect and also very sensitive to disorder and carrier localization phenomena.

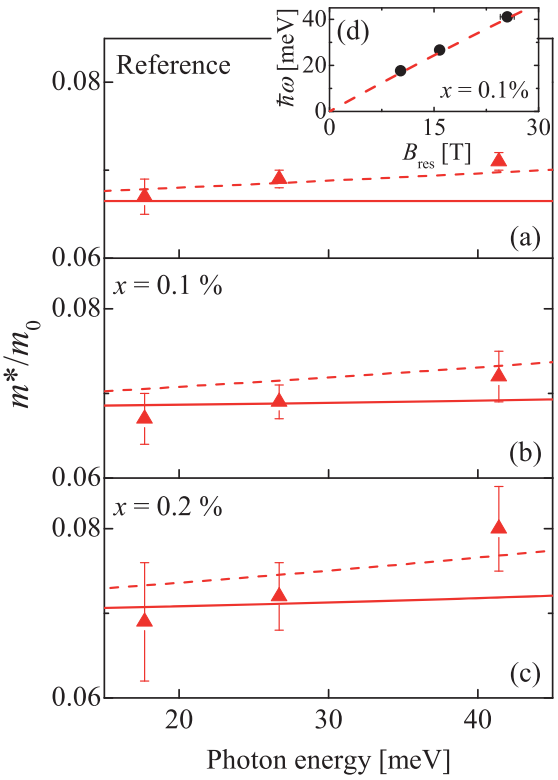

FIG. 2. Energy dependence of the electron effective mass. Triangles originate from CR spectroscopy investigations with different photon energies. Momentum masses (see Eq. (4)) were calculated using the BAC[4] model and are shown for the parabolic approximation of the GaAs CB (solid lines) and under consideration of the CB nonparabolicity (dashed lines) for $GaAs_{1-x}N_x$ with (a) $x = 0\%$, (b) $x = 0.1\%$, and (c) $x = 0.2\%$. The inset (d) depicts B_{res} in dependence of the photon energy for $x = 0.1\%$. Circles represent experimental values and the dashed line stands for a BAC fit.

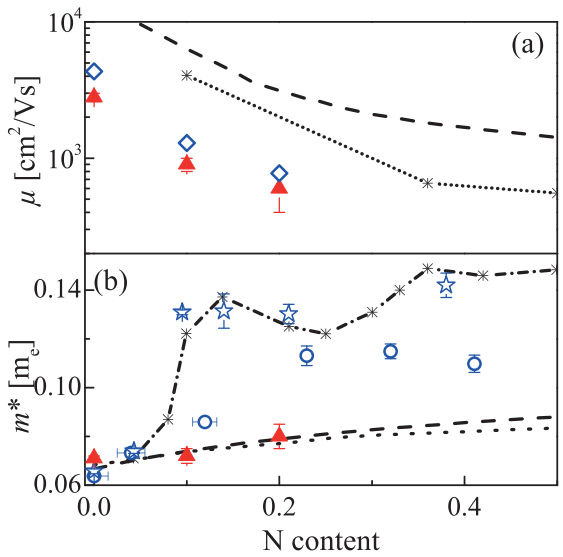

FIG. 3. (a) Mobility μ vs. N content. CR and Hall[27] mobilities are shown for 100 K with red triangles and blue diamonds, respectively. The dashed[29] and dotted[28] lines represent calculations for n-doped (10^{17} cm^{-3}) GaAsN at room temperature. (b) Effective mass m^* vs. N content. CR effective masses (triangles) are compared with calculations based on the BAC model[4] (dashed line), the empirical TB[5] (dotted line), and the LCINS model[6] calculations (dashed-dotted line). Magneto-PL results on m^* are shown with circles[15] and stars,[14] respectively. The underlying CR experiments were taken at 41.4±0.5 meV and 100 K.

In summary, we performed CR spectroscopy investigations on Si-doped GaAsN alloys with different nitrogen contents using high pulsed magnetic fields in combination with FEL/QCL THz radiation. We found a moderate increase of the CR electron effective mass and nonparabolicity in good agreement with calculations based on the two-level BAC model.[4] Furthermore, we observed a pronounced CR mobility drop in the nitrogen containing samples. Although N related scattering is the main scattering mechanism, other scattering processes cannot be ignored. The discrepancy between CR and magneto-PL results concerning the electron effective mass can be explained by the different sensitivity of the two methods to carrier localization by N-induced localized states.

We gratefully acknowledge M. Hopkinson and coworkers for growing our samples as well as helpful discussions with G. Pettinari and A. Polimeni. Furthermore, we thank P. Michel, W. Seidel, and the FELBE team and S. Zvyagin, O. Ponomaryov, and the team of HLD, member of the European Magnetic Field Laboratory (EMFL) for their dedicated support. This work was partly supported by the German Research Council (DFG) under Grant No. DR832/3-1.

[1]M. Weyers, M. Sato, and H. Ando, Jpn. J. Appl. Phys., Part 2 **31**, L853 (1992).
[2]W. G. Bi and C. W. Tu, Appl. Phys. Lett. **70**, 1608 (1997).
[3]R. Mouillet, L.-A. de Vaulchier, E. Deleporte, Y. Guldner, L. Travers, and J.-C. Harmand, Solid State Commun. **126**, 333 (2003).
[4]W. Shan, W. Walukiewicz, J. W. Ager, E. E. Haller, J. F. Geisz, D. J. Friedman, J. M. Olson, and S. R. Kurtz, Phys. Rev. Lett. **82**, 1221 (1999).
[5]N. Shtinkov, P. Desjardins, and R. A. Masut, Phys. Rev. B **67**, 081202 (2003).
[6]A. Lindsay and E. P. O'Reilly, Phys. Rev. Lett. **93**, 196402 (2004).
[7]L. Bellaiche, S.-H. Wei, and A. Zunger, Phys. Rev. B **56**, 10233 (1997).
[8]T. Mattila, S.-H. Wei, and A. Zunger, Phys. Rev. B **60**, R11245 (1999).
[9]P. R. C. Kent and A. Zunger, Phys. Rev. Lett. **86**, 2613 (2001).
[10]E. D. Jones, N. A. Modine, A. A. Allerman, S. R. Kurtz, A. F. Wright, S. T. Tozer, and X. Wei, Phys. Rev. B **60**, 4430 (1999).
[11]L.-W. Wang, Appl. Phys. Lett. **78**, 1565 (2001).
[12]H. Benaissa, A. Zaoui, and M. Ferhat, J. Appl. Phys. **102**, 113712 (2007).
[13]C. Skierbiszewski, I. Gorczyca, S. Lepkowski, J. Lusakowski, J. Borysiuk, and J. Toivonen, Semicond. Sci. Technol. **19**, 1189 (2004).
[14]F. Masia, G. Pettinari, A. Polimeni, M. Felici, A. Miriametro, M. Capizzi, A. Lindsay, S. B. Healy, E. P. O'Reilly, A. Cristofoli, G. Bais, M. Piccin, S. Rubini, F. Martelli, A. Franciosi, P. J. Klar, K. Volz, and W. Stolz, Phys. Rev. B **73**, 073201 (2006).
[15]K. Alberi, S. A. Crooker, B. Fluegel, D. A. Beaton, A. J. Ptak, and A. Mascarenhas, Phys. Rev. Lett. **110**, 156405 (2013).
[16]P. N. Hai, W. M. Chen, I. A. Buyanova, H. P. Xin, and C. W. Tu, Appl. Phys. Lett. **77**, 1843 (2000).
[17]R. Kudrawiec, M. Motyka, M. Gladysiewicz, J. Misiewicz, J. Gupta, and G. Aers, Solid State Commun. **138**, 365 (2006).
[18]D. L. Young, J. F. Geisz, and T. J. Coutts, Appl. Phys. Lett. **82**, 1236 (2003).
[19]S. A. Zvyagin, M. Ozerov, E. Cizmàr, D. Kamenskyi, S. Zherlitsyn, T. Herrmannsdörfer, J. Wosnitza, R. Wünsch, and W. Seidel, Rev. Sci. Instrum. **80**, 073102 (2009).
[20]O. Drachenko, S. Winnerl, H. Schneider, M. Helm, J. Wosnitza, and J. Leotin, Rev. Sci. Instrum. **82**, 033108 (2011).
[21]J. R. Apel, T. O. Poehler, C. R. Westgate, and R. I. Joseph, Phys. Rev. B **4**, 436 (1971).
[22]B. D. McCombe, R. Kaplan, R. J. Wagner, E. Gornik, and W. Müller, Phys. Rev. B **13**, 2536 (1976).
[23]O. Drachenko and M. Helm, in *Semiconductor Research*, Springer Series in Materials Science, edited by A. Patanè and N. Balkan (Springer, Berlin, Heidelberg, 2012), Vol. 150, p. 283.
[24]W. Zawadzki, Adv. Phys. **23**, 435 (1974).
[25]W. Walukiewicz, W. Shan, J. W. Ager, D. R. Chamberlin, E. E. Haller, J. F. Geisz, D. J. Friedman, J. M. Olson, and S. R. Kurtz, ECS Proc. **99-11**, 190 (1999).
[26]J. S. Blakemore, J. Appl. Phys. **53**, R123 (1982).
[27]A. Patanè, G. Allison, L. Eaves, N. V. Kozlova, Q. D. Zhuang, A. Krier, M. Hopkinson, and G. Hill, Appl. Phys. Lett. **93**, 252106 (2008).
[28]S. Fahy, A. Lindsay, H. Ouerdane, and E. P. O'Reilly, Phys. Rev. B **74**, 035203 (2006).
[29]M. P. Vaughan and B. K. Ridley, Phys. Rev. B **75**, 195205 (2007).

APPLIED PHYSICS LETTERS **107**, 242405 (2015)

From a non-magnet to a ferromagnet: Mn^+ implantation into different TiO_2 structures

O. Yıldırım,[1,2,a)] S. Cornelius,[1,3] M. Butterling,[4] W. Anwand,[4] A. Wagner,[4] A. Smekhova,[5,6] J. Fiedler,[1] R. Böttger,[1] C. Bähtz,[1,7] and K. Potzger[1]

[1]*Helmholtz-Zentrum Dresden - Rossendorf, Institute of Ion Beam Physics and Materials Research, Bautzner Landstr. 400, 01328 Dresden, Germany*
[2]*Technische Universität Dresden, D-01062 Dresden, Germany*
[3]*Department of Chemical Engineering, Materials for Energy Conversion and Storage, Delft University of Technology, Julianalaan 136, NL-2628BL Delft, The Netherlands*
[4]*Helmholtz-Zentrum Dresden - Rossendorf, Institute of Radiation Physics, Bautzner Landstr. 400, 01328 Dresden, Germany*
[5]*Faculty of Physics, Lomonosov Moscow State University (MSU), 119991 Moscow, Russia*
[6]*Faculty of Physics and CENIDE, University of Duisburg-Essen, Lotharstr. 1, 47048 Duisburg, Germany*
[7]*Rossendorf Beamline, European Synchrotron Radiation Facility, F-38043 Grenoble, France*

(Received 4 November 2015; accepted 3 December 2015; published online 15 December 2015)

We report effect of the initial structural order on the resulting magnetic properties of manganese implanted TiO_2 films. Different microstructures of as-grown TiO_2 films, namely, amorphous, polycrystalline anatase, and epitaxial anatase, have been implant-doped with Mn^+ up to a concentration of 5 at. %. We found that different initial structures lead to different defect and charge carrier concentrations and, as a result, strongly influence the magnetic properties upon implantation. Depending on the initial microstructure, paramagnetism, secondary phases related magnetic properties as well as ferromagnetism could be observed in the films.
[http://dx.doi.org/10.1063/1.4938069]

Until the discovery of room temperature ferromagnetism (FM) in TiO_2:Co (anatase),[1] studies on dilute magnetic semiconductors (DMS) were mostly focused on II–VI and III–V compounds. The aforementioned report broadened the research area of DMS to oxides and it has stimulated numerous follow-up studies. The simple experimental concept of doping TiO_2 with a few atomic percent of 3d metal cations is expected to yield substitutional dopant sites, which are separated by large distances, yet ferromagnetically ordered.[2] Such a ferromagnetic order, covering long-range distances, is inexplicable in terms of common super-exchange and double exchange, which consider only the first or second nearest-neighbour cation interactions.[3] Therefore, the discovery of dilute magnetic oxides (DMOs) also fueled a debate on the origin and the mechanism of the observed FM in such systems. The origin of the observed FM in DMOs can vary from magnetic contaminations,[4] secondary phases[5] to open-volume defects,[6–8] which are considered as extrinsic or unwanted sources of FM. On the other hand, if FM occurs due to coupling of dopant atoms residing on substitutional sites within the host lattice, it is considered to be an intrinsic effect. Consequently, identifying electronic and defect properties of the material along with the chemical environment of the dopant is of primary importance in order to understand the interplay between extrinsic and intrinsic origins of the magnetic properties. In this study, TiO_2 films with different defect properties have been prepared by adjusting their initial microstructure. Subsequently, Mn^+ implantation was performed in order to dope the TiO_2 films, and the effect of the microstructure on the resulting magnetic properties has been investigated along with electric transport and defect properties.

TiO_2 films of 300 nm thickness were grown on $SrTiO_3$ (100) single crystals by means of DC magnetron sputtering. A high purity oxygen deficient ceramic TiO_{2-x} target was sputtered at 120 W in Ar/O_2 atmosphere at a pressure of 0.7 Pa containing ~0.4 vol. % of O_2. These conditions were found to yield near-stoichiometric films confirmed by the absence of optical absorption below the bandgap of 3.2(±0.1) eV, as determined by spectral photometry (not shown). Amorphous TiO_2 films were obtained by deposition on unheated substrates. Polycrystalline anatase TiO_2 structure was achieved by post-growth annealing of initially amorphous layers at 450 °C for 1 h in vacuum ($<2 \times 10^{-5}$ Pa). Epitaxial anatase TiO_2, on the other hand, was obtained by direct deposition on substrates heated to 500 °C. For a homogeneous depth distribution of the Mn ions, as compared to the Gaussian-like depth distribution for implantations at a single energy, five different energy and ion fluence combinations, as determined by SRIM simulations,[9] have been applied[10] (see Ref. 11 for a similar ion implantation depth profile calculation). The maximum implantation depth was calculated to be around 150 nm. By keeping the maximum implantation depth around 150 nm, the interfacial mixing between the film and substrate, as well as doping of the substrate, is avoided. Moreover, having the implantation profile somewhat thinner than the actual film thickness also helps to avoid the formation of interfacial clusters.[12] The crystalline structure of both as-grown and implanted TiO_2 films was controlled by means of X-ray diffraction (XRD) measurements using Ni-filtered Cu-Kα radiation of a PANalytical Empyrean diffractometer. The local atomic

[a)]Author to whom correspondence should be addressed. Electronic mail: o.yildirim@hzdr.de

coordination of the implanted Mn dopant was investigated by X-ray absorption near-edge spectroscopy (XANES) at Mn K-edge. XANES measurements were performed in fluorescence mode using energy-resolved detector at the ROBL-MRH setup of the BM-20 beamline at the ESRF in Grenoble, France. All structural characterizations were performed at room temperature. The magnetic properties of the implanted films were investigated by a superconducting quantum interference device (SQUID, Quantum Design MPMS XL 7). Magnetometry was performed as function of temperature and magnetic field. For all samples, zero field cooled (ZFC) and field cooled (FC) thermomagnetic measurements have been carried out in an applied external magnetic field of 15 mT. The electrical transport properties of the films were characterized using a LakeShore HMS 9709 Hall measurement system in the temperature range of 20 K and 300 K and an applied external field range of 1 T with probe current of 1 mA. Ohmic contacts were employed by sputtering gold onto sample corners and attaching silver wires with silver glue on top of gold layers. The Hall effect measurements were carried out in van der Pauw geometry. Positron annihilation spectroscopy (PAS) was performed at the Slow Positron System of Rossendorf (SPONSOR).[13] The positron beam emitted from a ^{22}Na radioactive source was accelerated up to 30 keV for depth resolved Doppler broadening spectroscopy. The S parameter, characteristic of open volume defect concentration within the film,[14] is extracted from the Doppler broadening of the 511 keV photon peak originating from positron-electron annihilation in the sample.

XRD pattern analysis shows that all of the observed diffraction maxima of the polycrystalline and epitaxial films can be identified with the anatase phase of TiO_2 (not shown). Moreover, out-of-plane c-axis texture, i.e., $TiO_2(001)\|STO(100)$, for as-grown epitaxial film is confirmed by rocking curve measurements at the anatase (004) reflection (not shown). Upon Mn^+ implantation, rutile formation is observed both in initially polycrystalline anatase and epitaxial anatase films. Similar XRD patterns along with a detailed analysis on the structural deformation by considering the formation of rutile phases upon ion implantation is given elsewhere.[11] However, given the weak contribution of rutile related peaks to the total XRD pattern, the initial anatase structure has been mostly preserved after implantation. Apart from the rutile phases, no other known Mn related secondary phases could be detected by XRD.

The Mn^+-implanted polycrystalline and epitaxial TiO_2 films show n-type degenerate semiconducting behavior, i.e., the electron density is temperature independent with free electron concentrations of $1.54 \times 10^{19}\,cm^{-3}$ and $6.21 \times 10^{18}\,cm^{-3}$, for the Mn^+-implanted polycrystalline and epitaxial films, respectively. The room temperature electron mobilities are $\sim 2\,cm^2/V^{-1}s^{-1}$ for polycrystalline and $\sim 15\,cm^2/V^{-1}s^{-1}$ for epitaxial TiO_2:Mn film, which are comparable to the reported values for Nb doped epitaxial anatase TiO_2 films.[15] In the case of amorphous films, the contact resistance was above the measurement limit (>20 GΩ cm). Additionally, no anomalous Hall effect (AHE) has been observed for any of the three Mn^+-implanted samples within the investigated temperature range.

Figure 1 depicts the S parameter dependence on the positron energy as obtained from the PAS measurements on as-grown (a) and Mn^+-implanted (b) TiO_2 films. The data shown provide some depth information, because the positron energy defines the implantation depth of positrons into the sample, which is then followed by diffusion until annihilation takes place. Since the film surface acts as a positron sink, the S parameter is high at lowest positron energies (region I). Positrons implanted at higher energies remain in the bulk of the film, resulting in a plateau of the S parameter that provides information about defect concentration within the film (region II). Moreover, owing to the positive charge of the positron, PAS measurements are only sensitive to negatively charged or neutral vacancy defects. The PAS measurements on as-grown TiO_2 films reveal that the concentration of these defects is highest in as-grown amorphous TiO_2 and decreases in polycrystalline and further in epitaxial TiO_2 (Fig. 1(a)). After the Mn^+ implantation this trend is preserved (Fig. 1(b)). The more pronounced plateau of the S parameter depth profile observed in Mn^+-implanted polycrystalline and epitaxial films as compared to their as-grown states may be attributed to an increased sub-surface defect concentration, leading to suppressed positron diffusion towards the surface.

Figure 2(a) shows the Mn K-edge XANES spectra of the Mn^+-implanted TiO_2 films. Post-edge region of each spectrum was normalized to unity. The positions of the Mn K-edges for all three TiO_2:Mn structures coincide with those of MnO[16] and $MnTiO_3$,[17] confirming that most of the

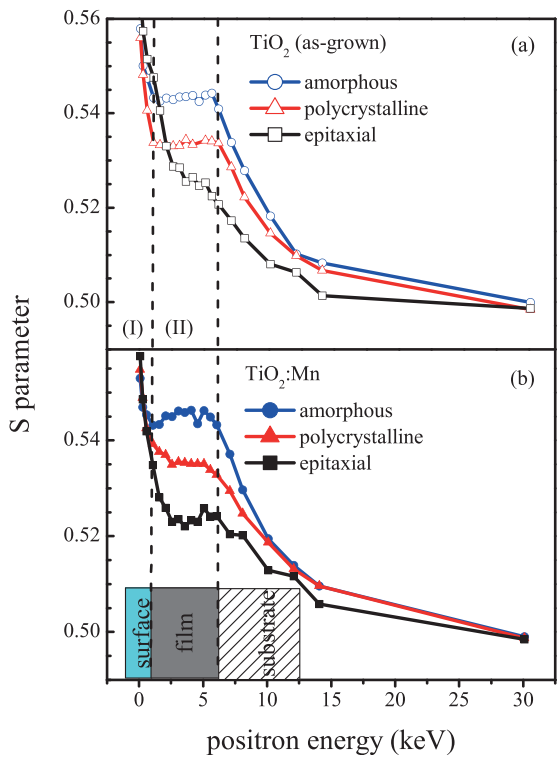

FIG. 1. S parameter depth profiles of as-grown (a) and Mn^+-implanted (b) TiO_2 structures. Dashed lines are present to guide the eyes and the energy range between them roughly corresponds to film body. A schematic sketch of the positron energy-depth profile through a thin film sample is given at the bottom of the figure.

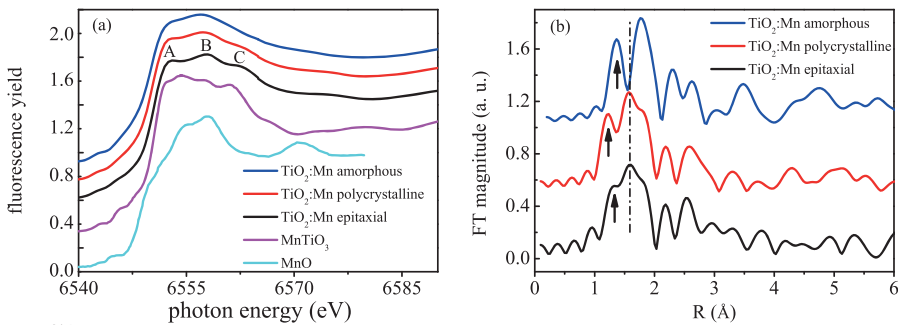

FIG. 2. (a) Mn K-edge XANES spectra of Mn^+-implanted TiO_2 structures along with reference spectra of MnO[16] and $MnTiO_3$[17] (reference spectra shifted vertically for clarity by considering the energy calibration of experimental setup). Data were obtained in grazing incidence geometry at 1° to enhance the Mn fluorescence signal. A, B, and C are given in order to guide the eyes and represent three distinct features, which show differences for each microstructure type. (b) Fourier transform of k^3-weighted extended XANES spectra of the experimental data. (The FT are not corrected with a phase shift.) The dotted-dashed line as well as arrows is present to guide the eyes.

implanted Mn atoms are in (II) oxidation state. In spite of an octahedral oxide coordination of Mn in both MnO and $MnTiO_3$, the difference in the local Mn-O coordination depends on the distortion of the octahedron, which can also be probed and distinguished by XANES measurements.[18,19] The XANES spectra of the three TiO_2:Mn films are dominated by three common features A, B, and C (Fig. 2(a)). These features are most pronounced in the case of the epitaxial film and resemble the $MnTiO_3$ spectrum. With increasing structural disorder from epitaxial to polycrystalline TiO_2, the features A–C tend to broaden. In particular, feature C, which appears as a weak shoulder in the polycrystalline film, vanishes in the case of the amorphous TiO_2:Mn, i.e., its presence reflects higher microstructural order. The Fourier transforms (FT) of the $k^3\chi(k)$ weighted Mn K-edge spectra of the Mn^+-implanted TiO_2 films are depicted in Fig. 2(b). The most intense FT peak of the epitaxial film was found at the same position for Ti in anatase structure.[20] Correspondingly, peak at around 1.60 Å (marked with a dashed-dotted line) is related to the Mn-O distance in the octahedron. For the amorphous film, this peak is shifted, which suggests a different Mn-O distance as compared to the epitaxial and the polycrystalline films. On the other hand, this peak contains a weak shoulder (shown by arrows) at around 1.3 Å for the epitaxial film. This shoulder becomes more pronounced for the polycrystalline film and eventually for the amorphous film it becomes almost an independent peak separated from the main peak. This situation seems to reflect different distortions of the octahedron.[21] Backscattering amplitudes and sizes of Mn and Ti atoms are slightly different, so if both of these atoms occupy the equivalent positions in the same matrix, the corresponding EXAFS signal will be disturbed and the most intense line of the FT could broaden. As a consequence, for the amorphous film, Mn atoms show different coordination geometry as compared to the epitaxial film. The similarities between the spectra obtained from the epitaxial film and Mn environment in $MnTiO_3$ and Ti environment in the anatase TiO_2 imply that most of the implanted Mn atoms within the epitaxial film reside in Ti lattice sites. For the polycrystalline film, due to a pronounced shoulder at 1.3 Å as compared to the epitaxial film, the Mn atoms appear to have two types of oxide coordination geometries, i.e., only a partial incorporation of Mn by substitution of Ti must be assumed.

The temperature dependent magnetometry results for the Mn^+-implanted TiO_2 structures are shown in Figure 3. It is worth to note that prior to implantation, all of the as-grown TiO_2 films showed only diamagnetic response. The Mn^+-implanted amorphous film exhibits a splitting between ZFC and FC curves and an antiferromagnetic-like transition at around 110 K (Fig. 3). This value is in agreement with the Néel temperature of MnO,[22,23] supporting the secondary phase-like coordination geometry of Mn in amorphous TiO_2 found from XANES measurements. Mn^+-implanted polycrystalline film shows a ferromagnetic behavior with a T_C of around 230 K. At low temperatures ($T \leq 25$ K), the magnetization of the polycrystalline film shows a tendency to decrease (Fig. 3), suggesting the existence of antiferromagnetic interactions. The saturation magnetization of polycrystalline TiO_2:Mn was found to be around $0.85\mu_B$/Mn at 20 K

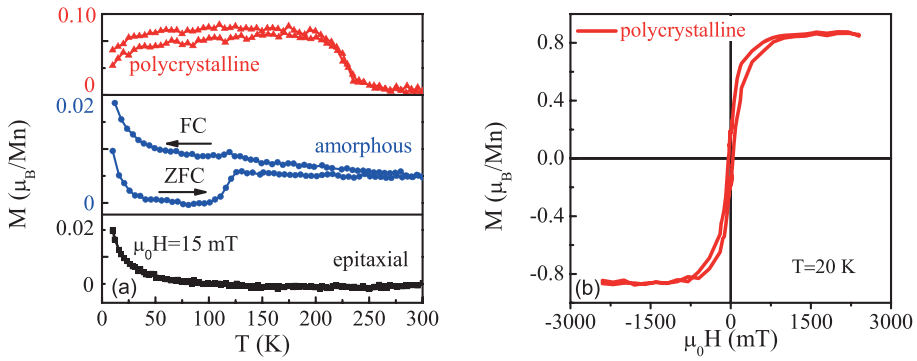

FIG. 3. (a) In-plane thermal scans of the magnetization of Mn^+-implanted TiO_2 films with different as-grown microstructures. (b) In-plane magnetic field dependent magnetization curve of Mn^+-implanted polycrystalline film at 20 K. For all of the measurements, diamagnetic contribution of the substrate was subtracted. Magnetic moment per Mn atom values were calculated by taking into account of total number of the implanted Mn atoms, independent of lattice-host incorporation.

(Fig. 3). These two contributions to magnetic properties of the polycrystalline film support the presence of two different local environments of Mn, as indicated by XANES. By comparison to the amorphous film, the antiferromagnetic-like negative contribution is attributed to a Mn related secondary phase, whereas the FM is due to the presence of Mn_{Ti} substitutional sites. On the other hand, although most of the Mn atoms in the epitaxial film substitutes for Ti, this sample shows no signs of FM but, a well defined weak paramagnetic behavior. Recently, it was reported that the FM in transition metal doped anatase TiO_2 appears above a certain carrier concentration ($\sim 1.8 \times 10^{19}\,cm^{-3}$).[24] This is comparable to the value measured in polycrystalline TiO_2:Mn, whereas the carrier concentration in the epitaxial sample is below. This may explain the absence of ferromagnetic interactions in the epitaxial TiO_2:Mn sample investigated in the present work. On the other hand, absence of AHE in polycrystalline anatase TiO_2:Mn is attributed to low carrier concentration.[25] Furthermore, compared to a previous study on 5 at. % Mn^+-implanted rutile TiO_2 single crystals,[26] the ferromagnetic behavior found for the polycrystalline film shows differences in saturation and thermal magnetization behavior. The extrapolated Curie temperature in Ref. 26 was found to be around room temperature, and the highest saturation magnetization is reported to be around $0.4\mu_B$. These differences must be attributed to the use of rutile TiO_2 in contrast to anatase TiO_2 in the present study. Our results also differ significantly from pure defect-induced FM in two main points. First, it is observed that the polycrystalline TiO_2:Mn is ferromagnetic with a Curie temperature at around 230 K, while almost all of the studies on the defect-induced FM report that ferromagnetic order exist above room temperature.[27] In addition, we find that the observed FM is correlated to the dopant type. In a recent study, we have investigated 5 at. % Co^+ implantation into the same type of polycrystalline anatase TiO_2 films under equivalent conditions.[11] In contrast to Mn^+ implantation, Co^+ implantation leads to paramagnetism independent of the crystalline structure of the as-grown films.

In summary, we have prepared TiO_2:Mn (5 at. %) with amorphous, polycrystalline anatase and epitaxial anatase structure. The initial microstructure, characterized by open-volume defect concentration and crystallographic order, strongly affects the magnetic properties upon Mn^+ implantation. The FM, observed in the Mn^+-implanted polycrystalline film, is attributed to the presence of a high carrier concentration together with a sufficient amount of defects, which facilitate ferromagnetic coupling. On the other hand, paramagnetic behavior has been observed in the case of the epitaxial TiO_2:Mn film, which showed the lowest defect concentration and lower carrier density as compared to the polycrystalline film. The magnetic properties of the amorphous film are attributed to the secondary phase formation. The observed dopant type, carrier, and defect concentration dependent ferromagnetic behavior points towards an intrinsic mechanism for ferromagnetic order in Mn^+-implanted polycrystalline anatase TiO_2 film, and it is generally consistent with a bound magnetic polaron description.[28,29] Consequently, our results suggest that polycrystalline anatase TiO_2 is an excellent candidate structure for DMO applications.

The authors would like to thank Mr. F. Ludewig for conducting ion implantations, Dr. C. Fowley for fruitful discussions, and Mrs. A. Scholz for performing XRD measurements. The work was supported by the Initiative and Networking Fund of the German Helmholtz Association, Helmholtz-Russia Joint Research Group HRJRG 314, and the Russian Foundation for Basic Research, RFBR No. 12-02-91321-*SIG_a*.

[1]Y. Matsumoto, M. Murakami, T. Shono, T. Hasegawa, T. Fukumura, M. Kawasaki, P. Ahmet, T. Chikow, S. Koshibara, and H. Koinuma, Science **291**, 854 (2001).
[2]W. Prellier, A. Fouchet, and B. Mercey, J. Phys. Condens. Matter **15**, R1583 (2003).
[3]J. B. Goodenough, *Magnetism and the Chemical Bond* (Interscience, New York, 1963).
[4]D. W. Abraham, M. M. Frank, and S. Guha, Appl. Phys. Lett. **87**, 252502 (2005).
[5]N. Akdogan, A. Nefedov, R. I. Khaibullin, A. Westphalen, L. R. Tagirov, B. Aktas, and H. Zabel, J. Magn. Magn. Mater. **300**, e4 (2006).
[6]T. Tietze, P. Audehm, Y. C. Chen, G. Shutz, B. B. Straumal, S. G. Protasova, A. A. Mazilkin, P. B. Straumal, T. Proksch, H. Luetkens, Z. Salman, A. Suter, B. Baretzky, K. Fink, W. Wenzel, D. Danilov, and E. Goering, Sci. Rep. **5**, 8871 (2015).
[7]J. M. D. Coey, P. Stamenov, R. D. Gunning, M. Venkatesan, and K. Paul, New J. Phys. **12**, 053025 (2010).
[8]Y. B. Nian, J. Strozier, N. J. Wu, X. Chen, and A. Ignatiev, Phys. Rev. Lett. **98**, 146403 (2007).
[9]J. F. Ziegler, M. D. Ziegler, and J. P. Biersack, Nucl. Inst. Methods Phys. Res. B **268**, 1818 (2010).
[10]The ion energies of 190 keV, 100 keV, 70 keV, 50 keV, and 30 keV applied sequentially, while the ion fluences of 42×10^{15} at./cm^3, 11.5×10^{15} at./cm^3, 3.75×10^{15} at./cm^3, 4.75×10^{15} at./cm^3, and 3.75×10^{15} at./cm^3 have been employed from the highest energy to the lowest, respectively.
[11]O. Yildirim, S. Cornelius, A. Smekhova, G. Zukov, E. A. Ganshina, A. Granovsky, R. Huebner, C. Baehtz, and K. Potzger, J. Appl. Phys. **117**, 183901 (2015).
[12]N. Akdogan, A. Nefedov, K. Westerholt, H. Zabel, H.-W. Becker, C. Somsen, R. I. Khaibullin, and L. R. Tagirov, J. Phys. D: Appl. Phys. **41**, 165001 (2008).
[13]W. Anwand, G. Brauer, M. Butterling, H. R. Kissener, and A. Wagner, Defect Diffus. Forum **331**, 25 (2012).
[14]M. P. Petkov, M. H. Weber, K. Lynn, K. P. Rodbell, and S. A. Cohen, Appl. Phys. Lett. **74**, 2146 (1999).
[15]Y. Furubayashi, T. Hitosugi, Y. Yamamoto, K. Inaba, G. Kinoda, Y. Hirose, T. Shimada, and T. Hasegawa, Appl. Phys. Lett. **86**, 252101 (2005).
[16]K.-W. Nam, M. G. Kim, and K.-B. Kim, J. Phys. Chem. C **111**, 749 (2007).
[17]M. Valant, T. Kolodiazhnyi, I. Arcon, F. Aguesse, A.-K. Axelsson, and N. M. Alford, Adv. Funct. Mater. **22**, 2114 (2012).
[18]L. Zhang, J. Li, Y. Du, J. Wang, X. Wei, J. Zhou, J. Cheng, W. Chu, Z. Jiang, Y. Huang, C. Yan, S. Zahng, and Z. Wu, New J. Phys. **14**, 013033 (2012).
[19]S. W. Chen, P. A. Lin, H. T. Jeng, S. W. Fu, J. M. Lee, J. F. Lee, C. W. Pao, H. Ishii, K. D. Tsuei, N. Hiraoka, D. P. Chen, S. X. Dou, X. L. Wang, K. T. Lu, and J. M. Chen, Appl. Phys. Lett. **104**, 082104 (2014).
[20]G. Vlaic, J. C. J. Bart, W. Cavigiolo, S. Mobilio, and G. Navarra, Z. Naturforsch. **86a**, 1192 (1981), available at http://zfn.mpdl.mpg.de/data/Reihe_A/36/ZNA-1981-36a-1192.pdf.
[21]T. Nedoseykina, M. G. Kim, S.-A. Park, H.-S. Kim, S.-B. Kim, J. Cho, and Y. Lee, Electrochem. Acta **55**, 8876 (2010).
[22]D. P. Shoemke, M. Grossman, and R. Seshadri, J. Phys.: Condens. Matter **20**, 195219 (2008).
[23]Z. Ge, W. L. Lim, S. Shen, Y. Y. Zhou, X. Liu, J. K. Furdyna, and M. Dobrowolska, Phys. Rev. B **75**, 014407 (2007).
[24]T. S. Krasienapibal, S. Inoue, T. Fukumura, and T. Hasegawa, Appl. Phys. Lett. **106**, 202402 (2015).
[25]J. S. Higgins, S. R. Shinde, S. B. Ogale, T. Venkatesan, and R. L. Greene, Phys. Rev. B **69**, 073201 (2004).
[26]D. Menzel, I. Jursic, J. Schoenes, F. Iacomi, and D. Cacaina, Phys. Status Solidi C **3**, 4119 (2006).
[27]P. Esquinazi, W. Hergert, D. Spemann, A. Setzer, and A. Ernst, IEEE Trans. Magn. **49**(8), 4668 (2013).
[28]A. Kaminski and S. DasSarma, Phys. Rev. Lett. **88**, 247202 (2002).
[29]H. Chou, C. P. Lin, J. C. A. Huang, and H. S. Hsu, Phys. Rev. B **77**, 245210 (2008).

SCIENTIFIC REPORTS

OPEN

SUBJECT AREAS:
SEMICONDUCTORS
MAGNETIC PROPERTIES AND MATERIALS

Received
7 November 2014

Accepted
13 February 2015

Published
11 March 2015

Correspondence and requests for materials should be addressed to Y.L. (y.liu@hzdr.de) or S.Z. (s.zhou@hzdr.de)

Carbon *p* Electron Ferromagnetism in Silicon Carbide

Yutian Wang[1,5], Yu Liu[1,2], Gang Wang[2], Wolfgang Anwand[3], Catherine A. Jenkins[4], Elke Arenholz[4], Frans Munnik[1], Ovidiu D. Gordan[6], Georgeta Salvan[6], Dietrich R. T. Zahn[6], Xiaolong Chen[2], Sibylle Gemming[1,6], Manfred Helm[1,5] & Shengqiang Zhou[1]

[1]Helmholtz-Zentrum Dresden-Rossendorf, Institute of Ion Beam Physics and Materials Research, Bautzner Landstr. 400, 01328 Dresden, Germany, [2]Research & Development Center for Functional Crystals, Beijing National Laboratory for Condensed Matter Physics, Institute of Physics, Chinese Academy of Sciences, Beijing 100190, China, [3]Institute of Radiation Physics, Helmholtz-Zentrum Dresden-Rossendorf, Bautzner Landstr. 400, 01328 Dresden, Germany, [4]Advanced Light Source, Lawrence Berkeley National Laboratory, Berkeley, California 94720, USA, [5]Technische Universität Dresden, 01062 Dresden, Germany, [6]Institute of Physics, Technische Universität Chemnitz, 09107 Chemnitz, Germany.

Ferromagnetism can occur in wide-band gap semiconductors as well as in carbon-based materials when specific defects are introduced. It is thus desirable to establish a direct relation between the defects and the resulting ferromagnetism. Here, we contribute to revealing the origin of defect-induced ferromagnetism using SiC as a prototypical example. We show that the long-range ferromagnetic coupling can be attributed to the *p* electrons of the nearest-neighbor carbon atoms around the $V_{Si}V_C$ divacancies. Thus, the ferromagnetism is traced down to its microscopic electronic origin.

Unexpected ferromagnetism has been observed or theoretically predicted for numerous defective carbon based materials and wide-band gap semiconductors such as highly oriented pyrolytic graphite (HOPG), graphene, oxides and SiC[1–12], which provides an alternative for organic and semiconductor spintronics. As the origin of the ferromagnetism is different from that in conventional *d*-electron ferromagnets, any experimental evidence to reveal its origin will be crucial. Červenka *et al.*[13] demonstrated direct evidence that localized electron states at grain boundaries were one of the origins to induce ferromagnetism in HOPG. Ohldag *et al.*[14] proved that the ferromagnetism found in graphite originates from carbon π-states and hydrogen-mediated electronic states. Ugeda *et al.*[15] explained the formation of local magnetic moments by single vacancies in graphite. Recently, defect-induced ferromagnetism was found in SiC[8,16–18]. Divacancies ($V_{Si}V_C$) are proven to exist in neutron irradiated and neon implanted SiC[8,17]. Thus a question arises whether it is possible to establish a one-to-one correlation between the local moments and the specific orbitals/electrons in SiC.

On the other hand, SiC has been well known as a kind of economical and practical abrasive and a semiconductor for its application in high-temperature and high-voltage semiconductor electronics. As to our work, the good crystalline quality and the low concentration of impurities (please compare the relevant data in Refs. 8,19,20) can remove the concerns whether the observed ferromagnetism originates from extrinsic factors (*e.g.* magnetic contamination, see Refs. 21,22). Moreover, the dynamics of defects and their charge states in SiC upon ion irradiation can be obtained by *ab initio* molecular dynamics simulations[23], rendering SiC an ideal testbed for the investigation of defect-induced ferromagnetism. Recent studies reveal that SiC could be a material with potential for applications in quantum optics and quantum information[24–27]. Therefore, direct experimental evidence for defect-induced ferromagnetism in SiC will have significant impact on other scientific areas related to defects.

In this paper, 6H-SiC single crystals irradiated with xenon ions are investigated to reveal the origin of its ferromagnetism. We present the results of X-ray absorption near-edge structure (XANES) and X-ray magnetic circular dichroism (XMCD) experiments at both the silicon and carbon K-edges in conjunction with sensitive magnetization measurements and first-principles calculations. These results show that the *p* electrons of the nearest-neighbor carbon atoms of $V_{Si}V_C$ are mainly responsible for the long-range ferromagnetic coupling. Our results provide important evidence for the origin of defect-induced ferromagnetism in SiC.

www.nature.com/scientificreports

Results

Magnetization measurements and sample selection. As a prerequisite step, the pristine SiC wafer was checked for trace elements by using particle induced X-ray emission. The amount of transition metal impurities (Fe, Co and Ni) proves to be below the detection limit of around 1 μg/g (result shown in Fig. S1 in the supplementary material). Figure 1(a) exhibits the hysteresis loops of all implanted samples after subtraction of the diamagnetic background. The inset of Fig. 1(a) shows magnetization vs. field for sample 5E12 and the pristine SiC measured at 5 K. The pristine SiC is primarily diamagnetic with a weak paramagnetic contribution (see Figs. S2–S4 in the supplementary material for details). As shown in Fig. 1(a), SiC becomes ferromagnetic upon Xe ion irradiation. The strongest magnetization occurs for the sample 5E12, which is the sample subjected to the lowest fluence and with the least damage to the crystallinity (refer to Fig. S5). With rising fluence, the saturation magnetization (*Ms*) decreases from 0.72 μ_B/vacancy to around 0.02 μ_B/vacancy. The decrease of *Ms* at large defect concentrations has also been observed in proton irradiated graphite[2,28]. This is very probably due to damage to the crystalline order or due to the unfavorable spin-polarization when the defects are too close to each other[29]. The hysteresis loops measured for the sample 5E12 at 5 K and 300 K after subtracting the magnetic background from the pristine sample are shown in Fig. 1(b), indicating *Ms* at 300 K is still around half of *Ms* at 5 K and the transition temperature is higher than 300 K. Therefore, we focus on the sample 5E12 in the following investigation.

Direct evidence for the origin of magnetism. XMCD spectroscopy as an element-specific technique has been used to measure the magnetic contribution from different elements with partially occupied 3*d* or 4*f* subshells[30,31]. Ohldag *et al.*[28] successfully applied this technique to investigate the magnetism at the carbon K-edge in proton irradiated HOPG. As it is possible to investigate the bonding state in SiC single crystals using XANES spectroscopy[32,33], it is also possible to explore the magnetic contribution in defect-induced ferromagnetism in SiC with soft X-ray spectroscopy. Figure 2(a) shows the XANES spectra of the silicon K-edge for selected samples to investigate the source of the observed ferromagnetism. Comparing with the pristine sample, the peak positions of samples after implantation are not changed, but the relative strength of the peak at 1848 eV decreases, which suggests an increase of defect density[34]. As shown in Fig. 2(b), the strength of the XMCD signal at the silicon K-edge is below the detection noise level in both the pristine sample and the sample 5E12. We may conclude that no spin-polarized states of 3*p* electrons occur at silicon atoms, and thus silicon centers do not contribute to the ferromagnetism observed in the sample 5E12. Figure 2(c) shows the XANES spectra at the carbon K-edge of the sample 5E12 and the pristine sample measured at 300 K. Resonances around 285 eV and 290 eV correspond to the transition of carbon 1*s* core-level electrons to π* and σ* bands, respectively[14,28]. The resonance at 285 eV of the sample 5E12 is sharper than that of the pristine sample, indicating that the orbital hybridization at carbon is modified from the diamond-like sp^3-type carbon in pure SiC towards a more planar, graphitic sp^2-type carbon center, which leaves the orthogonal p_z orbital unchanged and gives rise to the peak of π* bands[32]. This reflects a change of the local coordination from the tetrahedrally coordinated carbon atom in pristine SiC to the three-fold bound carbon site. In sharp contrast to the silicon K-edge, a clear XMCD signal appears at the carbon K-edge as shown in Fig. 2(d). Therefore,

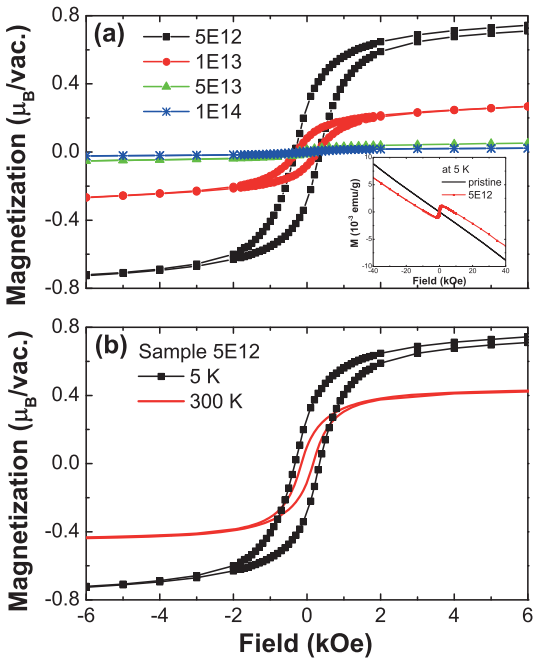

Figure 1 | (a) Ferromagnetic hysteresis loops of samples 5E12, 1E13, 5E13, 1E14 at 5 K after subtracting the magnetic background from the pristine sample. The inset shows the as-measured magnetization vs. field of the sample 5E12 and the pristine sample at 5 K. (b) Hysteresis loops of the sample 5E12 at 5 K and 300 K.

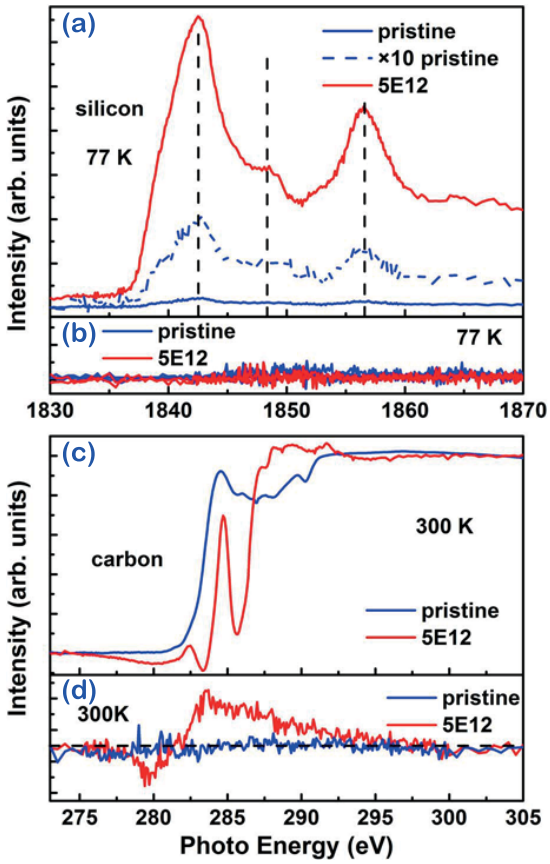

Figure 2 | X-ray absorption spectra measured in EY (electron yield) mode for the sample 5E12 and the pristine sample: (a) XANES of the silicon K-edge at 77 K, (b) XMCD at the silicon K-edge at 77 K, (c) XANES of the carbon K-edge at 300 K. (d) XMCD at the carbon K-edge at 300 K.

www.nature.com/scientificreports

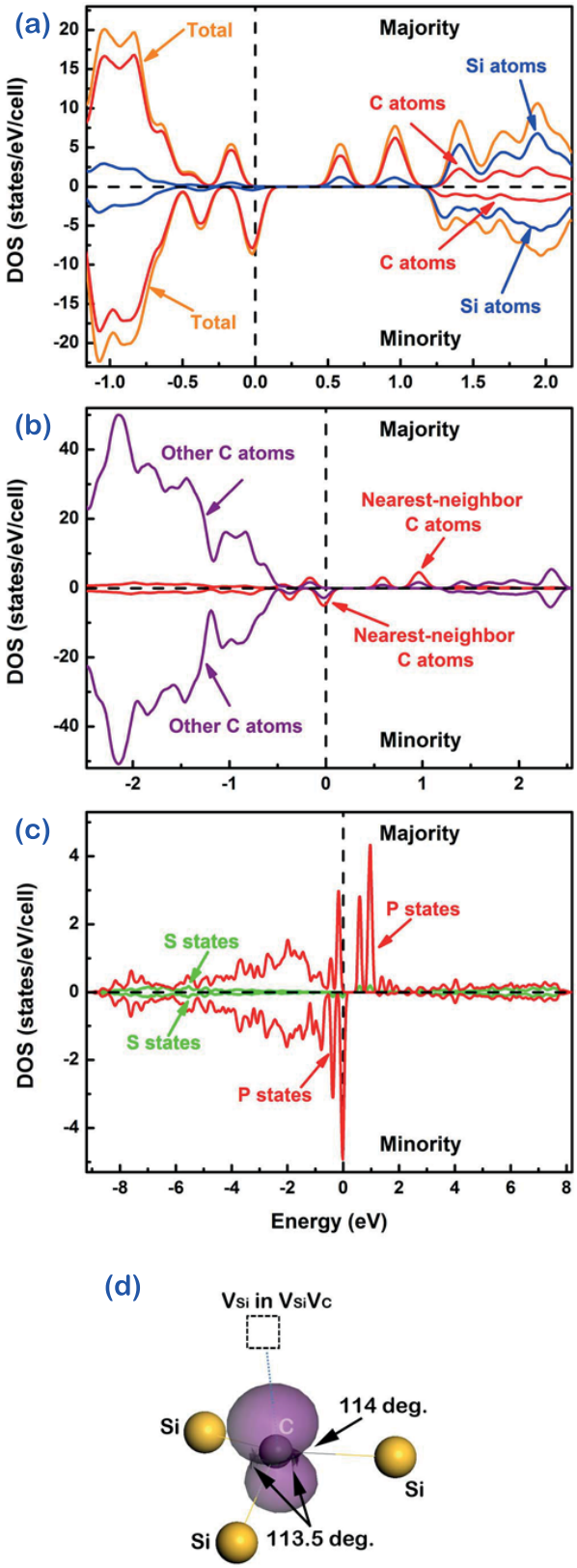

Figure 3 | The electronic structure of $Si_{95}(V_{Si})C_{95}(V_C)$: (a) The total spin-resolved DOS and the partial spin-resolved DOS of silicon atoms and carbon atoms, respectively. (b) Comparison of partial spin-resolved DOS of nearest-neighbor carbon atoms and others. (c) Comparison of the partial spin-resolved DOS of *s* and *p* electrons of nearest-neighbor carbon atoms of $V_{Si}V_C$. (d) The structure and spin density isosurface (0.08 e/Å^3, in purple) around one of the nearest-neighbor carbon atoms. The carbon atom is in grey in the middle and silicon atoms are in yellow. The arrows indicate the bond angles of Si-C-Si. The dashed line and square indicate the direction and the location of the adjacent silicon vacancy part (V_{Si}) within $V_{Si}V_C$, respectively.

the defect-induced ferromagnetism originates from a spin-polarized partial occupancy of the p_z orbitals at carbon atoms close to defect sites in SiC. It is worth noting that an XMCD peak at around 280 eV Fig. 2(d) appears well below the onset of the π* resonance. This peak was also observed in graphite[14]. This intriguing feature is not yet fully understood.

Discussion

According to the results provided by positron annihilation spectroscopy (see Figure S6 in the supplementary material), divacancies $V_{Si}V_C$ are the dominating defect type in our samples. Note that the nearest-neighbor atoms of $V_{Si}V_C$ include three carbon atoms as well as three silicon atoms. Why is the magnetic signal observed only at the carbon sites? To answer this question, first-principles calculations were employed. As shown in Fig. 3(a), 90% of the spin polarization with a total moment of 2 μ_B due to one divacancy $V_{Si}V_C$ is contributed by the valence states of the carbon atoms. This explains why XMCD is only observable at the carbon K-edge. Furthermore, when comparing the partial spin-resolved DOS of nearest-neighbor carbon atoms with that of other carbon atoms, it is visible [see Figure 3(b)] that 85% of the magnetic moments originate from the three nearest-neighbor carbon atoms. In the Si-C system, as carbon has higher electronegativity than silicon, unpaired electrons around carbon atoms should be more localized than those around silicon. A Mulliken population analysis indicates that in the unperturbed SiC bulk the Si-C bonds are already polar in accordance with the respective electronegativities: Partial charges of −0.32 e on carbon atoms and of +0.32 e on silicon atoms are calculated for the pristine bulk at the Mulliken level. In the vicinity of the divacancy carbon atoms show a trend towards larger partial charges (−0.38 e), whereas the silicon partial charges close to the divacancy are nearly unchanged. Spin polarization thus mainly appears at those carbon atoms that are located around the divacancies. According to Fig. 3(c), our calculation indicates that most of the magnetic moments (90%) originate from the *p* states of nearest-neighbor carbon atoms of $V_{Si}V_C$. Due to the attraction of the remaining adjacent silicon atoms, the nearest-neighbor carbon atoms will slightly move away from the $V_{Si}V_C$. This structure change from the unperturbed four-fold bulk coordination to a more planar three-fold bound state is connected with s-p-rehybridization at the C atoms in the close vicinity of $V_{Si}V_C$. Concomitantly, this distortion will modify the electronic structure locally towards a higher degree of sp^2 bonding orbitals and a singly occupied *p*-type lone pair at the C atoms. Thus those outermost orbitals will acquire significant π character and the magnetic moments are mainly contributed by *p* electrons, as shown in Fig. 3(d). This analysis corroborates our interpretation of the XMCD experiment: the XMCD signal of SiC after irradiation is thus assigned to *p* electrons.

In conclusion, in this work we investigated the magnetic properties of 6H-SiC after xenon irradiation. X-ray absorption spectroscopy at both the silicon and carbon K-edges combined with sensitive magnetization measurements and first-principles calculations are used to understand the origin of defect-induced ferromagnetism. The results give strong evidence that the *p* electrons of the nearest-neighbor carbon atoms of $V_{Si}V_C$ are mainly responsible for the observed ferromagnetism. These results provide valuable insight into

comprehending the phenomena of defect-induced ferromagnetism in SiC, graphitic and other carbon-based materials, and will encourage the exploration of the origin of defect-induced ferromagnetism in other promising materials such as graphene and oxides.

Methods

Sample preparation. A commercial one-side-polished semi-insulating 6H-SiC (0001) single crystal wafer was cut into pieces for ion irradiation. The concentrations of transition metal impurities (Fe, Co and Ni) prove to be below the detection limit of particle induced X-ray emission (see Fig. S1 in the supplementary material). Four SiC pieces were implanted by xenon ions with fluence values of 5×10^{12}, 1×10^{13}, 5×10^{13}, 1×10^{14} cm^{-2} at an energy of 500 keV at room temperature, which were subsequently labelled as 5E12, 1E13, 5E13, and 1E14, respectively. During implantation, the samples were tilted by 7 degrees to reduce the channelling effect. The corresponding displacements per atom (DPA) values have been calculated by Stopping and Range of Ions in Matter (SRIM)[35] to be 0.023, 0.047, 0.23, and 0.47, respectively. The distribution of irradiation-induced damage predicted by SRIM for xenon ions is more uniform and closer to the surface than that produced by 140 keV neon ions[17].

Measurements. All samples were measured with a superconducting quantum interference device (SQUID-MPMS or SQUID-VSM, Quantum Design). The magnetization is determined according to the total vacancies calculated using SRIM[35]. Both XANES and XMCD spectroscopies at the silicon and carbon K-edges were obtained at the Advanced Light Source (Berkeley Lab). The spectra of the silicon K-edge were measured at BL6.3.1 under a magnetic field of −2 and 2 T at 77 K, while the carbon K-edge spectra were measured at BL4.0.2 with the possibility of using a X-ray photon energy as low as 100 eV (note that the carbon K-edge is around 285 eV) and applying an external field of −0.5 and 0.5 T at 300 K. The typical spectral resolution for both beamlines is $E/\Delta E \sim 5000$ (see Ref. 14). In the measurements, total electron yield (EY) mode is chosen, which usually collects the signal from the topmost 5–10 nm of the sample[36].

Calculation parameters. First-principles calculations were performed using the Cambridge Serial Total Energy Package[37]. Spin-polarized electronic structure calculations were performed using the Perdew-Burke-Ernzerhof functional[38] for the exchange-correlation potential based on the generalized gradient approximation. The core-valence interaction was described by ultrasoft pseudopotentials[39], and to represent the self-consistently treated valence electrons the cutoff energy of the plane-wave basis was set to 310 eV. We calculated the total spin-resolved density of states (DOS) and the partial spin-resolved DOS of silicon atoms and carbon atoms in a $4 \times 4 \times 1$ *6H*-SiC supercell containing one axial $V_{Si}V_C$ [$Si_{95}(V_{Si})C_{95}(V_C)$]. The calculation presented in this paper is for neutral $V_{Si}V_C$. With the minimum distance between adjacent $V_{Si}V_C$ larger than 12 Å, this structure allows long-range ferromagnetic coupling[8]. The content of the spin polarization contribution is determined by comparing the integrated DOS below the Fermi level.

1. Coey, J. M. D., Venkatesan, M., Fitzgerald, C. B., Douvalis, A. P. & Sanders, I. S. Ferromagnetism of a graphite nodule from the Canyon Diablo meteorite. *Nature* **420**, 156–159 (2002).
2. Esquinazi, P. *et al.* Induced magnetic ordering by proton irradiation in graphite. *Phys. Rev. Lett.* **91**, 227201 (2003).
3. Yazyev, O. V. Magnetism in disordered graphene and irradiated graphite. *Phys. Rev. Lett.* **101**, 037203 (2008).
4. Venkatesan, M., Fitzgerald, C. B. & Coey, J. M. D. Unexpected magnetism in a dielectric oxide. *Nature* **430**, 630 (2004).
5. Osorio-Guillen, J., Lany, S., Barabash, S. V. & Zunger, A. Magnetism without magnetic ions: Percolation, exchange, and formation energies of magnetism-promoting intrinsic defects in CaO. *Phys. Rev. Lett.* **96**, 107203 (2006).
6. Araujo, C. M. *et al.* Room temperature ferromagnetism in pristine MgO thin films. *Appl. Phys. Lett.* **96**, 232505 (2010).
7. Yi, J. B. *et al.* Ferromagnetism in Dilute Magnetic Semiconductors through Defect Engineering: Li-Doped ZnO. *Phys. Rev. Lett.* **104**, 137201 (2010).
8. Liu, Y. *et al.* Defect-Induced Magnetism in Neutron Irradiated 6H-SiC Single Crystals. *Phys. Rev. Lett.* **106**, 087205 (2011).
9. Yazyev, O. V. & Helm, L. Defect-induced magnetism in graphene. *Phys. Rev. B* **75**, 125408 (2007).
10. Nair, R. R. *et al.* Dual origin of defect magnetism in graphene and its reversible switching by molecular doping. *Nat. Commun.* **4**, 2010 (2013).
11. Chen, L. L. *et al.* Towards intrinsic magnetism of graphene sheets with irregular zigzag edges. *Sci. Rep.* **3**, 2599 (2013).
12. Yazyev, O. V. Emergence of magnetism in graphene materials and nanostructures. *Rep Prog Phys* **73**, 056501 (2010).
13. Červenka, J., Katsnelson, M. I. & Flipse, C. F. J. Room-temperature ferromagnetism in graphite driven by two-dimensional networks of point defects. *Nat. Phys.* **5**, 840–844 (2009).
14. Ohldag, H. *et al.* The role of hydrogen in room-temperature ferromagnetism at graphite surfaces. *New J. Phys.* **12**, 123012 (2010).
15. Ugeda, M. M., Brihuega, I., Guinea, F. & Gómez-Rodríguez, J. M. Missing Atom as a Source of Carbon Magnetism. *Phys. Rev. Lett.* **104**, 096804 (2010).
16. Song, B. *et al.* Observation of Glassy Ferromagnetism in Al-Doped 4H-SiC. *J. Am. Chem. Soc.* **131**, 1376–1377 (2009).
17. Li, L. *et al.* Rise and fall of defect induced ferromagnetism in SiC single crystals. *Appl. Phys. Lett.* **98**, 222508 (2011).
18. Wang, Y. *et al.* Disentangling defect-induced ferromagnetism in SiC. *Phys. Rev. B* **89**, 014417 (2014).
19. Janzén, E. *et al.* [Defects in SiC] *Defects in Microelectronic Materials and Devices* [Fleetwood, D. M., Pantelides, S. T. & Schrimpf, R. D. (ed.)] (Taylor & Francis, Hoboken, NJ, 2008).
20. Esquinazi, P. *et al.* Magnetic order in graphite: Experimental evidence, intrinsic and extrinsic difficulties. *J. Magn. Magn. Mater.* **322**, 1156–1161 (2010).
21. Nair, R. R. *et al.* Spin-half paramagnetism in graphene induced by point defects. *Nat. Phys.* **8**, 199–202 (2012).
22. Khalid, M. *et al.* Ubiquity of ferromagnetic signals in common diamagnetic oxide crystals. *Phys. Rev. B* **81**, 214414 (2010).
23. Gao, F., Xiao, H. Y., Zu, X. T., Posselt, M. & Weber, W. J. Defect-Enhanced Charge Transfer by Ion-Solid Interactions in SiC using Large-Scale Ab Initio Molecular Dynamics Simulations. *Phys. Rev. Lett.* **103**, 027405 (2009).
24. Koehl, W. F., Buckley, B. B., Heremans, F. J., Calusine, G. & Awschalom, D. D. Room temperature coherent control of defect spin qubits in silicon carbide. *Nature* **479**, 84–87 (2011).
25. Falk, A. L. *et al.* Polytype control of spin qubits in silicon carbide. *Nat. Commun.* **4**, 1819 (2013).
26. Castelletto, S. *et al.* A silicon carbide room-temperature single-photon source. *Nat. Mater.* **13**, 151–156 (2014).
27. Kraus, H. *et al.* Room-temperature quantum microwave emitters based on spin defects in silicon carbide. *Nat. Phys.* **10**, 157–162 (2014).
28. Ohldag, H. *et al.* π-Electron Ferromagnetism in Metal-Free Carbon Probed by Soft X-Ray Dichroism. *Phys. Rev. Lett.* **98**, 187204 (2007).
29. Wang, Y. *et al.* Defect-induced magnetism in SiC: why the ferromagnetic signal is weak. *arXiv preprint*, arXiv:1501.01096 (2015).
30. Schütz, G. *et al.* Absorption of Circularly Polarized X-Rays in Iron. *Phys. Rev. Lett.* **58**, 737–740 (1987).
31. Stöhr, J., Padmore, H. A., Anders, S., Stammler, T. & Scheinfein, M. R. Principles of X-ray magnetic dichroism spectromicroscopy. *Surf. Rev. Lett.* **5**, 1297–1308 (1998).
32. Gao, X. Y. *et al.* Disorder beneath epitaxial graphene on SiC(0001): An x-ray absorption study. *Phys. Rev. B* **78**, 201404 (2008).
33. Ohkubo, M. *et al.* X-ray absorption near edge spectroscopy with a superconducting detector for nitrogen dopants in SiC. *Sci. Rep.* **2**, 831 (2012).
34. Dedkov, Y. S. & Fonin, M. Electronic and magnetic properties of the graphene–ferromagnet interface. *New J. Phys.* **12**, 125004 (2010).
35. James, J., Ziegler, F., Biersack, J. P. & Littmark, U. *The Stopping and Range of Ions in Solids* (Pergamon, Oxford, 1985).
36. Stöhr, J. & Siegmann, H. C. *Magnetism - From Fundamentals to Nanoscale Dynamics* (Springer, Heidelberg, 2006).
37. Clark, S. J. *et al.* First principles methods using CASTEP. *Z. Kristallogr.* **220**, 567–570 (2005).
38. Perdew, J. P., Burke, K. & Ernzerhof, M. Generalized gradient approximation made simple. *Phys. Rev. Lett.* **77**, 3865–3868 (1996).
39. Vanderbilt, D. Soft Self-Consistent Pseudopotentials in a Generalized Eigenvalue Formalism. *Phys. Rev. B* **41**, 7892–7895 (1990).

Acknowledgments

The work is financially supported by the Helmholtz-Gemeinschaft Deutscher Forschungszentren (VH-NG-713, VH-VI-442 and VH-PD-146). Y. Wang thanks the China Scholarship Council (File No. 2010675001) for supporting his stay at HZDR. The Advanced Light Source is supported by the U.S. Department of Energy under Contract No. DE-AC02-05CH11231. G. Wang, and X. L. Chen also thank the support by the National Natural Science Foundation of China (Grant Nos. 51322211, 90922037, 51072222 and 51272276).

Author contributions

S.Z. conceived the experiment. Y.W. prepared the samples and performed the measurements for magnetic properties. Y.L. and G.W. made the calculation. W.A. carried out the PAS experiment. F.M. did the PIXE measurement. C.J. and E.A. assistant the XAS experiment. O.G., G.S. and D.Z. performed the Raman measurements. S.G., X.C. and M.H. supervised the work. All authors have participated the manuscript preparation and discussion.

Additional information

Supplementary information accompanies this paper at http://www.nature.com/scientificreports

Competing financial interests: The authors declare no competing financial interests.

How to cite this article: Wang, Y. *et al.* Carbon *p* Electron Ferromagnetism in Silicon Carbide. *Sci. Rep.* 5, 8999; DOI:10.1038/srep08999 (2015).

www.nature.com/scientificreports

Langmuir
Article
pubs.acs.org/Langmuir

Alignment of Gold Nanoparticle-Decorated DNA Origami Nanotubes: Substrate Prepatterning versus Molecular Combing

Bezu Teschome,*[,†,‡] Stefan Facsko,[†] Kurt V. Gothelf,[§] and Adrian Keller[∥]

[†]Institute of Ion Beam Physics and Materials Research, Helmholtz-Zentrum Dresden-Rossendorf, 01328 Dresden, Germany
[‡]Technische Universität Dresden, Mommsenstraße 13, 01069 Dresden, Germany
[§]Danish National Research Foundation: Centre for DNA Nanotechnology (CDNA) at Interdisciplinary Nanoscience Center (iNANO) and Department of Chemistry, Aarhus University, 8000 Aarhus C, Denmark
[∥]Technical and Macromolecular Chemistry, University of Paderborn, Warburger Str. 100, 33098 Paderborn, Germany

Supporting Information

ABSTRACT: DNA origami has become an established technique for designing well-defined nanostructures with any desired shape and for the controlled arrangement of functional nanostructures with few nanometer resolution. These unique features make DNA origami nanostructures promising candidates for use as scaffolds in nanoelectronics and nanophotonics device fabrication. Consequently, a number of studies have shown the precise organization of metallic nanoparticles on various DNA origami shapes. In this work, we fabricated large arrays of aligned DNA origami decorated with a high density of gold nanoparticles (AuNPs). To this end, we first demonstrate the high-yield assembly of high-density AuNP arrangements on DNA origami adsorbed to Si surfaces with few unbound background nanoparticles by carefully controlling the concentrations of $MgCl_2$ and AuNPs in the hybridization buffer and the hybridization time. Then, we evaluate two methods, i.e., hybridization to prealigned DNA origami and molecular combing in a receding meniscus, with respect to their potential to yield large arrays of aligned AuNP-decorated DNA origami nanotubes. Because of the comparatively low $MgCl_2$ concentration required for the efficient immobilization of the AuNPs, the prealigned DNA origami become mobile and displaced from their original positions, thereby decreasing the alignment yield. This increased mobility, on the other hand, makes the adsorbed origami susceptible to molecular combing, and a total alignment yield of 86% is obtained in this way.

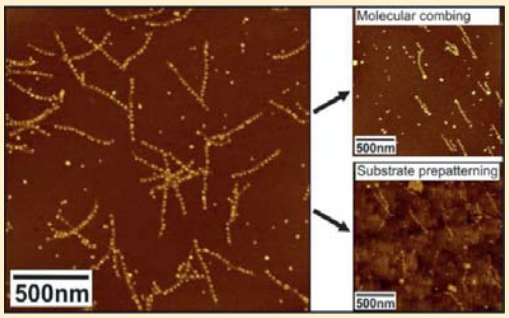

INTRODUCTION

The controlled arrangement of metallic nanoparticles on conventional surfaces has received a great deal of attention due to their potential applications in nanoelectronics, plasmonics, and sensor devices.[1] In the past, various routes for the organization of nanoparticles on technologically relevant surfaces have been explored.[2−5] Among several methods, DNA-directed self-assembly, and particularly DNA origami,[6] has proven to be an effective method and has been extensively employed for the precise positioning of noble metal nanoparticles with few nanometer resolution.[7−16] DNA origami is a method developed by Rothemund to create well-defined nanostructures with any desired shape by folding a long single-stranded DNA scaffold using multiple short synthetic staple strands.[6] A particular advantage of DNA origami is the possibility to modify selectively some of the staple strands to enable site-specific attachment of functional nanostructures. Hence, this method has become a key technique to assemble nanoparticles into 1D, 2D, and 3D geometries.

Recently, a number of studies have shown the precise organization of gold nanoparticles (AuNPs) on various shapes of DNA origami. In most experiments either 2D[7−9,11,13,17] DNA origami such as rectangular and triangular shapes or quasi-one-dimensional DNA origami nanotubes[12,15,16,18−20] have been employed as templates to assemble AuNPs. Similarly, also the controlled placement of various DNA origami nanostructures on technologically relevant surfaces has been investigated in depth.[21−29] Yet, only few studies have attempted to control the orientation of nanoparticle-decorated DNA origami nanostructures on conventional surfaces.[9,21] Nevertheless, controlling the arrangement of nanoparticle functionalized DNA origami over large areas is indispensible in order to integrate such DNA-based materials into nanoelectronic and plasmonic devices.

Although few researchers have reported the positioning of ordered arrays of AuNP-functionalized DNA origami on surfaces,[9,21] virtually all of these approaches rely on electron-beam lithography which seriously limits sample throughput, especially when large homogeneous surface areas are required. Besides, only small numbers of AuNPs have been assembled on

Received: July 13, 2015
Revised: October 13, 2015
Published: October 31, 2015

DOI: 10.1021/acs.langmuir.5b02569
Langmuir 2015, 31, 12823−12829

the DNA origami while high AuNP densities are required for instance to fabricate plasmonic waveguides[19] or as seeds for further DNA origami metallization.[30] However, decorating DNA origami nanostructures with large AuNP numbers will alter the solution shape of the DNA origami−AuNP conjugates,[31,32] which may hinder their controlled deposition on the patterned surfaces. This problem can be overcome by performing nanoparticle assembly on immobilized and prealigned DNA origami. However, one of the major experimental difficulties of assembling high-density nanoparticle arrays on the surface is removing the unbound, randomly adsorbed background nanoparticles. In solution-based assemblies, the unbound nanoparticles can be removed by gel extraction, gel filtration, magnetic beads, etc.[33] Therefore, in this work, we first demonstrate the high-yield assembly of high-density AuNP arrays on DNA origami adsorbed to Si surfaces with few unbound background nanoparticles by carefully controlling the concentrations of $MgCl_2$ and AuNPs in the hybridization buffer and the hybridization time. Then, we evaluate two methods, i.e., hybridization to prealigned DNA origami and molecular combing, with respect to their potential to yield large arrays of aligned AuNP-decorated DNA origami nanotubes. Molecular combing is a well-known technique used to align and to stretch double-stranded DNA along a certain substrate direction by applying a receding meniscus moving across the substrate surface.[34] Using this technique, we achieve a total alignment yield of 86% for DNA origami nanotubes decorated with 14 AuNPs, thus creating a promising route toward the large-area integration of DNA-based materials into nanoelectronic and plasmonic devices.

■ EXPERIMENTAL SECTION

In this work, we used DNA origami nanotubes (six-helix bundles), adopting the design of Bui et al.[35] The self-assembly of the DNA origami nanotubes was performed as previously described using the M13mp18 viral DNA scaffold (New England Biolabs) and 170 staple strands.[28] To enable the binding of 14 DNA-coated AuNPs, 28 staple strands, i.e., two strands per nanoparticle, were modified by elongating each strand with a capture sequence 5′-$(AAT)_8T_4$-3′ on their 5′ end (see Supporting Information for the full sequences of the modified strands).

Commercially available, citrate-stabilized 5 nm AuNPs (BBI) were coated with 3′ disulfide-modified oligonucleotides of the sequence 5′-$(ATT)_3T_4$-3′ as described previously.[13] Under our experimental conditions, these oligonucleotides have a melting temperature above 25 °C, so that efficient hybridization can be carried out at room temperature. All staple strands and the disulfide-modified oligonucleotides were purchased from Metabion. UV/vis spectroscopy was used to estimate the final AuNP concentration of the purified solution from the optical absorbance at 520 nm.

All nanoparticle assemblies were performed on commercially available epi-polished p-Si(100) wafers with native surface oxide at room temperature. Nanoscale ripple patterns with 30 nm periodicity were fabricated on the Si substrates by off-normal low-energy Ar^+ irradiation as previously reported.[36] Prior to DNA origami adsorption, the Si substrate was treated in an oxygen plasma for 3 min and subsequently rinsed with ethanol and Milli-Q water followed by drying in a stream of N_2. The DNA origami solution (concentration ∼1 nM) was then incubated for 1 h in 10 × TAE buffer containing 200 mM $MgCl_2$ in a humidity chamber. After adsorption, the substrate was dipped in a 1:1 mixture of ethanol and Milli-Q water for 30 s to remove residual salt from the surface and dehydrate the DNA origami. After drying in a N_2 stream oriented ∼45° with respect to the edge of the substrate, the adsorbed DNA origami was imaged and characterized by tapping mode atomic force microscopy (AFM) in air using a Bruker MultiMode 8 scanning probe microscope and PPP-NCLR cantilevers from Nanosensors (nominal force constant 48 N m^{-1}, tip radius <10 nm).

Hybridization of AuNPs to the immobilized DNA origami was performed by incubating 30 or 50 nM DNA-coated AuNPs on the substrate surface for 10 or 20 min at room temperature in 1 × TAE buffer containing 20 or 50 mM $MgCl_2$. After incubation, the substrate was first dipped in Milli-Q water for 10 s to remove the unbound DNA-coated AuNPs, then dipped again in a 1:1 mixture of ethanol and Milli-Q water for 30 s, and subsequently dried in a stream of N_2. Because of the higher surface tension of pure water compared to the ethanol/water mixture, this first dip was found to be more efficient in removing unbound background AuNPs. The AuNP-decorated DNA origami were again imaged and characterized by AFM. Analysis of the number of attached AuNPs per DNA origami and the orientation of the AuNP-functionalized DNA origami on the different substrates have been determined from 5 to 10 AFM images taken at different positions on the surface of each substrate. Values represent averages over four replicates with standard deviations given as errors. For each value, up to 220 DNA origami have been analyzed. The orientation of the AuNP-decorated DNA origami nanotubes was determined by measuring the angle between the nanotube and their anticipated direction of alignment as described previously.[28] All the topographic AFM images have 15 nm height scale and were analyzed using Gwyddion open source software.[37]

■ RESULTS AND DISCUSSION

For our experiments, we chose DNA origami six-helix bundle nanotubes with a length of 412 nm and diameter of 6 nm due to their promising application as scaffolds for nanoelectronic and plasmonic device fabrication.[19] For the attachment of 5 nm AuNPs, 28 staple strands at specific positions along the DNA origami nanotube axis were extended by adding a capture sequence on their 5′ end to create 14 binding sites, where each binding site consists of two capture strands of identical sequence that protrude from two neighboring helices. To avoid binding of individual AuNPs to two adjacent binding sites, a distance between binding sites of 30 nm was chosen. Figure 1 shows a schematic representation of the DNA-coated AuNPs and the DNA origami nanotube before and after AuNP hybridization.

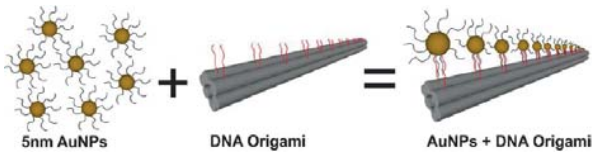

Figure 1. Schematic representation of the DNA-coated AuNPs and the modified DNA origami nanotubes before and after hybridization. To enable the attachment of the DNA-coated AuNPs, some of the staple strands used for DNA origami assembly were elongated with the capturing sequences.

Figure 2a shows an AFM height image of DNA origami nanotubes adsorbed on a flat Si/SiO_2 surface. In order to achieve moderately dispersed origami on the surface, the concentrations of DNA origami required for 1 h incubation in 10 × TAE buffer containing 200 mM $MgCl_2$ was first optimized. Hence, for all the following experiments, 20 μL of a 1 nM DNA origami solution were used for a 10 × 10 mm^2 Si/SiO_2 substrate. Since the high Mg^{2+} concentration of the adsorption buffer induces the aggregation of the AuNPs, the DNA origami were first adsorbed to the Si/SiO_2 surface, after which excess salt was removed with ethanol and Milli-Q water.

DOI: 10.1021/acs.langmuir.5b02569
Langmuir 2015, 31, 12823−12829

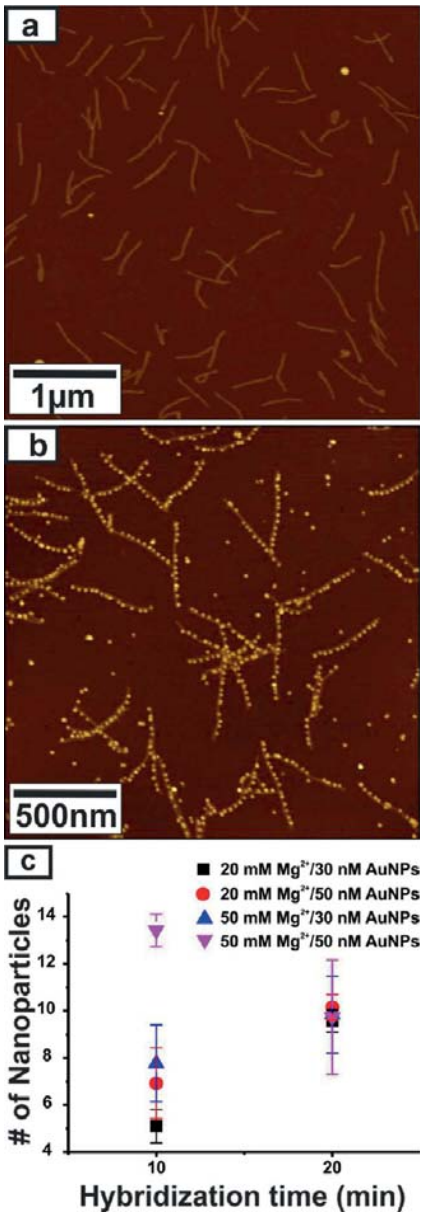

Figure 2. AFM height images and attachment yield of AuNPs for various conditions. (a) Immobilized DNA origami nanotubes on a flat Si surface. (b) AuNPs attached along the immobilized DNA origami nanotubes using 50 mM Mg^{2+}/50 nM AuNPs and 10 min incubation. (c) AuNPs attachment yield for different Mg^{2+} concentrations, AuNP concentrations, and hybridization times. The data were obtained by counting the AuNPs bound to the individual DNA origami.

Then AuNP hybridization was performed on the dried sample in 1 × TAE buffer having a lower Mg^{2+} concentration.

For optimizing the attachment of 5 nm AuNPs, the effects of Mg^{2+} concentration (20 and 50 mM in 1 × TAE), AuNP concentrations (30 and 50 nM), and hybridization time (10 and 20 min) have been evaluated. The results of the statistical analysis are presented in Figure 2c. The highest attachment yield of >96% (corresponding to 13−14 AuNPs) with few unbound background nanoparticles is obtained for 10 min incubation of 50 nM DNA-coated AuNPs in buffer containing 50 mM Mg^{2+}. A corresponding AFM image is shown in Figure 2b. At lower AuNP and Mg^{2+} concentrations, drastically lower attachment yields are observed. Increasing the hybridization time to 20 min leads to a significant increase of the attachment yield for lower Mg^{2+} and AuNP concentrations. Nevertheless, binding yields for 20 min hybridization do not exceed 70%. In addition, the density of unbound background nanoparticles also increases with hybridization time. This phenomenon is clearly visible in the AFM images shown in Figure 3 for three different

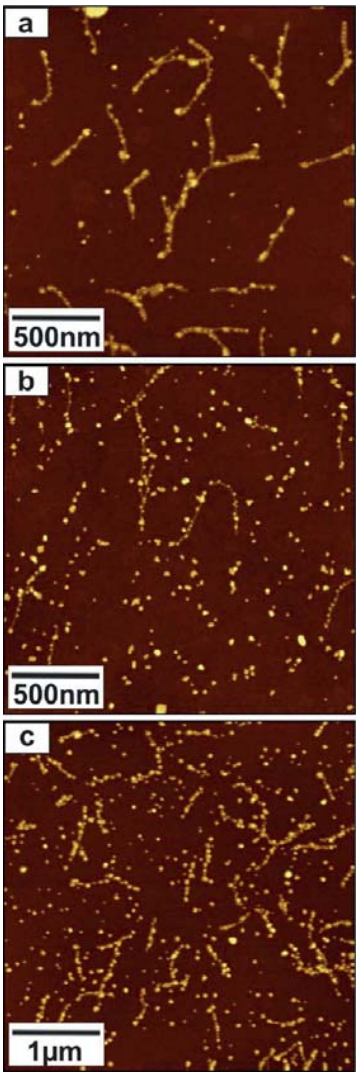

Figure 3. AFM images for 20 min hybridization time and different Mg^{2+} and AuNP concentrations: (a) 20 mM Mg^{2+}, 30 nM AuNPs; (b) 20 mM Mg^{2+}, 50 nM AuNPs; (c) 50 mM Mg^{2+}, 50 nM AuNPs.

buffer and AuNP concentrations and a hybridization time of 20 min. Especially concentrations of 50 nM AuNPs and 50 mM Mg^{2+} result in a very large density of unbound background AuNPs (Figure 3c). Besides, some of the AuNPs bound to the DNA origami form clusters and appear larger than the actual size of individual AuNPs. Those clusters have not been included in the statistical analysis which explains the observed reduction of the overall binding yield for 20 min hybridization in the case of the high Mg^{2+} and AuNP concentrations. By lowering the Mg^{2+} concentration to 20 mM and the AuNP concentration to 30 nM at constant 20 min hybridization time

DOI: 10.1021/acs.langmuir.5b02569
Langmuir 2015, 31, 12823−12829

(Figure 3a), the density of unbound background AuNPs can be effectively reduced. Interestingly, for 20 min incubation, there is no pronounced effect of the Mg^{2+} and the AuNP concentrations on the attachment yield. Therefore, the delicate interplay of these three factors, i.e. Mg^{2+} concentration, AuNP concentration, and hybridization time, has to be taken into account not only in optimizing the attachment yield but also in avoiding unbound background nanoparticles on the Si/SiO_2 surface. This finding is consistent with recently published results.[20] The effect of temperature on the AuNPs attachment yield was found to be insignificant in the range from about 15 °C to about 25 °C. We however expect that much lower hybridization temperatures or temperatures too close to the melting temperature of the oligonucleotides will result in a reduction of the attachment yield.

In the next step, we applied the optimized protocol, i.e., 10 min hybridization of 50 nM AuNPs in 1 × TAE with 50 mM Mg^{2+}, for AuNP attachment to aligned DNA origami nanotubes on prepatterned surfaces. Recently, we demonstrated the self-alignment of DNA origami nanotubes on silicon surfaces exhibiting self-organized nanoscale ripple patterns produced by ion irradiation.[28] By optimizing the nanopattern dimensions and the ionic strength of the adsorption buffer, we were able to produce arrays of aligned DNA origami nanotubes due to surface topography and electrostatic interactions between the DNA origami and the patterned surface. In particular, for a ripple pattern with 30 nm periodicity we could achieve an alignment yield >70% for the same type of DNA origami nanotube as used in the present work. We therefore prepared and characterized nanopatterned surfaces with 30 nm periodicity for this experiment (Figure 4a). Then, the DNA origami were adsorbed on the nanorippled surface. Figure 4b shows an AFM phase image of the adsorbed DNA origami on the nanopatterned surface where most of the DNA origami nanotubes are located in the ripple valleys and follow the pattern direction. For a better visualization, four nanotubes are highlighted and shown as zooms below the phase image.

After the DNA origami adsorption on the nanorippled surfaces, the substrates were dipped and dried as described above while taking care not to displace the aligned DNA origami nanotubes.[28] Immediately after drying, AuNP hybridization was performed using the optimized protocol. The result is shown in Figure 5a,b. Surprisingly, the AuNP attachment is found to displace the DNA origami nanotubes and dislocates them from their original positions in the ripple valleys. This phenomenon is also reflected in the angular distribution of the AuNP-decorated DNA origami nanotubes shown in Figure 5c. Less than 50% of the 116 AuNP-functionalized DNA origami nanotubes analyzed are aligned within ±10° with respect to the ripple direction. Prior to AuNP attachment, alignment yields of 70% are routinely obtained.[28] We attribute this observation to the fact that the buffer for AuNPs assembly contains only 50 mM $MgCl_2$ instead of the 200 mM used for the DNA origami adsorption. Therefore, some of the adsorbed Mg^{2+} ions responsible for the charge inversion of the negatively charged Si/SiO_2 surface may be released from the surface which will decrease the electrostatic attraction between surface and DNA origami, thereby increasing the mobility of the adsorbed DNA origami.[38] In addition, since the dimensions of the AuNP-functionalized DNA origami are larger than those of the unmodified DNA origami, the shallow ripple pattern may not provide sufficient lateral confinement to keep the structures inside the ripple valleys.[28]

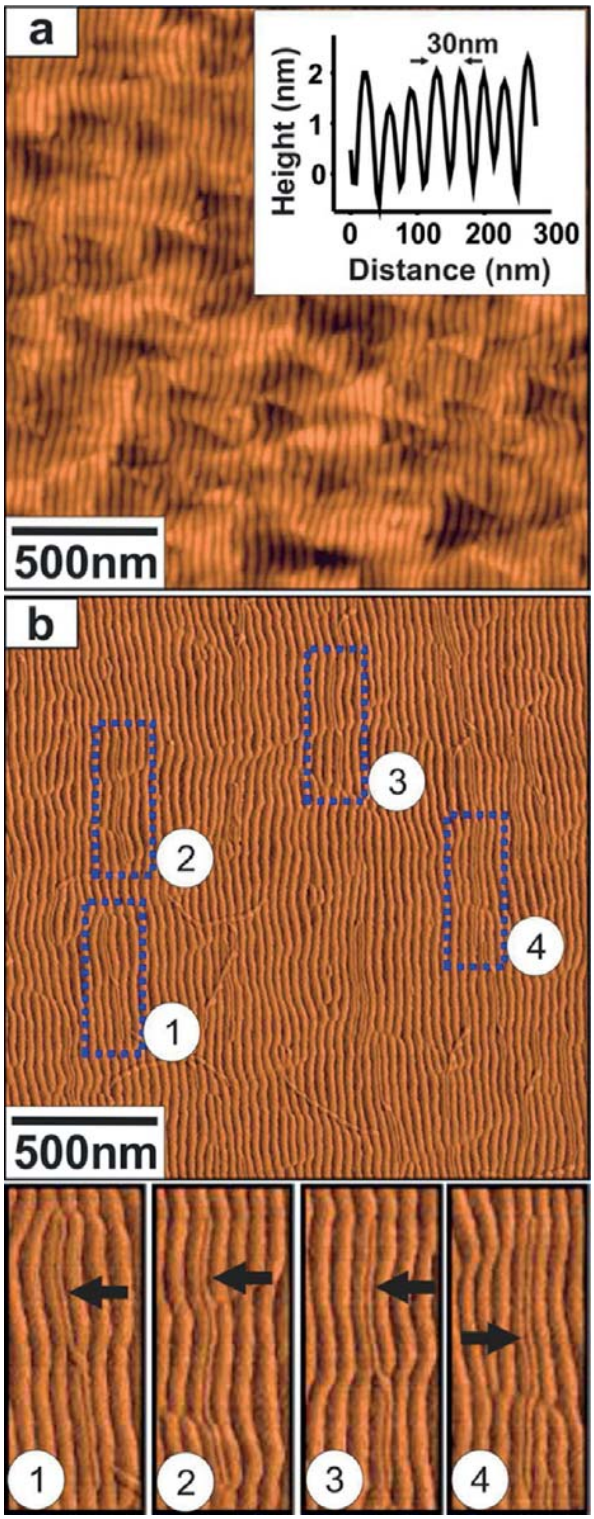

Figure 4. AFM height image (a) with corresponding line scan (inset) of a nanopatterned Si surface with 30 nm periodicity and AFM phase image (b) of immobilized DNA origami nanotubes on the nanopatterned Si surface. Four nanotubes are highlighted and shown as zooms below the phase image. The black arrows indicate the location of individual DNA origami nanotubes.

DOI: 10.1021/acs.langmuir.5b02569
Langmuir 2015, 31, 12823−12829

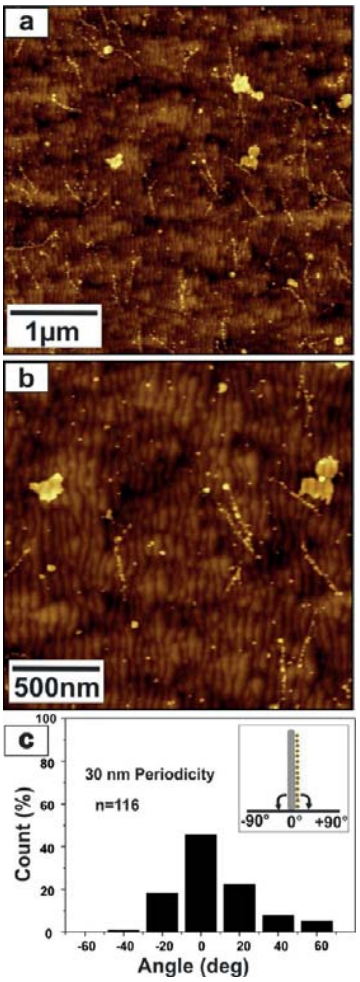

Figure 5. AFM images (a, b) and angular distribution (c) of AuNP-decorated DNA origami nanotubes adsorbed to nanopatterned Si surfaces. The angular distribution has been analyzed by measuring the angle of each AuNP-functionalized DNA origami nanotube with respect to the ripple direction (inset). The ripple direction is defined as a 0° angle.

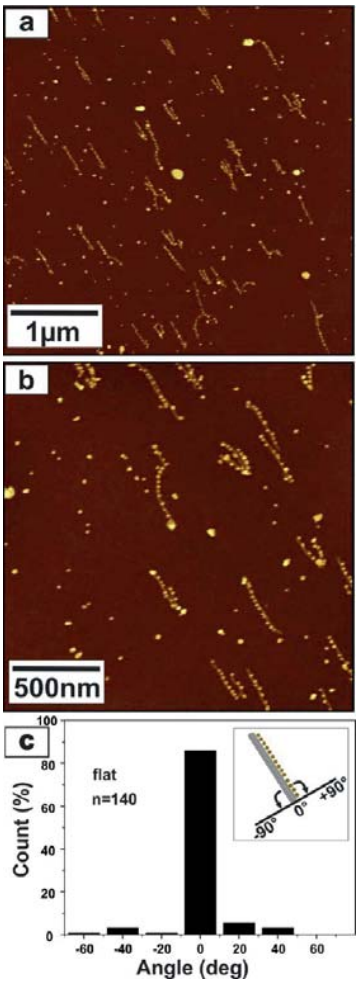

Figure 6. AFM images (a, b) and angular distribution (c) of AuNP-decorated DNA origami nanotubes adsorbed to flat Si surfaces. The angular distribution has been analyzed by measuring the angle of each AuNP-functionalized DNA origami nanotube with respect to the anticipated alignment direction (inset). The direction of movement of the receding meniscus is assigned to an angle of 0°.

However, since the low-magnesium buffer used for AuNP attachment seemed to enhance the mobility of the AuNP-decorated DNA origami nanotubes, we speculated that this effect might make them more susceptible to molecular combing. For DNA origami nanotubes adsorbed to Si/SiO_2 surfaces with the aid of high Mg^{2+} concentrations, molecular combing did not result in any alignment.[28] Enhancing their mobility on the surface by a reduction of the Mg^{2+} concentration after the initial adsorption might enable the flow-induced alignment of the DNA origami nanotubes. In our approach, after the AuNP hybridization, the substrate was first dipped in Milli-Q water for 10 s and dipped again in a 1:1 mixture of ethanol and Milli-Q water for 30 s. In order to evaluate the effect of molecular combing, a flat Si/SiO_2 surface with immobilized AuNP-decorated DNA origami was withdrawn both from the Milli-Q water and the ethanol−water mixture in the same direction. Furthermore, also the stream of N_2 used for drying the sample was applied along this very direction. Figure 6a,b shows AFM height images of the AuNP-functionalized DNA origami nanotubes after molecular combing. Preferential alignment along the withdrawal direction is clearly evident. The histogram shown in Figure 6c gives the angular distribution of the combed AuNP-decorated DNA origami nanotubes. The observed distribution reveals a total alignment yield of ∼86% from 140 AuNP-functionalized DNA origami, thus demonstrating the applicability of molecular combing for aligning AuNP-decorated DNA origami nanotubes. However, as can be seen in the AFM images in Figure 6a,b, some of the AuNP-decorated DNA origami nanotubes seem to be pinned to the surface at random positions along the tube axis, presumably by the attachment of AuNP aggregates of higher mass. This pinning then results in a deformation of the DNA origami nanotube during molecular combing, so that the nanotube is kinked at the immobile pinning site with the mobile nanotube segments being aligned in the flow. About 14% of all AuNP-DNA origami nanotubes exhibit such a deformed U shape. Therefore, we find that in total 86% of all DNA origami nanotubes are aligned, but only 72% remain structurally intact while 14% are aligned but kinked or bent.

DOI: 10.1021/acs.langmuir.5b02569
Langmuir 2015, 31, 12823−12829

Using more rigid DNA origami nanotubes such as 12-helix bundles may however reduce the fraction of kinked nanotubes.

The described molecular combing method has been applied also to nanorippled surfaces, with the receding meniscus moving along the direction of the ripples. However, no significant enhancement of the alignment yield compared to Figure 6c was observed. This can be attributed to the shallow depth of only ~2 nm of the ripple pattern which therefore does not provide sufficient lateral confinement in order to guide the AuNP-decorated DNA origami during molecular combing. The combination of molecular combing with deeper, groove-like patterns might however result in a further increase of the alignment yield.

■ CONCLUSIONS

In summary, we have demonstrated the high-yield synthesis of high-density AuNP arrangements on DNA origami nanotubes with few unbound background nanoparticles by carefully controlling the concentration of $MgCl_2$ in the hybridization buffer, the concentration of AuNPs, and the hybridization time. We have then applied the developed protocol for AuNP attachment to prealigned DNA origami nanotubes on nanorippled Si/SiO_2 surfaces. AuNP attachment was found to result in a significant decrease of the alignment yield, which we attribute to the reduced Mg^{2+} concentration in the hybridization buffer as compared to the high concentration used for DNA origami adsorption. This reduced Mg^{2+} concentration, however, increased the mobility of the AuNP-decorated DNA origami nanotubes and rendered them susceptible toward molecular combing. Using this approach, a total alignment yield of 86% was achieved. Although molecular combing does not provide the same versatility as topography-controlled self-alignment, its simplicity in combination with the high alignment yields makes it a very attractive method. Especially applications that do not require complex arrangements of the AuNPs but rather rely on arrays of parallel nanoparticle chains or nanowires over large surface areas, e.g., the fabrication of dichroic filters[39] or transparent conductive electrodes,[40] may benefit from this technique. In addition, the occurrence of deformed U-shaped AuNP-decorated DNA origami nanotubes may be minimized in future experiments by using more rigid DNA origami nanotubes.

■ ASSOCIATED CONTENT

Ⓢ Supporting Information

The Supporting Information is available free of charge on the ACS Publications website at DOI: 10.1021/acs.langmuir.5b02569.

The full sequences of the 28 modified staple strands (PDF)

■ AUTHOR INFORMATION

Corresponding Author

*E-mail b.teschome@hzdr.de (B.T.).

Notes

The authors declare no competing financial interest.

■ ACKNOWLEDGMENTS

This work was kindly supported by the Initiative and Networking Fund of the Helmholtz Association of German Research Centers through the International Helmholtz Research School for Nanoelectronic Networks, IHRS NANONET (VH-KO-606). The authors thank B. Schreiber for performing the ion irradiations.

■ REFERENCES

(1) Shipway, A. N.; Katz, E.; Willner, I. Nanoparticle Arrays on Surfaces for Electronic, Optical, and Sensor Applications. *ChemPhysChem* **2000**, *1* (1), 18−52.

(2) Shenhar, R.; Norsten, T. B.; Rotello, V. M. Polymer-Mediated Nanoparticle Assembly: Structural Control and Applications. *Adv. Mater.* **2005**, *17* (6), 657−669.

(3) Lin, C.; Liu, Y.; Rinker, S.; Yan, H. DNA Tile Based Self-Assembly: Building Complex Nanoarchitectures. *ChemPhysChem* **2006**, *7* (8), 1641−1647.

(4) Aldaye, F. A.; Palmer, A. L.; Sleiman, H. F. Assembling Materials with DNA as the Guide. *Science* **2008**, *321* (5897), 1795−1799.

(5) Sharma, J.; Ke, Y.; Lin, C.; Chhabra, R.; Wang, Q.; Nangreave, J.; Liu, Y.; Yan, H. DNA-Tile-Directed Self-Assembly of Quantum Dots into Two-Dimensional Nanopatterns. *Angew. Chem., Int. Ed.* **2008**, *47* (28), 5157−5159.

(6) Rothemund, P. W. K. Folding DNA to Create Nanoscale Shapes and Patterns. *Nature* **2006**, *440* (7082), 297−302.

(7) Sharma, J.; Chhabra, R.; Andersen, C. S.; Gothelf, K. V.; Yan, H.; Liu, Y. Toward Reliable Gold Nanoparticle Patterning On Self-Assembled DNA Nanoscaffold. *J. Am. Chem. Soc.* **2008**, *130* (25), 7820−7821.

(8) Ding, B.; Deng, Z.; Yan, H.; Cabrini, S.; Zuckermann, R. N.; Bokor, J. Gold Nanoparticle Self-Similar Chain Structure Organized by DNA Origami. *J. Am. Chem. Soc.* **2010**, *132* (10), 3248−3249.

(9) Hung, A. M.; Micheel, C. M.; Bozano, L. D.; Osterbur, L. W.; Wallraff, G. M.; Cha, J. N. Large-Area Spatially Ordered Arrays of Gold Nanoparticles Directed by Lithographically Confined DNA Origami. *Nat. Nanotechnol.* **2010**, *5* (2), 121−126.

(10) Pal, S.; Deng, Z.; Ding, B.; Yan, H.; Liu, Y. DNA-Origami-Directed Self-Assembly of Discrete Silver-Nanoparticle Architectures. *Angew. Chem., Int. Ed.* **2010**, *49* (15), 2700−2704.

(11) Endo, M.; Yang, Y.; Emura, T.; Hidaka, K.; Sugiyama, H. Programmed Placement of Gold Nanoparticles onto a Slit-Type DNA Origami Scaffold. *Chem. Commun.* **2011**, *47* (38), 10743−10745.

(12) Kuzyk, A.; Schreiber, R.; Fan, Z.; Pardatscher, G.; Roller, E.-M.; Högele, A.; Simmel, F. C.; Govorov, A. O.; Liedl, T. DNA-Based Self-Assembly of Chiral Plasmonic Nanostructures with Tailored Optical Response. *Nature* **2012**, *483* (7389), 311−314.

(13) Prinz, J.; Schreiber, B.; Olejko, L.; Oertel, J.; Rackwitz, J.; Keller, A.; Bald, I. DNA Origami Substrates for Highly Sensitive Surface-Enhanced Raman Scattering. *J. Phys. Chem. Lett.* **2013**, *4* (23), 4140−4145.

(14) Shen, X.; Song, C.; Wang, J.; Shi, D.; Wang, Z.; Liu, N.; Ding, B. Rolling Up Gold Nanoparticle-Dressed DNA Origami into Three-Dimensional Plasmonic Chiral Nanostructures. *J. Am. Chem. Soc.* **2012**, *134* (1), 146−149.

(15) Acuna, G. P.; Möller, F. M.; Holzmeister, P.; Beater, S.; Lalkens, B.; Tinnefeld, P. Fluorescence Enhancement at Docking Sites of DNA-Directed Self-Assembled Nanoantennas. *Science* **2012**, *338* (6106), 506−510.

(16) Takabayashi, S.; Klein, W. P.; Onodera, C.; Rapp, B.; Flores-Estrada, J.; Lindau, E.; Snowball, L.; Sam, J. T.; Padilla, J. E.; Lee, J.; et al. High Precision and High Yield Fabrication of Dense Nanoparticle Arrays onto DNA Origami at Statistically Independent Binding Sites. *Nanoscale* **2014**, *6* (22), 13928−13938.

(17) Pilo-Pais, M.; Goldberg, S.; Samano, E.; LaBean, T. H.; Finkelstein, G. Connecting the Nanodots: Programmable Nanofabrication of Fused Metal Shapes on DNA Templates. *Nano Lett.* **2011**, *11* (8), 3489−3492.

(18) Schreiber, R.; Do, J.; Roller, E.-M.; Zhang, T.; Schüller, V. J.; Nickels, P. C.; Feldmann, J.; Liedl, T. Hierarchical Assembly of Metal Nanoparticles, Quantum Dots and Organic Dyes Using DNA Origami Scaffolds. *Nat. Nanotechnol.* **2014**, *9* (1), 74−78.

(19) Klein, W. P.; Schmidt, C. N.; Rapp, B.; Takabayashi, S.; Knowlton, W. B.; Lee, J.; Yurke, B.; Hughes, W. L.; Graugnard, E.;

DOI: 10.1021/acs.langmuir.5b02569
Langmuir 2015, 31, 12823−12829

Kuang, W. Multiscaffold DNA Origami Nanoparticle Waveguides. *Nano Lett.* **2013**, *13* (8), 3850−3856.
(20) Gates, E. P.; Jensen, J. K.; Harb, J. N.; Woolley, A. T. Optimizing Gold Nanoparticle Seeding Density on DNA Origami. *RSC Adv.* **2015**, *5* (11), 8134−8141.
(21) Gerdon, A. E.; Oh, S. S.; Hsieh, K.; Ke, Y.; Yan, H.; Soh, H. T. Controlled Delivery of DNA Origami on Patterned Surfaces. *Small* **2009**, *5* (17), 1942−1946.
(22) Kershner, R. J.; Bozano, L. D.; Micheel, C. M.; Hung, A. M.; Fornof, A. R.; Cha, J. N.; Rettner, C. T.; Bersani, M.; Frommer, J.; Rothemund, P. W. K.; et al. Placement and Orientation of Individual DNA Shapes on Lithographically Patterned Surfaces. *Nat. Nanotechnol.* **2009**, *4* (9), 557−561.
(23) Ding, B.; Wu, H.; Xu, W.; Zhao, Z.; Liu, Y.; Yu, H.; Yan, H. Interconnecting Gold Islands with DNA Origami Nanotubes. *Nano Lett.* **2010**, *10* (12), 5065−5069.
(24) Pearson, A. C.; Pound, E.; Woolley, A. T.; Linford, M. R.; Harb, J. N.; Davis, R. C. Chemical Alignment of DNA Origami to Block Copolymer Patterned Arrays of 5 Nm Gold Nanoparticles. *Nano Lett.* **2011**, *11* (5), 1981−1987.
(25) Yun, J. M.; Kim, K. N.; Kim, J. Y.; Shin, D. O.; Lee, W. J.; Lee, S. H.; Lieberman, M.; Kim, S. O. DNA Origami Nanopatterning on Chemically Modified Graphene. *Angew. Chem., Int. Ed.* **2012**, *51* (4), 912−915.
(26) Gao, B.; Sarveswaran, K.; Bernstein, G. H.; Lieberman, M. Guided Deposition of Individual DNA Nanostructures on Silicon Substrates. *Langmuir* **2010**, *26* (15), 12680−12683.
(27) Kuzyk, A.; Yurke, B.; Toppari, J. J.; Linko, V.; Törmä, P. Dielectrophoretic Trapping of DNA Origami. *Small* **2008**, *4* (4), 447−450.
(28) Teshome, B.; Facsko, S.; Keller, A. Topography-Controlled Alignment of DNA Origami Nanotubes on Nanopatterned Surfaces. *Nanoscale* **2014**, *6* (3), 1790−1796.
(29) Gopinath, A.; Rothemund, P. W. K. Optimized Assembly and Covalent Coupling of Single-Molecule DNA Origami Nanoarrays. *ACS Nano* **2014**, *8* (12), 12030−12040.
(30) Pearson, A. C.; Liu, J.; Pound, E.; Uprety, B.; Woolley, A. T.; Davis, R. C.; Harb, J. N. DNA Origami Metallized Site Specifically to Form Electrically Conductive Nanowires. *J. Phys. Chem. B* **2012**, *116* (35), 10551−10560.
(31) Li, Z.; Wang, L.; Yan, H.; Liu, Y. Effect of DNA Hairpin Loops on the Twist of Planar DNA Origami Tiles. *Langmuir* **2012**, *28* (4), 1959−1965.
(32) Sharma, J.; Chhabra, R.; Cheng, A.; Brownell, J.; Liu, Y.; Yan, H. Control of Self-Assembly of DNA Tubules Through Integration of Gold Nanoparticles. *Science* **2009**, *323* (5910), 112−116.
(33) Shaw, A.; Benson, E.; Högberg, B. Purification of Functionalized DNA Origami Nanostructures. *ACS Nano* **2015**, *9* (5), 4968−4975.
(34) Bensimon, D.; Simon, A. J.; Croquette, V.; Bensimon, A. Stretching DNA with a Receding Meniscus: Experiments and Models. *Phys. Rev. Lett.* **1995**, *74* (23), 4754−4757.
(35) Bui, H.; Onodera, C.; Kidwell, C.; Tan, Y.; Graugnard, E.; Kuang, W.; Lee, J.; Knowlton, W. B.; Yurke, B.; Hughes, W. L. Programmable Periodicity of Quantum Dot Arrays with DNA Origami Nanotubes. *Nano Lett.* **2010**, *10* (9), 3367−3372.
(36) Keller, A.; Facsko, S.; Möller, W. Minimization of Topological Defects in Ion-Induced Ripple Patterns on Silicon. *New J. Phys.* **2008**, *10* (6), 063004.
(37) Nečas, D.; Klapetek, P. Gwyddion: An Open-Source Software for SPM Data Analysis. *Open Phys.* **2012**, *10* (1), 181−188.
(38) Aghebat Rafat, A.; Pirzer, T.; Scheible, M. B.; Kostina, A.; Simmel, F. C. Surface-Assisted Large-Scale Ordering of DNA Origami Tiles. *Angew. Chem., Int. Ed.* **2014**, *53* (29), 7665−7668.
(39) Gotschy, W.; Vonmetz, K.; Leitner, A.; Aussenegg, F. R. Optical Dichroism of Lithographically Designed Silver Nanoparticle Films. *Opt. Lett.* **1996**, *21* (15), 1099−1101.
(40) Park, J. H.; Lee, D. Y.; Seung, W.; Sun, Q.; Kim, S.-W.; Cho, J. H. Metallic Grid Electrode Fabricated via Flow Coating for High-Performance Flexible Piezoelectric Nanogenerators. *J. Phys. Chem. C* **2015**, *119* (14), 7802−7808.

DOI: 10.1021/acs.langmuir.5b02569
Langmuir 2015, 31, 12823−12829

Nanometer scale elemental analysis in the helium ion microscope using time of flight spectrometry

N. Klingner[a,b,*], R. Heller[a], G. Hlawacek[a], J. von Borany[a], J. Notte[c], J. Huang[c], S. Facsko[a]

[a] *Helmholtz–Zentrum Dresden–Rossendorf e.V., Bautzner Landstr. 400, 01328 Dresden, Germany*
[b] *Technical University Dresden, 01062 Dresden, Germany*
[c] *Ion Microscopy Innovation Center at Carl Zeiss Microscopy LLC, One Corporation Way, Peabody, Massachusetts 01960 USA*

Abstract

Time of flight backscattering spectrometry (ToF–BS) was successfully implemented in a helium ion microscope (HIM). Its integration introduces the ability to perform laterally resolved elemental analysis as well as elemental depth profiling on the nm scale. A lateral resolution of ≤ 54 nm and a time resolution of $\Delta t \leq 17$ ns ($\Delta t/t \leq 5.4\%$) are achieved. By using the energy of the backscattered particles for contrast generation, we introduce a new imaging method to the HIM allowing direct elemental mapping as well as local spectrometry. In addition laterally resolved time of flight secondary ion mass spectrometry (ToF–SIMS) can be performed with the same setup. Time of flight is implemented by pulsing the primary ion beam. This is achieved in a cost effective and minimal invasive way that does not influence the high resolution capabilities of the microscope when operating in standard secondary electron (SE) imaging mode. This technique can thus be easily adapted to existing devices. The particular implementation of ToF–BS and ToF–SIMS techniques are described, results are presented and advantages, difficulties and limitations of this new techniques are discussed.

Keywords: helium ion microscope, time of flight, elemental analysis, backscattering spectrometry, neutral impact–collision ion scattering spectrometry, secondary ion mass spectrometry

1. Introduction

In the recent past helium ion microscopy [1] has become a mature technique that is best known for its high resolution imaging capabilities. The latest version of these devices, the Zeiss helium ion microscope (model *Orion NanoFab*) (used in this work) is able to operate with He as well as with Ne ions and provides high resolution nano–engineering capabilities [2–4], that so far are unmatched by any other technique. Using neon in the gas field ion source (GFIS) nano–structuring with 2 nm lateral resolution is possible without any metal (Ga) contamination [5, 6]. Although exceptional nano machining and imaging results on insulating and biological samples have been achieved, so far no analytical elemental information can be obtained in the HIM.

Several attempts have been made in the past to obtain analytical information utilizing the nano–sized ion beam available in GFIS microscopes. Early attempts to perform backscattering spectrometry (BS) in a HIM utilized a cooled, windowless silicon drift detector [7]. However, Si particle detectors provide an energy resolution with a low $\Delta E/E$ ratio of just 1:10 or worse. The so obtained BS spectra have been useful only in a limited number of specialized cases. Further, from this attempt it became clear that monolayer sensitivity should in principle be possible [8]. Analyzing the energy distribution of the emitted secondary electrons for elemental analysis has not matured so far [9]. Here, matrix effects and non–linearities in the SE–yield hinder the quantification of the obtained SE energy spectra [10, 11]. Recently impressive progress has been made in the development of a dedicated SIMS add–on for the HIM [12, 13]. The approach followed by Wirtz *et al.* [14] will allow high resolution SIMS spectra and mass filtered images with sub-20 nm lateral resolution.

For the elemental analysis by BS several different approaches could be used. For conventional primary ion energies in the range from 100 keV to some MeV various approaches of backscattering energy measurement have been established in the past. Semiconductor detectors are most commonly used and can deliver an energy resolution down to 5.1 keV for 2.25 MeV protons [15] using an in–vacuum preamplifier. Using additional detector cooling an energy resolution of 1.8 keV was reported for 600 keV deuterons [16] and 7 keV for 3.2 MeV He [17]. For low energies such as the ones used in HIM (typically 10 keV to 40 keV) energy resolution of 4.5 keV for 25 keV He particles have been reported. These results have been achieved by using a Peltier cooled silicon drift detector [7, 8]. Other approaches make use of magnetic [18] or electrostatic energy analyzers which have an excellent energy resolution down to $\Delta E/E \leq 0.001$ but are only sensitive to charged particles [19, 20] and acquire spectra in a sequential manner.

The fraction of charged, backscattered projectiles for energies below 10 keV decreases rapidly with increasing depth and is below one percent for scattering from depths as low as one nm [21–24]. For energies above 30 keV the charge fraction

*Corresponding author
Email address: n.klingner@hzdr.de (N. Klingner)

stays below ten percent [25].

Consequently, for backscattered particle detectors that are sensitive only to charged particles, the overall usefulness is reduced due to the increased sample damage and longer analysis time. The attempt of performing BS in a HIM is connected to a very small beam size and low primary ion energies. It thus is clear that in order to prevent sample damage (by sputtering and/or bubble formation [26–29]) backscattered particle detection has to be sensitive to both backscattered ions as well as neutrals.

Micro calorimeters would provide the necessary energy resolution [30] and are sensitive to ions and neutrals but their implementation into the microscope and the decoupling from the heat reservoir of the chamber would require a considerable amount of investigation and engineering work.

The most convenient approach is the application of ToF spectrometry. Performing ToF spectrometry by triggering the start signal from secondary electrons from the sample surface are currently under development for classical Ga focused ion beams [31] as well HIM [32, 33]. However, the high number of emitted SEs compared to the rather low cross sections for backscattering lead to a very low coincidence rate and subsequently a poor signal to noise ratio and therefore long measuring times.

Different to previous approaches, here time of flight spectrometry is enabled by pulsing the primary ion beam. We present first analytical results obtained with a combined time of flight backscattering spectrometry and secondary ion mass spectrometry setup. Both techniques utilize the same cost efficient approach, which requires minimal modifications of the system to ensure that the high resolution imaging capabilities are maintained when no analytical information is required. Switching between ToF–BS and standard SE imaging can be performed electronically and requires no mechanical adjustments on the instrument hardware.

2. Experimental

The helium ion microscope delivers primary ion energies from 5 keV to 35 keV, typical ion currents of a few pA and a beam focus below 0.5 nm. Higher currents of up to 150 pA are possible, however only with a larger beam spot and consequently a lower lateral resolution. A scheme showing the major components of the device is presented in fig. 1.

The start signal for the ToF measurement is created by pulsing the primary ion beam. To retain the excellent imaging capabilities of the microscope no changes have been made to the ion beam column. A newly designed fast pulsing electronics has been added to the column–mounted electronics of the beam blanking unit ((7) in fig. 1). The new electronics generates fast voltage pulses on both blanking plates that unblank the ion beam from the Faraday cup ((8) in fig. 1) for a few nanoseconds towards the sample. It is triggered by a standard TTL pulse from a pulse generator with a typical repetition rate of up to 500 kHz. An oscillograph of the voltages on both blanking plates is shown in fig. 2(a). A rise/fall time of 8 ns equally for both blanking plates was achieved.

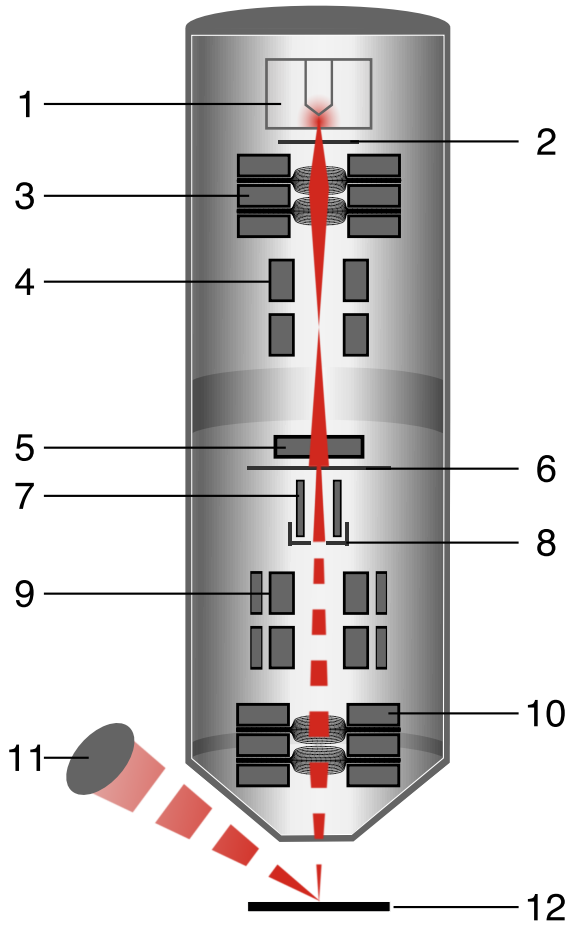

Figure 1: Simplified scheme of the HIM (not to scale): 1 Source and gas chamber, 2 Extractor, 3 Einzel lens I, 4 Quadrupole, 5 Column isolation valve, 6 Aperture, 7 Blanking unit, 8 Faraday cup, 9 Octopole, 10 Einzel lens II, 11 Micro channel plate, 12 Sample. The beam path is indicated in red.

The stop signal for our ToF measurements is obtained by detecting the backscattered particles on a micro channel plate (MCP) referred to as the stop detector in the following ((11) in fig. 1). It is a chevron stack MCP (model AF2225-A41D, type F1217-01 Hamamatsu Photonics) operated at an amplification voltage of 1800 V. The stop detector is mounted under a backscattering angle of 126° to the primary ion beam and in a distance of 358 mm to the target surface with a solid angle of 10.8 msr. For an increased relative time resolution a second MCP is mounted in a distance of 1023 mm which results in a smaller solid angle of 1.3 msr. The stop signal is amplified by a pre–amplifier (model TA2000B–2, FAST ComTec), the edge detection is done by a constant fraction discriminator (model 2128, FAST ComTec) and the time of flight is measured with a time to amplitude converter (model 2145, Canberra) and digitised by an analog to digital converter (model 7072T, FAST ComTec). Standard spectroscopic equipment (pulse height analysis via a multi channel analyzer) finally reveals the ToF spectrum.

The performance of the ToF setup has been evaluated by direct measurement of the time profile of the pulsed ion beam

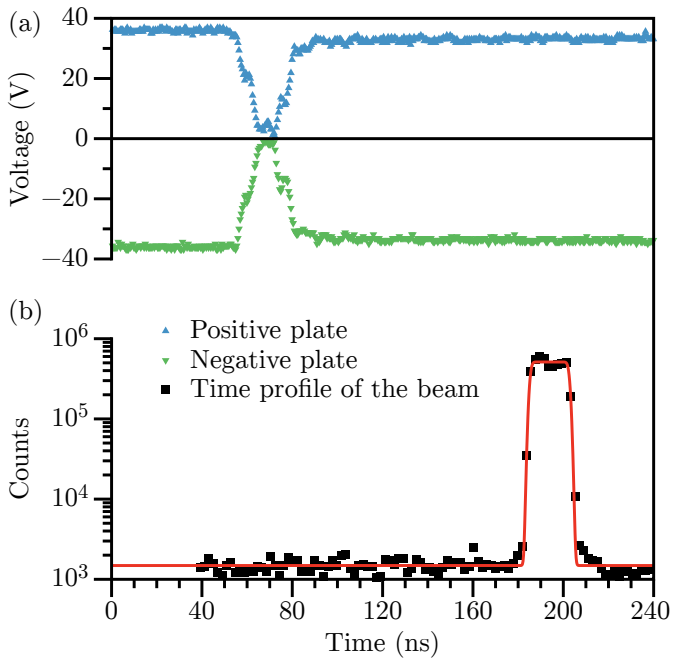

Figure 2: Voltage pulses on both blanking plates (blue and blue triangles (a)) and time profile of a pulsed 30 keV He^+ ion beam (black squares in (b)), both triggered by a TTL pulse at 0 ns. The beam pulse fits a box profile with a FWHM of 17 ns and a rise/fall time of 1.7 ns (red line). It starts at 120 ns after unblanking the ion beam which approximately corresponds to the flight time from the blanker to the sample.

using a channeltron mounted on the sample stage. The time profile of a 30 keV pulsed He ion beam has been integrated over 2×10^7 pulses and is shown in fig. 2(b). It can be described by a double error function with a width of 17 ns and a rise/fall time of 1.7 ns.

3. Results and discussion

3.1. Time of flight backscattering spectrometry

A typical ToF He backscattering spectrum of a 2 nm HfO_2 layer on top of Si is shown in fig. 3. For this measurement the pulsed beam was continuously scanned across a sample area of 200 μm^2. The peak at 320 ns corresponds to backscattering from Hf which is separated from the signal of the silicon bulk material starting at 380 ns. Since the HfO_2 layer is very thin, its full width half maximum (FWHM) corresponds to the time resolution of the ToF setup. The measured $\Delta t = 17.3$ ns equals a relative time resolution of $\Delta t/t \leq 5.4\,\%$. This value fits to the ratio between the length of the blanking plates and the distance between sample surface and stop detector (5.8%). Obviously, increased energy straggling inside the sample with increasing depths [34] has to be taken into account and conventional single collision analysis can be assumed only for near-surface scattering. ToF spectrometers also allow even better energy resolution by increasing the flight path at cost of decreased solid angle and counting statistics. Using the same setup but with a flight path of 1023 mm and a flight time of 900 ns, a relative time resolution of $\leq 2.7\%$ has been achieved.

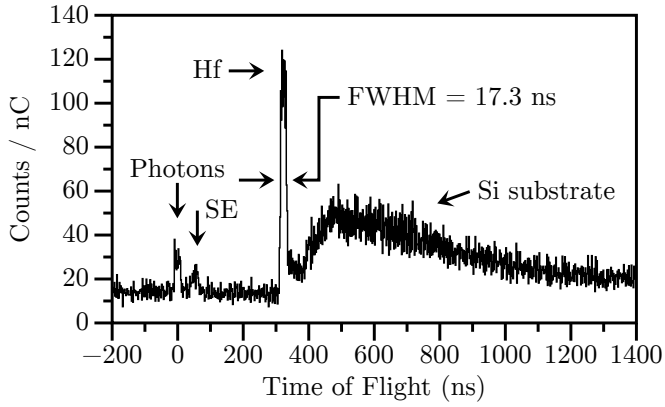

Figure 3: Time of flight spectrum of 30 keV He^+ backscattered from a 2 nm HfO_2 layer on top of Si measured with 17.3 ns time resolution. The time scale of the spectra was calibrated by helium induced photons. The total charge collected for this spectrum was 1.9 nC.

The layer structure of a sample and the elemental composition of the particular layers can be determined from the measured spectra by simulation and comparison of the simulation result to the data in an interactive way. Conventional backscattering spectrometry is typically performed with primary energies above 1 MeV and well known as Rutherford backscattering spectrometry (RBS). Analytical simulation software packages like RUMP [35], WINDF [36] or SIMNRA [37] are commonly used and known to deliver quite accurate results. All of them have in common that they assume a single or at most two main collision (besides simple models to correct the effect of multiple scattering) leading to a change of the direction and the energy of the primary particle. However, in the low energy range below 100 keV the majority of backscattered particles are suffering multiple large angle collisions with the target atoms. Thus these programs fail to recover the measured spectra. In contrast Monte Carlo simulation software like SRIM [38], TRIDYN [39], CORTEO [40] or TRBS [41] use a binary collision approximation and deliver results taking into account multiple scattering.

The comparison of spectra from ToF measurements with simulated spectra requires a conversion of the time of flight into an energy or vice versa. A precise knowledge of the offset of the time axis is therefore essential. Since the start signal is triggered by blanking the beam and the stop signal by the backscattered particle hitting the stop MCP, the measured time of flight has to be reduced by the electronic delay and the flight time of the primary ions from the blanker to the sample surface. The latter one depends on the ions mass, its energy, and the distance from the blanking plates to the sample and can be embedded in the analysis routine. However, the first part is more difficult. Therefore the total time offset is calibrated by making use of photons emitted during the interaction of the primary beam with the sample. The lifetime of the excited states of ≤ 10 ns [42, 43] and the ToF below 2 ns make them suitable for the calibration. Although the production rate for photons in this ion energy range is rather small it is sufficient to collect a usable signal in reasonable time (minutes).

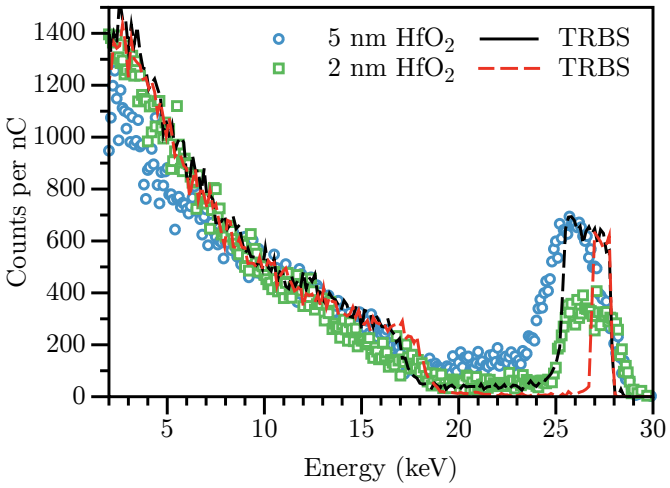

Figure 4: ToF spectra of 5 nm and 2 nm HfO_2 layer on top of Si converted into energy space (dots and squares) and corresponding TRBS [41] simulations (black and red lines). The collected charge has been adapted to fit the Si bulk signal to the TRBS simulation.

The converted spectrum of the ToF measurement presented in fig. 3 (30 keV He on 2 nm HfO_2 layer on Si) is plotted in fig. 4 together with a spectrum of a 5 nm HfO_2 layer on Si. The dots and squares present measured spectra while the black and red lines are results from Monte Carlo simulations using TRBS. The energy resolution of our ToF setup translates to a sufficient depth resolution to clearly distinguish between the different thicknesses of the HfO_2 layers. In each simulation the trajectories of 5×10^7 He ions were evaluated. Simulated particles backscattered towards the detector were recorded and sorted into a pulse height spectrum according to their energy. The resulting spectrum was scaled to the solid angle and plotted as counts per nC.

The collected charge in both measurements has been adapted to fit the Si bulk signal to the TRBS simulation. The charge adaption had to be done because the charge measurement in the HIM is designed to measure DC ion currents instead of a pulsed beam. For both measurements two different scaling factors had to be applied since they were recorded with different primary ion beam currents. For both samples the gap between Hf-peak and Si substrate reveals a non-zero offset that is not predicted by the simulations. A similar observation can be found for focused ion beam based ToF–BS [31, 44]. The origin of this effect stays unclear so far. The larger height and the smaller width of the simulated peaks originate from neglecting any detector resolution which is present in the experimental data only.

3.2. Elemental mapping with backscattering spectrometry

To obtain laterally resolved element maps we made use of a self-made micro controller based external scan electronic. This external scan controller provides analog signals to the input of the microscope steering the scanning of the beam. It further records the time of flight for each event from the analog to digital converter together with the current scan position. These events are stored in a list mode file for further evaluation. Thus one can post-select particular regions of interest within the scan field and extract local energy spectra. Scan parameters like field of view, number of pixels or dwell time (pixel time) are configurable in the data acquisition software.

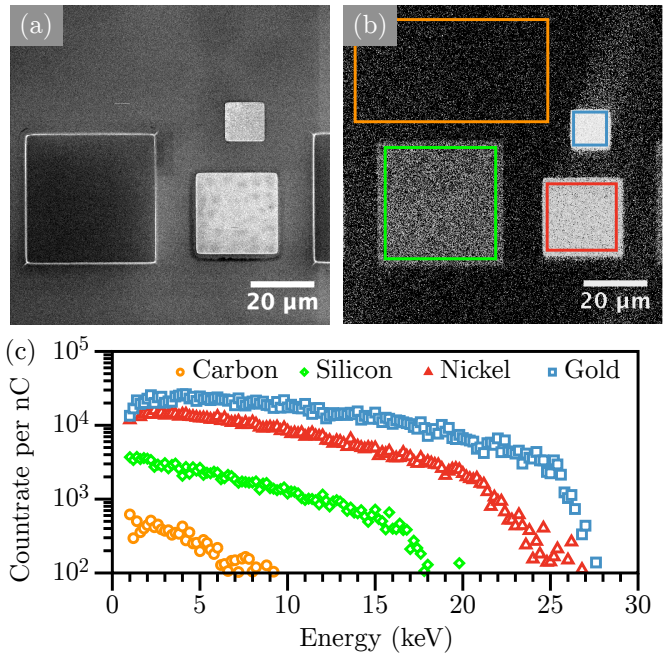

Figure 5: Images of a Au/Ni/Si patterned test sample (as described in the text) acquired in SE mode (a) and in ToF–BS mode (b). (c) shows energy spectra of backscattered He within different regions of interest in (b). The color of each spectrum in (c) corresponds to the colors of the rectangles marking the corresponding region of interest in (b).

To test the imaging capabilities of the HIM in ToF–BS mode we used a glassy carbon sample coated with rectangular patches of Si, Ni and Au. The patches have different dimensions of 40 µm × 40 µm × 300 nm (Si), 25 µm × 25 µm × 110 nm (Ni) and 12 µm × 12 µm × 85 nm (Au), respectively. An image of the test sample in standard SE mode is shown in fig. 5(a) and the ToF–BS image from the same surface region is presented in fig. 5(b). For this image only the highest backscattering energy in each pixel is taken for contrast generation. This leads to an enhanced elemental contrast. In fig. 5(c), the BS spectra obtained from different regions within the image presented in fig. 5(b) are shown. This allows local quantitative element analysis which is currently not possible in standard SE imaging.

Partially blanked ions lead to non axial trajectories and a spatial offset. The flight time of a 30 keV He ion through the blanking plates is approximately 17 ns. The ion will pass the blanker in an undisturbed manner if the plates are grounded during its transition. However, if the blanker changes state during the transition of the ion, it will be deflected from the aligned path through the column. This leads to a reduced lateral resolution in pulsed beam operation. The lateral resolution parallel to the deflection direction is most influenced by this effect.

The edge resolution in pulsed mode was evaluated using a Ni patch on our test sample. The results are shown in fig. 6. Im-

ages of the Ni patch without pulsing the ion beam in SE mode (fig. 6(a)) and in ToF–BS mode (fig. 6(b)) as well as the corresponding line profiles across the edges (fig. 6(c)) are presented. Line profiles of several neighboring (vertical) lines were averaged (indicated by the rectangles in fig. 6(a,b)) leading to a better signal to noise ratio. The blanking direction in this measurement was 52° with respect to the Ni edge. The edge resolution (80%-20%) is 10.9 nm in SE mode without pulsing the beam and 53.7 nm in ToF–BS mode using beam pulses with a length of 55 ns.

The reduced lateral resolution in ToF–BS mode is attributed to the partial blanking of the beam as discussed above. The larger sampling volume of the backscattered particles and the sample drift due to longer acquisition time contribute further to the reduced lateral resolution.

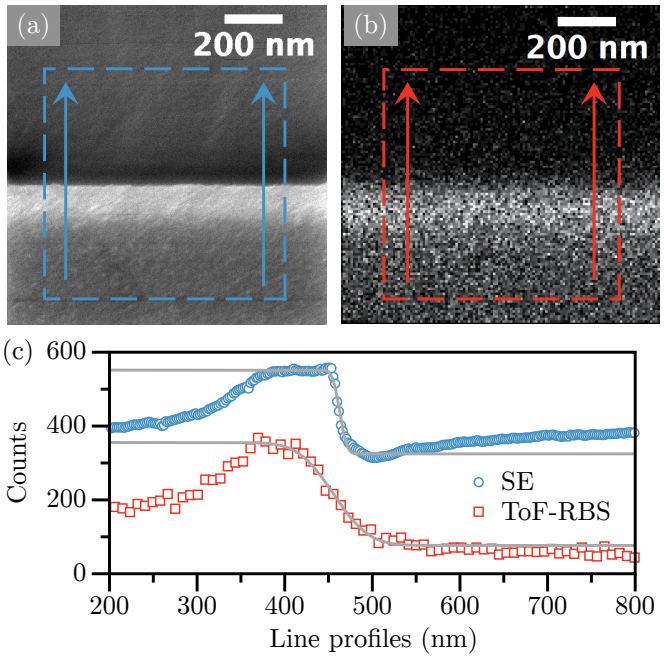

Figure 6: SE image without pulsing the ion beam (a) and ToF–BS image (b) of a Ni patch on the test sample described in the text and derived line profiles of the Ni edge (c). Line profiles are measured and averaged across the Ni edge according to the rectangles plotted in (a) and (b) and error functions fitted at the edges. The edge resolutions (80%-20%) was determined to 10.9 nm in SE mode and 53.7 nm in ToF–BS mode using 55 ns beam pulses.

It should be mentioned that the pulse length influences lateral resolution, energy resolution and signal to noise ratio simultaneously. By adjusting pulse length and duty cycle one can vary between optimum lateral and highest energy resolution. Both have to be adapted according to the particular demands of the measurement task.

3.3. Time of flight secondary ion mass spectrometry

In addition to the possibility of the measurement of ToF–BS spectra our approach of pulsing the primary ion beam allows time of flight secondary ion mass spectrometry (ToF–SIMS). For this purpose the sputtered ions (with energies of few to few tens eV [45]) have to be accelerated to higher kinetic energies and guided towards the MCP. The time of flight directly scales with the secondary ion mass in this mode of operation.

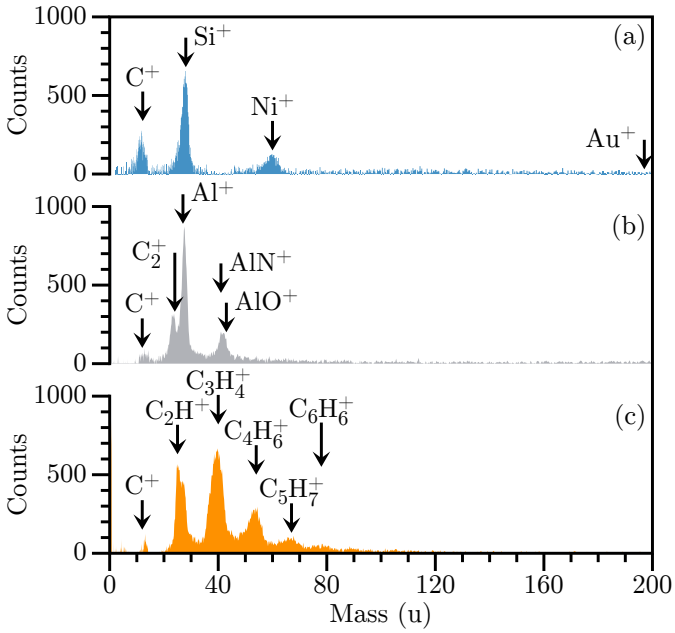

Figure 7: ToF-SIMS spectra of the Au/Ni/Si/C test sample describe in the text (a), an aluminium sample (b) and copper tape (c) measured in the HIM with 25 keV Ne ions and 250 ns pulse length.

In our experiments we applied an acceleration voltage of 500 V leading to an additional energy of 500 eV for single charged and 1000 eV for doubly charged particles, respectively (both can be identified in the mass spectra). To minimize the time spread caused by different starting energies, acceleration has to be applied as close as possible to the surface. Therefore we biased the sample holder to 500 V and mounted a grounded TEM grid on top of the sample in a distance of less than one millimeter. The sample was additionally tilted to face towards the MCP. Therefore the sputtered ions can pass through the chamber to the MCP without the need of a flight tube. Due to the sample bias, the primary ion beam is decelerated from 30 keV to 29.5 keV before reaching the sample. This setup enables SIMS measurements with moderate efforts, but with inferior ion collection efficiency compared to dedicated SIMS machines were ions are extracted by more complex extraction optics and guided towards the detector. Due to the finite mesh size of the TEM grid inhomogeneities of the electric field may occur leading to a broadening of the beam focus. It has been shown by Dowsett *et al.* [45] that an advanced extraction system would improve the efficiency of the SIMS setup in the HIM while keeping the lateral resolution below 10 nm. Since the majority of emitted secondary electrons have energies less than 500 eV [9, 10, 46] standard SE imaging is not available during ToF–SIMS measurements. Because of higher sputter yields the use of neon is preferred for SIMS experiments.

The ToF–SIMS spectrum of the test sample described above is shown in fig. 7(a). Mass peaks from carbon, silicon and nickel are found well separated from each other. The gold peak cannot be distinguished from background noise because

the secondary Au^+ yield is several orders of magnitudes smaller compared to carbon, silicon and nickel [12]. In fig. 7(b,c) further ToF–SIMS spectra of a pure aluminum sample and a piece of copper tape are presented. For the latter the ToF–SIMS spectrum actually reveals the constituents of the organic glue on top of the copper which is much thicker than the origin of the sputtered particles.

Since the flight times of the accelerated sputtered ions ($E = 500$ eV) are higher than those of backscattered He in ToF–BS mode ($E \leq 30$ keV) ToF–SIMS spectra can be acquired by using larger puls lengths. We used 250 ns pulses corresponding to $t/\Delta t \approx 40$ and measured a FWHM mass resolving power of $M/\Delta M \approx 12$ (Al peak). The initial energy distribution [45] of sputtered particles leads to variations in the time of flight from the sample surface to the acceleration grid. This effect can be reduced by applying higher acceleration voltages. However, compared to the short pulses for ToF–BS measurements, higher pulse lengths lead to a better lateral resolution (see text above). The need for ion extraction by biasing the sample also contributes to a lateral spread (see also [45]).

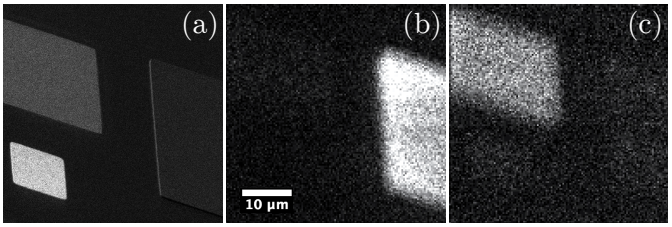

Figure 8: Images of the carbon test sample described in the text acquired in SE mode (a) and in ToF–SIMS mode (b,c) using 25 keV neon ion beam with 250 ns pulses. Different mass filters were applied for generating maps of silicon (b) and nickel (c) distribution out of the common list mode file.

The SE image of the carbon test sample is shown in fig. 8(a) and ToF–SIMS images obtained from the same location are presented in fig. 8(b,c). For generating the particular ToF–SIMS images from the corresponding list mode file different mass (flight time) filters were applied. In fig. 8(b) only silicon is shown whereas in fig. 8(c) the nickel counts are presented. Since in ToF–SIMS mode the sample has to face towards the MCP detector (see text above) the rectangular patches appear as parallelogram shapes in the images. Although mass filters are applied in fig. 8(b,c) one can identify faintly visible structures at the position of the remaining patches. These originate from neutrals (mainly backscattered neon) which could be suppressed by a reflectron flight tube in a future design. However, characterization and optimization of the ToF–SIMS mode with respect to mass and lateral resolution as well as signal–to–noise ratio are subject of future investigations. As is evident from the presented data ToF–SIMS in the HIM is perfectly capable of delivering an excellent elemental contrast for imaging purposes. However, quantification of elements in mixed layers can not be done from pure SIMS measurements without comparison to standards. This drawback of SIMS is partly overcome here as our setup is capable to also measure ToF–BS spectra. These deliver the needed quantitative information on the layer composition. Thus ToF–BS and ToF–SIMS performed in–situ complement each other and therefore deliver a maximum of compositional information on the sample.

4. Summary

We demonstrated that time of flight backscattering spectrometry as well as secondary ion mass spectrometry can be performed in a helium ion microscope to obtain information on the elemental composition of a sample. This information is not accessible in standard SE imaging mode. Data acquisition in list mode enables post–processing of measured data to obtain BS spectra on specific regions of interest and elemental mapping at the nanometer scale. A lateral resolution of 54 nm for ToF–BS imaging was demonstrated. Spatial resolved BS was so far only possible down to 300 nm^2 [47, 48] using ion micro probe experiments requiring big (MeV) ion accelerators. Our experimental approach requires a minimum of changes to the existing HIM hardware and thus may be easily retrofitted on existing devices significantly enhancing their capabilities. The setup additionally allows ToF–SIMS measurements in the HIM delivering excellent elemental contrast. In summary we present a minimal invasive and cost effective way to extract a maximum of information from the sample in a correlative approach. The ability to obtain SE, ToF–BS and TOF–SIMS images in–situ, enables the user to correlate these data and in this way obtain elemental and topographical information at the nanometer scale.

Acknowledgement

Financial support from the Bundesministerium für Wirtschaft und Energie (BMWi) (Grant 03ET7016) is acknowledged. The authors thank R. Aniol (HZDR) for manufacturing of the mechanical parts for the ToF setup and P. Bauer (JKU Llinz) for providing the TRBS simulations.

References

[1] G. Hlawacek, V. Veligura, R. van Gastel, B. Poelsema, Helium Ion Microscopy, J. Vac. Sci. Technol., B: Microelectron. Nanometer Struct. 32 (2) (2013) 1–16. arXiv:1311.1711, doi:10.1116/1.4863676. URL http://scitation.aip.org/content/avs/journal/jvstb/32/2/10.1116/1.4863676http://arxiv.org/abs/1311.1711

[2] P. F. A. Alkemade, E. van Veldhoven, Deposition, Milling, and Etching with a Focused Helium Ion Beam, in: M. Stepanova, S. Dew (Eds.), Nanofabrication: Techniques and principles, Springer, Vienna, 2012, pp. 275—-300.

[3] A. I. Kuznetsov, A. E. Miroshnichenko, Y. Hsing Fu, V. Viswanathan, M. Rahmani, V. Valuckas, Z. Ying Pan, Y. Kivshar, D. S. Pickard, B. Luk'yanchuk, Split-ball resonator as a three-dimensional analogue of planar split-rings., Nat. Commun. 5 (2014) 3104. doi:10.1038/ncomms4104. URL http://www.ncbi.nlm.nih.gov/pubmed/24430506

[4] D. C. Bell, Contrast mechanisms and image formation in helium ion microscopy., Microsc. Microanal. 15 (2) (2009) 147–53. doi:10.1017/S1431927609090138. URL http://www.ncbi.nlm.nih.gov/pubmed/19284896

[5] S. A. Cybart, P. X. T. Yen, E. Y. Cho, J. U. Huh, V. N. Glyantsev, C. S. Yung, B. Moeckly, J. W. Beeman, R. C. Dynes, Comparison of YBaCuO Films Irradiated With Helium and Neon Ions for the Fabrication of Josephson Devices, IEEE Trans. Appl. Supercond. 24 (4) (2014) 1100105.

[6] J. A. Notte, Charged Particle Microscopy: Why Mass Matters, Micros. Today 20 (05) (2012) 16–22. doi:10.1017/S1551929512000715.

[7] S. Sijbrandij, B. Thompson, J. Notte, B. W. Ward, N. P. Economou, Elemental analysis with the helium ion microscope, J. Vac. Sci. Technol., B: Microelectron. Nanometer Struct. 26 (6) (2008) 2103. doi:10.1116/1.2993262.

[8] S. Sijbrandij, J. Notte, L. Scipioni, C. Huynh, C. Sanford, Analysis and metrology with a focused helium ion beam, J. Vac. Sci. Technol., B: Microelectron. Nanometer Struct. 28 (1) (2010) 73. doi:10.1116/1.3271254.

[9] Y. Petrov, O. Vyvenko, Secondary electron emission spectra and energy selective imaging in helium ion microscope, in: Proc. SPIE, Vol. 8036, 2011, pp. 80360O–80360O–10. doi:10.1117/12.886347.
URL http://dx.doi.org/10.1117/12.886347

[10] R. Ramachandra, B. Griffin, D. Joy, A model of secondary electron imaging in the helium ion scanning microscope., Ultramicroscopy 109 (6) (2009) 748–57. doi:10.1016/j.ultramic.2009.01.013.
URL http://www.ncbi.nlm.nih.gov/pubmed/19269097

[11] D. C. Joy, B. J. Griffin, Is microanalysis possible in the helium ion microscope?, Microsc. Microanal. 17 (4) (2011) 643–649. doi:10.1017/S1431927611000596.

[12] L. Pillatsch, N. Vanhove, D. Dowsett, S. Sijbrandij, J. Notte, T. Wirtz, Study and optimisation of SIMS performed with He+ and Ne+ bombardment, Appl. Surf. Sci. 282 (2013) 908–913. doi:10.1016/j.apsusc.2013.06.088.

[13] T. Wirtz, N. Vanhove, L. Pillatsch, D. Dowsett, S. Sijbrandij, J. Notte, Towards secondary ion mass spectrometry on the helium ion microscope: An experimental and simulation based feasibility study with He+ and Ne+ bombardment, Appl. Phys. Lett. 101 (4) (2012) 041601. doi:10.1063/1.4739240.

[14] T. Wirtz, P. Philipp, J.-N. Audinot, D. Dowsett, S. Eswara, High-resolution high-sensitivity elemental imaging by secondary ion mass spectrometry: from traditional 2D and 3D imaging to correlative microscopy, Nanotechnology 26 (43) (2015) 434001. doi:10.1088/0957-4484/26/43/434001.
URL http://stacks.iop.org/0957-4484/26/i=43/a=434001?key=crossref.82da906b523a4ee9f8c72f5f71ffdb3d

[15] N. Klingner, J. Vogt, D. Spemann, Optimizing the Rutherford Backscattering Spectrometry setup in a nuclear microprobe, Nucl. Instrum. Methods Phys. Res., Sect. B 306 (2013) 44–48. doi:10.1016/j.nimb.2012.12.062.
URL http://linkinghub.elsevier.com/retrieve/pii/S0168583X13000438

[16] D. Primetzhofer, P. Bauer, Trace element quantification in high-resolution Rutherford backscattering spectrometry, Nucl. Instrum. Methods Phys. Res., Sect. B 269 (11) (2011) 1284–1287. doi:10.1016/j.nimb.2010.11.028.
URL http://linkinghub.elsevier.com/retrieve/pii/S0168583X10008530

[17] E. Steinbauer, G. Bortels, P. Bauer, J. P. Biersack, P. Burger, I. Ahmad, A survey of the physical processes which determine the response function of silicon detectors to alpha particles, Nucl. Instrum. Methods Phys. Res., Sect. B 339 (1-2) (1994) 102–108.
URL http://www.sciencedirect.com/science/article/pii/0168900294917876

[18] K. Kimura, S. Joumori, Y. Oota, K. Nakajima, M. Suzuki, High-resolution RBS: A powerful tool for atomic level characterization, Nucl. Instrum. Methods Phys. Res., Sect. B 219-220 (1-4) (2004) 351–357. doi:10.1016/j.nimb.2004.01.081.
URL http://linkinghub.elsevier.com/retrieve/pii/S0168583X04001090

[19] H. Ter Veen, T. Kim, I. Wachs, H. Brongersma, Applications of high sensitivity-low energy ion scattering (hs-leis) in heterogeneous catalysis, Catal. Today 140 (3) (2009) 197–201. doi:10.1016/j.cattod.2008.10.012.

[20] H. H. Brongersma, T. Grehl, P. A. van Hal, N. C. Kuijpers, S. G. Mathijssen, E. R. Schofield, R. A. Smith, H. R. ter Veen, High-sensitivity and high-resolution low-energy ion scattering, Vacuum 84 (8) (2010) 1005–1007. doi:10.1016/j.vacuum.2009.11.016.

[21] T. M. Buck, Y. Chen, G. Wheatley, W. V. der Weg, Energy spectra of 632 keV neutral and ionized Ar and He scattered from Au targets; ionized fractions as functions of energy, Surf. Sci. 47 (1975) 244–255.
URL http://www.sciencedirect.com/science/article/pii/0029554X76907953http://www.sciencedirect.com/science/article/pii/0039602875902915

[22] M. Draxler, R. Gruber, H. H. Brongersma, P. Bauer, Velocity Scaling of Ion Neutralization in Low Energy Ion Scattering, Phys. Rev. Lett. 89 (26) (2002) 263201. doi:10.1103/PhysRevLett.89.263201.
URL http://link.aps.org/doi/10.1103/PhysRevLett.89.263201

[23] D. Primetzhofer, S. N. Markin, P. Zeppenfeld, P. Bauer, S. PrÅša, M. Kolíbal, T. Sikola, Quantitative analysis of ultra thin layer growth by time-of-flight low energy ion scattering, Appl. Phys. Lett. 92 (1) (2008) 011929. doi:10.1063/1.2822816.
URL http://link.aip.org/link/APPLAB/v92/i1/p011929/s1&Agg=doi

[24] D. Primetzhofer, M. Spitz, E. Taglauer, P. Bauer, Resonant charge transfer in low-energy ion scattering: Information depth in the reionization regime., Surf. Sci. 605 (21-22) (2011) 1913–1917. doi:10.1016/j.susc.2011.07.006.
URL http://www.pubmedcentral.nih.gov/articlerender.fcgi?artid=3165101&tool=pmcentrez&rendertype=abstract

[25] T. Buck, G. Wheatley, L. Feldman, Charge states of 25150 keV H and 4He backscattered from solid surfaces, Surf. Sci. 35 (1973) 345–361. doi:10.1016/0039-6028(73)90224-0.
URL http://linkinghub.elsevier.com/retrieve/pii/0039602873902240

[26] W. Wilson, M. Baskes, C. Bisson, Atomistics of helium bubble formation in a face-centered-cubic metal, Phys. Rev. B: Condens. Matter Mater. Phys. 13 (6) (1976) 2470–2478. doi:10.1103/PhysRevB.13.2470.
URL http://journals.aps.org/prb/abstract/10.1103/PhysRevB.13.2470http://link.aps.org/doi/10.1103/PhysRevB.13.2470

[27] R. Livengood, S. Tan, Y. Greenzweig, J. Notte, S. McVey, Subsurface damage from helium ions as a function of dose, beam energy, and dose rate, J. Vac. Sci. Technol., B: Microelectron. Nanometer Struct. 27 (6) (2009) 3244. doi:10.1116/1.3237101.
URL http://link.aip.org/link/JVTBD9/v27/i6/p3244/s1&Agg=doi

[28] S. Tan, R. H. Livengood, D. Shima, J. A. Notte, S. McVey, Gas field ion source and liquid metal ion source charged particle material interaction study for semiconductor nanomachining applications, J. Vac. Sci. Technol., B: Microelectron. Nanometer Struct. 28 (6) (2010) C6F15. doi:10.1116/1.3511509.
URL http://link.aip.org/link/JVTBD9/v28/i6/pC6F15/s1&Agg=doi

[29] V. Veligura, G. Hlawacek, R. P. Berkelaar, R. van Gastel, H. J. W. Zandvliet, B. Poelsema, Digging gold: keV He+ ion interaction with Au, Beilstein J. Nanotechnol. 4 (2013) 453–460. doi:10.3762/bjnano.4.53.
URL http://www.beilstein-journals.org/bjnano/content/4/1/53

[30] D. A. Wollman, K. D. Irwin, G. C. Hilton, L. L. Dulcie, D. E. Newbury, J. M. Martinis, High resolution, energy dispersive microcalorimeter spectrometer for x-ray microanalysis, J. Microsc. 188 (3) (1997) 196–223. doi:10.1046/j.1365-2818.1997.2670824.x.
URL <Go$\delimiter"026E30F$nto$\delimiter"026E30F$nISI>://000071375100002

[31] S. Abo, T. Azuma, T. Lohner, F. Wakaya, M. Takai, Study on spatial resolution of three-dimensional analysis by full count TOF-RBS with beryllium nanoprobe, Nucl. Instrum. Methods Phys. Res., Sect. B 273 (2012) 266–269. doi:10.1016/j.nimb.2011.07.091.
URL http://dx.doi.org/10.1016/j.nimb.2011.07.091

[32] T. Kobayashi, A. Kamoshida, H. Akiyama, K. Watanabe, T. Ohnishi, K. Takada, T. T. Suzuki, Development of microscopy for lithium analysis using medium-energy ion-stimulated desorption, Appl. Phys. Express 7 (10) (2014) 106601. doi:10.7567/APEX.7.106601.

[33] C. Xu, H. D. Lee, S. Shubeita, G. Liu, Y. Xu, L. Wielunski, J. Bloch, B. Yakshinskiy, E. Garfunkel, T. Gustafsson, L. C. Feldman, Atomic collisions in materials analysis, International Conference on Atomic Collisions in Solids (Conference), Debrecen, 2014.

[34] R. van Gastel, G. Hlawacek, S. Dutta, B. Poelsema, Backscattered helium spectroscopy in the helium ion microscope: Principles, resolution and

applications, Nucl. Instrum. Methods Phys. Res., Sect. B 344 (2015) 44–49. doi:10.1016/j.nimb.2014.11.073.

[35] L. R. Doolittle, Algorithms for the rapid simulation of Rutherford backscattering spectra, Nucl. Instruments Methods Phys. Res. Sect. B Beam Interact. with Mater. Atoms 9 (3) (1985) 344–351. doi:10.1016/0168-583X(85)90762-1.
URL http://linkinghub.elsevier.com/retrieve/pii/0168583X85907621

[36] N. P. Barradas, C. Jeynes, R. P. Webb, Simulated annealing analysis of Rutherford backscattering data, Appl. Phys. Lett. 71 (2) (1997) 291. doi:10.1063/1.119524.
URL http://scitation.aip.org/content/aip/journal/apl/71/2/10.1063/1.119524

[37] M. Mayer, SIMNRA, a simulation program for the analysis of NRA, RBS and ERDA, in: AIP Conf. Proc., AIP, 1999, pp. 541–544. doi:10.1063/1.59188.
URL http://scitation.aip.org/content/aip/proceeding/aipcp/10.1063/1.59188

[38] J. F. Ziegler, J. P. Biersack, M. D. Ziegler, SRIM, the stopping and range of ions in matter, SRIM Co., Chester, 2008.
URL http://www.worldcat.org/isbn/096542071http://books.google.com/books?vid=ISBN096542071http://www.amazon.com/gp/search?keywords=096542071&index=books&linkCode=qshttp://www.librarything.com/isbn/096542071http://www.worldcat.org/oclc/191686602

[39] W. Möller, W. Eckstein, Tridyn A TRIM simulation code including dynamic composition changes, Nucl. Instrum. Methods Phys. Res., Sect. B 2 (1-3) (1984) 814–818. doi:10.1016/0168-583X(84)90321-5.
URL http://dx.doi.org/10.1016/0168-583X(84)90321-5

[40] F. Schiettekatte, Fast Monte Carlo for ion beam analysis simulations, Nucl. Instrum. Methods Phys. Res., Sect. B 266 (8) (2008) 1880–1885. doi:10.1016/j.nimb.2007.11.075.

[41] J. Biersack, E. Steinbauer, P. Bauer, A particularly fast TRIM version for ion backscattering and high energy ion implantation 61 (1) (1991) 77–82. doi:10.1016/0168-583X(91)95564-T.
URL http://www.sciencedirect.com/science/article/pii/0168583X9195564T

[42] G. Andersson, H. Morgner, Impact collision ion scattering spectroscopy (ICISS) and neutral impact collision ion scattering spectroscopy (NICISS) at surfaces of organic liquids, Surf. Sci. 405 (1) (1998) 138–151. doi:10.1016/S0039-6028(98)00062-4.
URL http://linkinghub.elsevier.com/retrieve/pii/S0039602898000624

[43] H. D. Hagstrum, Low energy de-excitation and neutralization processes near surfaces, in: Inelast. ion-surface collisions, Academic New York, 1976, p. 1. doi:nichtverf\"{u}gbar?
URL https://books.google.de/books?id=ssxWsu9pvlYC

[44] K. Hayashi, H. Takayama, M. Ishikawa, S. Abo, T. Lohner, M. Takai, TOF-RBS with medium energy heavy ion probe for semiconductor process analysis, Nucl. Instrum. Methods Phys. Res., Sect. B 219-220 (1-4) (2004) 589–592. doi:10.1016/j.nimb.2004.01.125.

[45] D. Dowsett, T. Wirtz, N. Vanhove, L. Pillatsch, S. Sijbrandij, J. Notte, Secondary ion mass spectrometry on the helium ion microscope: A feasibility study of ion extraction, J. Vac. Sci. Technol., B: Microelectron. Nanometer Struct.: 30 (6) (2012) 06F602. doi:10.1116/1.4754309.

[46] Y. V. Petrov, O. F. Vyvenko, A. S. Bondarenko, Scanning helium ion microscope: Distribution of secondary electrons and ion channeling, J. Surf. Invest.: X-Ray, Synchrotron Neutron Tech. 4 (5) (2010) 792–795. doi:10.1134/S1027451010050186.
URL http://link.springer.com/10.1134/S1027451010050186

[47] T. Reinert, D. Spemann, M. Morawski, T. Arendt, Quantitative trace element analysis with sub-micron lateral resolution, Nucl. Instrum. Methods Phys. Res., Sect. B 249 (1-2) (2006) 734–737. doi:10.1016/j.nimb.2006.03.129.
URL http://linkinghub.elsevier.com/retrieve/pii/S0168583X06003648

[48] F. Watt, J. van Kan, I. Rajta, A. Bettiol, T. Choo, M. Breese, T. Osipowicz, The National University of Singapore high energy ion nano-probe facility: Performance tests, Nucl. Instrum. Methods Phys. Res., Sect. B 210 (2003) 14–20. doi:10.1016/S0168-583X(03)01003-6.
URL http://linkinghub.elsevier.com/retrieve/pii/S0168583X03010036

Statistics

Image: HZDR/E. Josten

Publications and patents

Books and chapters

1. Erbe, A.
   Electrical Conductance of DNA Oligomers — A Review of Experimental Results
   Eugen Stulz and Guido Clever: DNA in supramolecular chemistry and nanotechnology, John Wiley & Sons Limited (2015), ISBN 978-1-118-69686-6, 94-101
2. Hinsche, N. F.; Hölzer, M.; Ernst, A.; Mertig, I.; Zahn, P.
   Ab intio description of thermoelectric properties based on the Boltzmann theory
   Eibl, Nielsch, Peranio, Völklein: Thermoelectric Bi_2Te_3 Nanomaterials, Weinheim: Wiley-VCH (2015), ISBN 978-3-527-33489-6, 187-221
3. Sebastian, T.; Hillebrands, B.
   $Co_2Mn_{0.6}Fe_{0.4}Si$: A Heusler compound opening new perspectives in magnon spintronics
   Claudia Felser, Atsufumi Hirohata: Heusler Alloys - Properties, Growth, Applications, Springer Series in Materials Science **222**, Springer International Publishing (2015), ISBN 978-3-319-21448-1, 321-340

Publications in journals

Magnetism

1. Basith, M.; McVitie, S.; Strache, T.; Fritzsche, M.; Mücklich, A.; Fassbender, J.; McCord, J.
   Lorentz TEM Imaging of Stripe Structures Embedded in a Soft Magnetic Matrix
   Physical Review Applied **4**, 034012 (2015)
2. Duan, Z.; Krivorotov, I.; Arias, R.; Reckers, N.; Stienen, S.; Lindner, J.
   Spin wave eigenmodes in transversely magnetized thin film ferromagnetic wires
   Physical Review B **92**, 104424 (2015)
3. Feng, W.; Fowley, C.; Bernert, K.; Sluka, V.; Kowalska, E.; Aleksandrov, Y.; Lindner, J.; Fassbender, J.; Gan, H.; Kunz, A.; Hübner, R.; Coey, J. M. D.; Deac, A. M.
   Effect of deposition conditions and annealing temperature on tunnel magnetoresistance and structure of MgO-based double-barrier magnetic tunnel junctions
   IEEE Transactions on Magnetics **51**, 4400704 (2015)
4. Fowley, C.; Ouardi, S.; Kubota, T.; Oguz, Y.; Neudert, A.; Lenz, K.; Sluka, V.; Lindner, J.; Law, J. M.; Mizukami, S.; Fecher, G. H.; Felser, C.; Deac, A. M.
   Direct measurement of the magnetic anisotropy field in Mn-Ga and Mn-Co-Ga Heusler films
   Journal of Physics D: Applied Physics **48**, 164006 (2015)
5. Gliga, S.; Kákay, A.; Heyderman, L. J.; Hertel, R.; Heinonen, O. G.
   Broken vertex symmetry and finite zero-point entropy in the artificial square ice ground state
   Physical Review B **92**, 060413 (2015)
6. Hassdenteufel, A.; Schmidt, J.; Schubert, C.; Hebler, B.; Helm, M.; Albrecht, M.; Bratschitsch, R.
   Low-remanence criterion for helicity-dependent all-optical magnetic switching in ferrimagnets
   Physical Review B **91**, 104431 (2015)
7. Heidarian, A.; Bali, R.; Grenzer, J.; Wilhelm, R. A.; Heller, R.; Yildirim, O.; Lindner, J.; Potzger, K.
   Tuning the antiferromagnetic to ferromagnetic phase transition in FeRh thin films by means of low-energy/low fluence ion irradiation
   Nuclear Instruments and Methods in Physics Research B **358**, 251 (2015)

8. Hoffmann, A.; Schultheiss, H.
Mesoscale magnetism
Current Opinion in Solid State & Materials Science **19**, 253 (2015)

9. Khalid, M.; Gao, K.; Weschke, E.; Hübner, R.; Bähtz, C.; Gordan, O.; Salvan, G.; Zahn, D. R. T.; Skorupa, W.; Helm, M.; Zhou, S.
A comprehensive study of the magnetic, structural, and transport properties of the III-V ferromagnetic semiconductor InMnP
Journal of Applied Physics **117**, 043906 (2015)

10. Li, L.; Yuan, Y.; Zhang, Y.; Namiki, T.; Nishimura, K.; Pöttgen, R.; Zhou, S.
Giant low field magnetocaloric effect and field-induced metamagnetic transition in TmZn
Applied Physics Letters **107**, 132401 (2015)

11. Li, L.; Yuan, Y.; Zhang, Y.; Poettgen, R.; Zhou, S.
Magnetic phase transitions and large magnetic entropy change with a wide temperature span in HoZn
Journal of Alloys and Compounds **543**, 147 (2015)

12. Liebana-Vinas, S.; Wiedwald, U.; Elsukova, A.; Perl, J.; Zingsem, B.; Semisalova, A.; Salgueirino, V.; Spasova, M.; Farle, M.
Structure-Correlated Exchange Anisotropy in Oxidized $Co_{80}Ni_{20}$ Nanorods
Chemistry of Materials **27**, 4015 (2015)

13. Liedke, M. O.; Anwand, W.; Bali, R.; Cornelius, S.; Butterling, M.; Trinh, T. T.; Wagner, A.; Salamon, S.; Walecki, D.; Smekhova, A.; Wende, H.; Potzger, K.
Open volume defects and magnetic phase transition in $Fe_{60}Al_{40}$ transition metal aluminide
Journal of Applied Physics **117**, 163908 (2015)

14. Mazalski, P.; Sveklo, I.; Kurant, Z.; Ollefs, K.; Rogalev, A.; Wilhelm, F.; Fassbender, J.; Baczewski, L.; Wawro, A.; Maziewski, A.
XAS and XMCD studies of magnetic properties modifications of Pt/Co/Au and Pt/Co/Pt trilayers induced by Ga+ ions irradiation
Journal of Synchrotron Radiation **22**, 753 (2015)

15. Röder, F.; Hlawacek, G.; Wintz, S.; Hübner, R.; Bischoff, L.; Lichte, H.; Potzger, K.; Lindner, J.; Fassbender, J.; Bali, R.
Direct Depth- and Lateral- Imaging of Nanoscale Magnets Generated by Ion Impact
Scientific Reports **5**, 16786 (2015)

16. Rylkov, V. V.; Bugaev, A. S.; Novodvorskii, O. A.; Tugushev, V. V.; Kulatov, E. T.; Zenkevich, A. V.; Semisalova, A. S.; Nikolaev, S. N.; Vedeneev, A. S.; Shorokhova, A. V.; Aver′yanov, D. V.; Chernoglazov, K. Yu.; Gan′shina, E. A.; Granovsky, A. B.; Wang, Y.; Panchenko, V. Ya.; Zhou, S.
High-temperature ferromagnetism of $Si_{1-x}Mn_x$ (x≈0.52−0.55) alloys
Journal of Magnetism and Magnetic Materials **393**, 30 (2015)

17. Salikhov, R.; Semisalova, A. S.; Petruhins, A.; Ingason, A. S.; Rosen, J.; Wiedwald, U.; Farle, M.
Magnetic Anisotropy in $(Cr_{0.5}Mn_{0.5})_2GaC$ MAX Phase
Materials Research Letters **3**, 156 (2015)

18. Sebastian, T.; Schultheiss, K.; Obry, B.; Hillebrands, B.; Schultheiss, H.
Micro-focused Brillouin light scattering: imaging spin waves at the nanoscale
Frontiers in Physics **3**, 35 (2015)

19. Semisalova, A. S.; Mikhailovsky, Yu. O.; Smekhova, A.; Orlov, A. F.; Perov, N. S.; Gan'shina, E. A.; Lashkul, A.; Lahderanta, E.; Potzger, K.; Yildirim, O.; Aronzon, B.; Granovsky, A. B.
Above Room Temperature Ferromagnetism in Co- and V-Doped TiO_2 — Revealing the Different Contributions of Defects and Impurities
Journal of Superconductivity and Novel Magnetism **28**, 805 (2015)

20. Sluka, V.; Kákay, A.; Deac, A. M.; Bürgler, D. E.; Schneider, C. M.; Hertel, R.
Spin-torque-induced dynamics at fine-split frequencies in nano-oscillators with two stacked vortices
Nature Communications **6**, 6409 (2015)

21. Tahir, N.; Bali, R.; Gieniusz, R.; Mamica, S.; Gollwitzer, J.; Schneider, T.; Lenz, K.; Potzger, K.; Lindner, J.; Krawczyk, M.; Fassbender, J.; Maziewski, A.
Tailoring dynamic magnetic characteristics of $Fe_{60}Al_{40}$ films through ion irradiation
Physical Review B **92**, 144429 (2015)

22. Tahir, N.; Gieniusz, R.; Maziewski, A.; Bali, R.; Potzger, K.; Lindner, J.; Fassbender, J.
Evolution of magnetic domain structure formed by ion-irradiation of B2-$Fe_{0.6}Al_{0.4}$
Optics Express **23**, 16575 (2015)

23. Teichert, N.; Auge, A.; Yuzuak, E.; Dincer, I.; Elerman, Y.; Krumme, B.; Wende, H.; Yildirim, O.; Potzger, K.; Hütten, A.
Influence of film thickness and composition on the martensitic transformation in epitaxial Ni–Mn–Sn thin films
Acta Materialia **86**, 279 (2015)

24. Teichert, N.; Kucza, D.; Yildirim, O.; Yuzuak, E.; Dincer, I.; Behler, A.; Helmich, L.; Böhnke, A.; Klimova, S.; Waske, A.; Elerman, Y.; Hütten, A.
Structure and Giant Inverse Magnetocaloric Effect of Epitaxial Ni-Co-Mn-Al Films
Physical Review B **91**, 184405 (2015)

25. Wang, Y.; Liu, Y.; Wang, G.; Anwand, W.; Jenkins, C.; Arenholz, E.; Munnik, F.; Gordan, O.; Salvan, G.; Zahn, D. R. T.; Chen, X.; Gemming, S.; Helm, M.; Zhou, S.
Carbon p Electron Ferromagnetism in Silicon Carbide
Scientific Reports **5**, 8999 (2015)

26. Wang, Y.; Liu, Y.; Wendler, E.; Hübner, R.; Anwand, W.; Wang, G.; Chen, X.; Tong, W.; Yang, Z.; Munnik, F.; Bukalis, G.; Chen, X.; Gemming, S.; Helm, M.; Zhou, S.
Defect-induced magnetism in SiC: Interplay between ferromagnetism and paramagnetism
Physical Review B **92**, 174409 (2015)

27. Xu, Q.; Sheng, Y.; Khalid, M.; Cao, Y.; Wang, Y.; Qiu, X.; Zhang, W.; He, M.; Wang, S.; Zhou, S.; Li, Q.; Wu, D.; Zhai, Y.; Liu, W.; Wang, P.; Xu, Y.; Du, J.
Magnetic interactions in $BiFe_{0.5}Mn_{0.5}O_3$ films and $BiFeO_3/BiMnO_3$ superlattices
Scientific Reports **5**, 9093 (2015)

28. Yang, L.; Verba, R.; Tiberkevich, V.; Schneider, T.; Smith, A.; Duan, Z.; Youngblood, B.; Lenz, K.; Lindner, J.; Slavin, A. N.; Krivorotov, I. N.
Reduction of phase noise in nanowire spin orbit torque oscillators
Scientific Reports **5**, 16942 (2015)

29. Yildirim, O.; Cornelius, S.; Butterling, M.; Anwand, W.; Wagner, A.; Smekhova, A.; Fiedler, J.; Böttger, R.; Bähtz, C.; Potzger, K.
From a non-magnet to a ferromagnet: Mn implantation into different TiO_2 structures
Applied Physics Letters **107**, 242405 (2015)

30. Yildirim, O.; Cornelius, S.; Smekhova, A.; Zykov, G.; Ganshina, E.; Granovsky, A.; Hübner, R.; Bähtz, C.; Potzger, K.
The local environment of cobalt in amorphous, polycrystalline and epitaxial anatase TiO_2:Co films produced by cobalt ion implantation
Journal of Applied Physics **117**, 183901 (2015)

31. Yuan, Y.; Wang, Y.; Gao, K.; Khalid, M.; Wu, C.; Zhang, W.; Munnik, F.; Weschke, E.; Bähtz, C.; Skorupa, W.; Helm, M.; Zhou, S.
High Curie temperature and perpendicular magnetic anisotropy in homoepitaxial InMnAs films
Journal of Physics D: Applied Physics **48**, 235002 (2015)

32. Zhou, S.
Dilute ferromagnetic semiconductors prepared by the combination of ion implantation with pulse laser melting
Journal of Physics D: Applied Physics **48**, 263001 (2015)

Nanoscience and materials for information technologies

33. Bittencourt, C.; Ewels, C.; Krasheninnikov, A. V.
Atomic scale interface design and characterisation
Beilstein Journal of Nanotechnology **6**, 1708 (2015)

34. Bogusz, A.; Blaschke, D.; Skorupa, I.; Bürger, D.; Schmidt, O. G.; Schmidt, H.
Morphological transformations of top electrodes on $YMnO_3$ caused by filamentary resistive switching in the oxide matrix
Advanced Materials Research **1101**, 120 (2015)

35. Buljan, M.; Facsko, S.; Delač Marion, I.; Mikšić Trontl, V.; Kralj, M.; Jerčinović, M.; Baehtz, C.; Muecklich, A.; Holý, V.; Grenzer, J.; Radić, N.
Self-assembly of Ge quantum dots on periodically corrugated Si surfaces
Applied Physics Letters **107**, 203101 (2015)

36. Buljan, M.; Radic, N.; Sancho-Paramon, J.; Janicki, V.; Grenzer, J.; Bogdanovic-Radovic, I.; Siketic, Z.; Ivanda, M.; Utrobicic, A.; Hübner, R.; Weidauer, R.; Vales, V.; Endres, J.; Car, T.; Jercinovic, M.; Rosko, J.; Bernstorff, S.; Holy, V.
Production of three-dimensional quantum dot lattice of Ge/Si core-shell quantum dots and Si/Ge layers in an alumina glass matrix
Nanotechnology **26**, 065602 (2015)

37. Bussone, G.; Schäfer-Eberwein, H.; Dimakis, E.; Biermanns, A.; Carbone, D.; Tahraoui, A.; Geelhaar, L.; Haring Bolívar, P.; Schülli, T. U.; Pietsch, U.
Correlation of electrical and structural properties of single as-grown GaAs nanowires on Si (111) substrates
Nano Letters **15**, 981 (2015)

38. Ervasti, M. M.; Fan, Zh.; Uppstu, A.; Krasheninnikov, A. V.; Harju, A.
Silicon and silicon-nitrogen impurities in graphene: Structure, energetics, and effects on electronic transport
Physical Review B **92**, 235412 (2015)

39. Eßer, F.; Drachenko, O.; Patanè, A.; Ozerov, M.; Winnerl, S.; Schneider, H.; Helm, M.
Direct determination of the electron effective mass of GaAsN by terahertz cyclotron resonance spectroscopy
Applied Physics Letters **107**, 062103 (2015)

40. Fehrenbacher, M.; Winnerl, S.; Schneider, H.; Doring, J.; Kehr, S.; Eng, L.; Huo, Y.; Schmidt, O.; Yao, K.; Liu, Y.; Helm, M.
Plasmonic Superlensing in Doped GaAs
Nano Letters **15**, 1057 (2015)

41. Förster, A.; Wagner, C.; Gemming, S.; Schuster, J.
Theoretical investigation of an in situ k-restore process for damaged ultra-low-k materials based on plasma enhanced fragmentation
Journal of Vacuum Science & Technology B **33**, 052203 (2015)

42. Franke, C.; Walther, M.; Helm, M.; Schneider, H.
Two-photon quantum well infrared photodetectors below 6 THz
Infrared Physics and Technology **70**, 30 (2015)

43. Gruber, E.; Wilhelm, R. A.; Smejkal, V.; Heller, R.; Facsko, S.; Aumayr, F.
Interaction of highly charged ions with carbon nano membranes
Journal of Physics: Conference Series **635**, 012027 (2015)

44. Heera, V.; Fiedler, J.; Schmidt, B.; Hübner, R.; Voelskow, M.; Skrotzki, R.; Skorupa, W.
Negative magneto- and electroresistance of silicon films with superconducting nanoprecipitates - the role of inelastic cotunneling
Journal of Low Temperature Physics **180**, 342 (2015)

45. Heera, V.; Fiedler, J.; Skorupa, J.; Skorupa, W.
Resistance fluctuations in insulating silicon films with superconducting nanoprecipitates – superconductor-to-metal or vortex matter phase transition?
AIP Advances **5**, 117219 (2015)

46. Henke, T.; Knaut, M.; Hossbach, C.; Geidel, M.; Rebohle, L.; Albert, M.; Skorupa, W.; Bartha, J.
Flash-Enhanced Atomic Layer Deposition: Basics, Opportunities, Review, and Principal Studies on the Flash-Enhanced Growth of Thin Films
ECS Journal of Solid State Science and Technology **4**, 277 (2015)

47. Herbig, C.; Åhlgren, E. H.; Schröder, U. A.; Martínez-Galera, A. J.; Arman, M. A.; Kotakoski, J.; Knudsen, J.; Krasheninnikov, A. V.; Michely, T.
Xe irradiation of graphene on Ir(111): From trapping to blistering
Physical Review B **92**, 085429 (2015)

48. Hu, X.; Björkman, T.; Lipsanen, H.; Sun, L.; Krasheninnikov, A. V.
Solubility of boron, carbon, and nitrogen in transition metals: getting insight into trends from first-principles calculations
The Journal of Physical Chemistry Letters **6**, 3263 (2015)

49. Joswig, J.-O.; Lorenz, T.; Wendumu, T.; Gemming, S.; Seifert, G.
Optics, Mechanics, and Energetics of Two-Dimensional MoS_2 Nanostructures from a Theoretical Perspective
Accounts of Chemical Research **48**, 48 (2015)

50. Kelly, R. A.; Liedke, B.; Baldauf, S.; Gangnaik, A.; Biswas, S.; Georgiev, Y.; Holmes, J. D.; Posselt, M.; Petkov, N.
Epitaxial Post-Implant Recrystallization in Germanium Nanowires
Crystal Growth & Design **15**, 4581 (2015)

51. Klingner, N.; Heller, R.; Hlawacek, G.; von Borany, J.; Notte, J.; Huang, J.; Facsko, S.
Nanometer scale elemental analysis in the helium ion microscope using time of flight spectrometry
Ultramicroscopy **162**, 91 (2016)

52. Köhl, M.; Schroth, P.; Minkevich, A. A.; Hornung, J.-W.; Dimakis, E.; Somaschini, C.; Geelhaar, L.; Aschenbrenner, T.; Lazarev, S.; Grigoriev, D.; Pietsch, U.; Baumbach, T.
Polytypism in GaAs nanowires: determination of the interplanar spacing of wurtzite GaAs by X-ray diffraction
Journal of Synchrotron Radiation **22**, 67 (2015)

53. Kuschewski, F.; Kehr, S. C.; Green, B.; Bauer, C.; Gensch, M.; Eng, L. M.
Optical nanoscopy of transient states in condensed matter
Scientific Reports **5**, 12582 (2015)

54. Lehninger, D.; Seidel, P.; Geyer, M.; Schneider, F.; Klemm, V.; Rafaja, D.; von Borany, J.; Heitmann, J.
Charge trapping of Ge-nanocrystals embedded in $TaZrO_x$ dielectric films
Applied Physics Letters **106**, 023116 (2015)

55. Lin, Y.-C.; Komsa, H.-P.; Yeh, C.-H.; Björkman, T.; Liang, Z.-Y.; Ho, C.-H.; Huang, Y.-S.; Chiu, P.-W.; Krasheninnikov, A. V.; Suenaga, K.
Single-Layer RES_2: Two-Dimensional Semiconductor with Tunable In-Plane Anisotropy
ACS Nano **9**, 11249 (2015)

56. Mayer, B.; Schmidt, C.; Grupp, A.; Bühler, J.; Oelmann, J.; Marvel, R. E.; Haglund, R. F.; Oka, T.; Brida, D.; Leitenstorfer, A.; Pashkin, A.
Tunneling breakdown of a strongly correlated insulating state in VO_2 induced by intense multiterahertz excitation
Physical Review B **91**, 235113 (2015)

57. Miller, T. A.; Chhaajlany, R. W.; Tagliacozzo, L.; Green, B.; Kovalev, S.; Prabhakaran, D.; Lewenstein, M.; Gensch, M.; Wall, S.
Terahertz field control of in-plane orbital order in $La_{0.5}Sr_{1.5}MnO_4$
Nature Communications **6**, 8175 (2015)

58. Mittendorff, M.; Kamann, J.; Eroms, J.; Weiss, D.; Drexler, C.; Ganichev, S. D.; Kerbusch, J.; Erbe, A.; Suess, R. J.; Murphy, T. E.; Chatterjee, S.; Kolata, K.; Ohser, J.; König-Otto, J. C.; Schneider, H.; Helm, M.; Winnerl, S.
Universal ultrafast detector for short optical pulses based on graphene
Optics Express **23**, 28728 (2015)

59. Mittendorff, M.; Wendler, F.; Malic, E.; Knorr, A.; Orlita, M.; Potemski, M.; Berger, C.; de Heer, W. A.; Schneider, H.; Helm, M.; Winnerl, S.
Carrier dynamics in Landau-quantized graphene featuring strong Auger scattering
Nature Physics **11**, 75 (2015)

60. Ou, X.; Heinig, K.-H.; Hübner, R.; Grenzer, J.; Wang, X.; Helm, M.; Fassbender, J.; Facsko, S.
Faceted nanostructure arrays with extreme regularity controlled vacancy by vacancy
Nanoscale **7**, 18928 (2015)

61. Pavlov, S. G.; Deßmann, N.; Pohl, A.; Abrosimov, N. V.; Mittendorff, M.; Winnerl, S.; Zhukavin, R. Kh.; Tsyplenkov, V. V.; Shengurov, D. V.; Shastin, V. N.; Hübers, H.-W.
Towards a life-time-limited 8-octave-infrared photoconductive germanium detector
Journal of Physics: Conference Series **647**, 012070 (2015)

62. Persechini, L.; Verre, R.; Smith, C. M.; Fleischer, K.; Shvets, I. V.; Ranjan, M.; Facsko, S.; Mcgilp, J. F.
Optical characterisation of plasmonic nanostructures on planar substrates using second harmonic generation
Optics Express **23**, 26486 (2015)

63. Preu, S.; Mittendorff, M.; Winnerl, S.; Cojocari, O.; Penirschke, A.
THz Autocorrelators for ps Pulse Characterization Based on Schottky Diodes and Rectifying Field-Effect Transistors
IEEE Transactions on Terahertz Science and Technology **5**, 922 (2015)

64. Prucnal, S.; Gao, K.; Skorupa, I.; Rebohle, L.; Vines, L.; Schmidt, H.; Khalid, M.; Wang, Y.; Weschke, E.; Skorupa, W.; Grenzer, J.; Hübner, R.; Helm, M.; Zhou, S.
Band-gap narrowing in Mn-doped GaAs probed by room-temperature photoluminescence
Physical Review B **92**, 224407 (2015)

65. Radek, M.; Bracht, H.; Johnson, B. C.; McCallum, J. C.; Posselt, M.; Liedke, B.
Atomic transport during solid-phase epitaxial recrystallization of amorphous germanium
Applied Physics Letters **107**, 082112 (2015)

66. Regensburger, S.; Mittendorff, M.; Winnerl, S.; Lu, H.; Gossard, A. C.; Preu, S.
Broadband THz detection from 0.1 to 22 THz with large area field-effect transistors
Optics Express **23**, 20732 (2015)

67. Rentrop, S.; Abendroth, B.; Walter, J.; Rensberg, J.; Münchgesang, W.; Strohmeyer, R.; Stöcker, H.; Ronning, C.; Gemming, S.; Meyer, D. C.
Stoichiometry variation for the atomic layer deposition of $Sr_xTi_yO_z$ from $Sr(^iPr_3Cp)_2$, $Ti[N(CH_3)_2]_4$ and H_2O
Thin Solid Films **577**, 134 (2015)

68. Riise, H. N.; Schumann, T.; Azarov, A.; Hübner, R.; Skorupa, W.; Svensson, B. G.; Monakhov, E.
Formation of shallow boron emitters in crystalline silicon using flash lamp annealing: Role of excess silicon interstitials
Applied Physics Letters **107**, 022105 (2015)

69. Schroth, P.; Köhl, M.; Hornung, J.-W.; Dimakis, E.; Somaschini, C.; Geelhaar, L.; Biermanns, A.; Pietsch, U.; Bauer, S.; Lazarev, S.; Baumbach, T.
Evolution of polytypism in GaAs nanowires during growth revealed by time-resolved in situ x-ray diffraction
Physical Review Letters **114**, 055504 (2015)

70. Sendler, T.; Luka-Guth, K.; Wieser, M.; Lokamani, M.; Wolf, J.; Helm, M.; Gemming, S.; Kerbusch, J.; Scheer, E.; Huhn, T.; Erbe, A.
Light-Induced Switching of Tunable Single-Molecule Junctions
Advanced Science **2**, 1500017 (2015)

71. Smejkal, V.; Gruber, E.; Kralik, M.; Wilhelm, R. A.; Heller, R.; Facsko, S.; Aumayr, F.
Interaction of multiply charged ions with single layer graphene Part I: Charge exchange and energy loss
Journal of Physics: Conference Series **635**, 032002 (2015)

72. Spirin, K. E.; Krishtopenko, S. S.; Sadofyev, Yu. G.; Drachenko, O.; Helm, M.; Teppe, F.; Knap, W.; Gavrilenko, V. I.
Cyclotron Resonance in InAs/AlSb Quantum Wells in Magnetic Fields up to 45 T
Semiconductors **49**, 1616 (2015)

73. Teschome, B.; Facsko, S.; Gothelf, K. V.; Keller, A.
Alignment of Gold Nanoparticle-Decorated DNA Origami Nanotubes: Substrate Prepatterning versus Molecular Combing
Langmuir **31**, 12823 (2015)

74. Wendler, F. H. Funk; Mittendorff, M.; Winnerl, S.; Helm, M.; Knorr, A.; Malic, E.
Efficient Auger scattering in Landau-quantized graphene
Proceedings of SPIE **9361**, 936105 (2015)

75. Wilhelm, R. A.; El-Said, A. S.; Krok, F.; Heller, R.; Gruber, E.; Aumayr, F.; Facsko, S.
Highly charged ion induced nanostructures at surfaces by strong electronic excitations
Progress in Surface Science **90**, 377 (2015)

76. Wilhelm, R. A.; Gruber, E.; Ritter, R.; Heller, R.; Beyer, A.; Turchanin, A.; Klingner, N.; Hübner, R.; Stöger-Pollach, M.; Vieker, H.; Hlawacek, G.; Gölzhäuser, A.; Facsko, S.; Aumayr, F.
Threshold and Efficiency for Pore Formation in 1nm Thick Carbon Nanomembranes by Slow Highly Charged Ions
2D Materials **2**, 035009 (2015)

77. Wilhelm, R. A.; Gruber, E.; Ritter, R.; Heller, R.; Facsko, S.; Aumayr, F.
Threshold and Efficiency for Perforation of 1nm Thick Carbon Nanomembranes with Slow Highly Charged Ions
Journal of Physics: Conference Series **635**, 032011 (2015)

78. Wutzler, R.; Rebohle, L.; Prucnal, S.; Bregolin, F.; Hübner, R.; Voelskow, M.; Helm, M.; Skorupa, W.
Liquid phase epitaxy of binary III-V nanocrystals in thin Si layers triggered by ion implantation and flash lamp annealing
Journal of Applied Physics **117**, 175307 (2015)

79. Wylezich, H.; Mähne, H.; Heinrich, A.; Slesazeck, S.; Rensberg, J.; Ronning, C.; Zahn, P.; Mikolajick, T.
Adjusting the Forming Step for Resistive Switching in Nb_2O_5 by Ion Irradiation
Journal of Vacuum Science & Technology B **33**, 01A105 (2015)

80. Zhou, S.; Liu, F.; Prucnal, S.; Gao, K.; Khalid, M.; Bähtz, C.; Posselt, M.; Skorupa, W.; Helm, M.
Hyperdoping silicon with selenium: solid vs. liquid phase epitaxy
Scientific Reports **5**, 8329 (2015)

Materials for energy and transport technologies

81. Bergner, F.; Gillemot, F.; Hernández-Mayoral, M.; Serrano, M.; Török, G.; Ulbricht, A.; Altstadt, E.
Contributions of Cu-rich clusters, dislocation loops and nanovoids to the irradiation-induced hardening of Cu-bearing low-Ni reactor pressure vessel steels
Journal of Nuclear Materials **461**, 37 (2015)

82. Devaraj, M.; Posselt, M.; Schiwarth, M.
First-principles calculation of defect free energies: General aspects illustrated in the case of bcc-Fe
Physical Review B **92**, 064103 (2015)

83. Hilger, I.; Bergner, F.; Weißgärber, T.
Bimodal grain size distribution of nanostructured ferritic ODS Fe-Cr alloys
Journal of the American Ceramic Society **98**, 3576 (2015)

84. Rouden, J.; Hein, H.; May, J.; Planman, T.; Todeschini, P.; Brumovsky, M.; Ballesteros, A.; Gillemot, F.; Chaouadi, R.; Efsing, P.; Altstadt, E.
Towards safe long-term operation of reactor pressure vessels
atw - International Journal for Nuclear Power **60**, 287 (2015)

85. Tusheva, P.; Altstadt, E.; Willschütz, H.-G.; Fridman, E.; Weiß, F.-P.
Investigations on in-vessel melt retention by external cooling for a generic VVER-1000 reactor
Annals of Nuclear Energy **75**, 249 (2015)

86. Viehrig, H.-W.; Altstadt, E.; Houska, M.
Radiation response of the overlay cladding from the decommissioned WWER-440 Greifswald unit 4 reactor pressure vessel
Nuclear Engineering and Design **286**, 227 (2015)

87. Viehrig, H.-W.; Houska, M.; Altstadt, E.
Radiation and annealing response of WWER 440 beltline welding seams
Journal of Nuclear Materials **456**, 334 (2015)

88. Viehrig, H.-W.; Houska, M.; Kalkhof, D.; Schindler, H.-J.
Fracture mechanics characterisation of reactor pressure vessel multi-layer weld metal
International Journal of Pressure Vessels and Piping **135-136**, 36 (2015)

Other topics and external users of ion beam center and free-electron laser

89. Bacco, D.; Corso, A. J.; Zuppella, P.; Böttger, R.; Gerlin, F.; Napolitani, E.; Tessarolo, E.; Nardello, M.; Pelizzo, M. G.
Study of solar wind ions implantation effects in optical coatings in view of Solar Orbiter space mission operation
Proceedings of SPIE **9604**, 960407 (2015)

90. Bacco, D.; Corso, A. J.; Zuppella, P.; Gerlin, F.; Böttger, R.; Napolitani, E.; Tessarolo, E.; Nardello, M.; Zuccon, S.; Pelizzo, M. G.
He^+ ions damage on optical coatings for solar missions
Proceedings of SPIE **9510**, 95100B (2015)

91. Bilek, M. M. M.; Kondyurin, A.; Dekker, S. A.; Steel, B. C.; Wilhelm, R. A.; Heller, R.; McKenzie, D. R.; Weiss, A. S.; James, M.; Möller, W.
Depth Resolved Structural and Compositional Characterization of Ion-Implanted Polystyrene that Enables Direct Covalent Immobilization of Biomolecules
Journal of Physical Chemistry C **119**, 16793 (2015)

92. Cai, H.; Liang, P.; Hübner, R.; Zhou, S.; Li, Y.; Sun, J.; Xu, N.; Wu, J.
Composition and bandgap control of $Al_xGa_{1-x}N$ films synthesized by plasma-assisted pulsed laser deposition
Journal of Materials Chemistry C **3**, 5307 (2015)

93. Caneva, S.; Weatherup, R. S.; Bayer, B. C.; Brennan, B.; Spencer, S. J.; Mingard, K.; Cabrero-Vilatela, A.; Baehtz, C.; Pollard, A. J.; Hofmann, S.
Nucleation Control for Large, Single Crystalline Domains of Monolayer Hexagonal Boron Nitride via Si-Doped Fe Catalysts
Nano Letters **15**, 1867 (2015)

94. Cantelli, V.; Geaymond, O.; Ulrich, O.; Zhou, T.; Blanc, N.; Renaud, G.
The In situ growth of nanostructures on surfaces (INS) endstation of the ESRF BM32 beamline: A combined UHV–CVD and MBE reactor for in situ X-ray scattering investigations of growing nanoparticles and semiconductor nanowires
Journal of Synchrotron Radiation **22**, 688 (2015)

95. Cavaleiro, A. J.; Ramos, A. S.; Martins, R. M. S.; Braz Fernandes, F. M.; Morgiel, J.; Bähtz, C.; Vieira, M. T.
Phase transformations in Ni/Ti multilayers investigated by synchrotron radiation-based x-ray diffraction
Journal of Alloys and Compounds **645**, 1165 (2015)

96. Chen, C.; Luan, Q.; He, R.; Cheng, C.; Akhmadaliev, S.; Zhou, S.; Yu, H.; Zhang, H.; Chen, F.
Ridge waveguides in Nd:ABC_3O_7 disordered crystals produced by swift C^{5+} ion irradiation and precise diamond dicing: Broad band guidance and spectroscopic properties
Optics and Laser Technology **68**, 84 (2015)

97. Cheng, Y.; Lv, J.; Akhmadaliev, S.; Zhou, S.; Kong, Y.; Chen, F.
Mid-infrared ridge waveguide in MgO:$LiNbO_3$ crystal produced by combination of swift O^{5+} ion irradiation and precise diamond blade dicing
Optical Materials **48**, 209 (2015)

98. Cheng, Y.; Lv, J.; Akhmadaliev, Sh.; Hernández-Palmero, I.; Romero, C.; Vázquez De Aldana, J. R.; Zhou, S.; Chen, F.
Optical ridge waveguides in Yb:YAG laser crystal produced by combination of swift carbon ion irradiation and femtosecond laser ablation
Optics and Laser Technology **72**, 100 (2015)

99. Cherkouk, C.; Rebohle, L.; Lenk, J.; Keller, A.; Ou, X.; Laubec, M.; Neuber, C.; Haase-Kohn, C.; Pietzsch, J.; Skorupa, W.
Controlled immobilization of His-tagged proteins for protein-ligand interaction experiments using Ni^{2+}-NTA layer on glass surfaces
Clinical Hemorheology and Microcirculation **61**, 523 (2015)

100. Csato, C.; Krippendorf, F.; Akhmadaliev, S.; von Borany, J.; Han, W.; Siefke, T.; Zowalla, A.; Rüb, M.
Energy filter for tailoring depth profiles in semiconductor doping application
Nuclear Instruments and Methods in Physics Research B **365**, 182 (2015)

101. Depalo, R.; Cavanna, F.; Ferraro, F.; Slemer, A.; Al-Abdullah, T.; Akhmadaliev, S.; Anders, M.; Bemmerer, D.; Elekes, Z.; Mattei, G.; Reinicke, S.; Schmidt, K.; Scian, C.; Wagner, L.
Strengths of the resonances at 436, 479, 639, 661, and 1279 keV in the $^{22}Ne(p,\gamma)^{23}Na$ reaction
Physical Review C **92**, 045807 (2015)

102. Deßmann, N.; Pavlov, S. G.; Pohl, A.; Abrosimov, N. V.; Winnerl, S.; Mittendorff, M.; Zhukavin, R. Kh.; Tsyplenkov, V. V.; Shengurov, D. V.; Shastin, V. N.; Hübers, H.-W.
Lifetime-limited, sub-nanosecond terahertz germanium photoconductive detectors
Applied Physics Letters **106**, 171109 (2015)

103. Du, N.; Kiani, M.; Mayr, C.; You, T.; Buerger, D.; Skorupa, I.; Schmidt, O.; Schmidt, H.
Single pairing spike-timing dependent plasticity in $BiFeO_3$ memristors with a time window of 25ms to 125µs
Frontiers in Neuroscience **9**, 227 (2015)

104. Duan, K. J.; Zhang, L.; Yuan, X. Z.; Han, S. S.; Liu, Y.; Huang, Q. S.
Effect of an upward magnetic field on nanosized sulfide precipitation in ultra-low carbon steel
International Journal of Minerals, Metallurgy & Materials **22**, 714 (2015)

105. Enghardt, S.; Richter, G.; Richter, E.; Reitemeier, B.; Walter, M. H.
Experimental investigations on the influence of adhesive oxides on the metal-ceramic bond
Metals **5**, 119 (2015)

106. England, J.; Möller, W.
Industrial challenges in ion beam processing and metrology in the 3D era
Nuclear Instruments and Methods in Physics Research B **365**, 105 (2015)

107. Florentin, M.; Alexandru, M.; Constant, A.; Schmidt, B.; Godignon, P.
10 MeV Proton Irradiation Effect on 4H-SiC n-MOSFET Electrical Parameters
Materials Science Forum **806**, 121 (2015)

108. Fuchs, M. C.; Gloaguen, R.; Merchel, S.; Pohl, E.; Sulaiman, V.; Andermann, C.; Rugel, G.
Millennial erosion rates across the Pamir based on ^{10}Be concentrations in fluvial sediments: Dominance of topographic over climatic factors
Earth Surface Dynamics Discussion **3**, 83 (2015)

109. Fuchs, M. C.; Gloaguen, R.; Merchel, S.; Pohl, E.; Sulaymonova, Vasila A.; Andermann, C.; Rugel, G.
Denudation rates across the Pamir based on ^{10}Be concentrations in fluvial sediments: dominance of topographic over climatic factors
Earth Surface Dynamics **3**, 423 (2015)

110. Gaiduk, Peter I.; Hansen, J. L.; Larsen, A. N.; Skorupa, W.
Comparative study of defect evolution in carbon implanted strained SiGe and SiSn layers
Physica Status Solidi (C) **12**, 120 (2015)

111. González, C.; Panizo-Laiz, M.; Gordillo, N.; Tejado, E.; Munnik, F.; Guerrero, C.; Piaggi, P.; Iglesias, R.; Perlado, J. M.; González-Arrabal, R.
H trapping and mobility in nanostructured tungsten grain boundaries: A combined experimental and theoretical approach
Nuclear Fusion **55**, 113009 (2015)

112. Grundke, K.; Pöschel, K.; Synytska, A.; Frenzel, R.; Drechsler, A.; Nitschke, M.; Cordeiro, A. L.; Uhlmann, P.; Welzel, P. B.
Experimental studies of contact angle hysteresis phenomena on polymer surfaces — Toward the understanding and control of wettability for different applications
Advances in Colloid and Interface Science **222**, 350 (2015)

113. Guillen, E.; Heras, I.; Rincon Llorente, G.; Lungwitz, F.; Alcon-Camas, M.; Escobar-Galindo, R.
Room temperature deposition of highly dense TiO_2 thin films by filtered cathodic vacuum arc
Proceedings of SPIE **9558**, 95580S (2015)

114. Husar, R.; Hübner, R.; Hennig, C.; Martin, P. M.; Chollet, M.; Weiss, S.; Zänker, H.; Stumpf, T.; Ikeda-Ohno, A.
Intrinsic formation of nanocrystalline neptunium dioxide under neutral aqueous conditions relevant to deep geological repositories
Chemical Communications **51**, 1301 (2015)

115. Jia, J. Y.; Wang, T. M.; Zhang, Y. H.; Shen, W. Z.; Schneider, H.
High-temperature photon-noise-limited performance terahertz quantum-well photodetectors
IEEE Transactions on Terahertz Science and Technology **5**, 715 (2015)

116. Karlušić, M.; Kozubek, R.; Lebius, H.; Ban-D'Etat, B.; Wilhelm, R. A.; Buljan, M.; Siketić, Z.; Scholz, F.; Meisch, T.; Jakšić, M.; Bernstorff, S.; Schleberger, M.; Šantić, B.
Response of GaN to energetic ion irradiation: conditions for ion track formation
Journal of Physics D: Applied Physics **48**, 325304 (2015)

117. Koller, C. M.; Ramm, J.; Polcik, P.; Munnik, F.; Paulitsch, J.; Mayrhofer, P. H.
Corundum-type Fe-doped cathodic arc evaporated Al-Cr-O coatings
Scripta Materialia **97**, 49 (2015)

118. Krauß, N.; Haas, M.; Niemeyer, L.; Winnerl, S.; Helm, M.; Dekorsy, T.
Terahertz emission based on large-area photoconductive emitters illuminated via beam interference
Electronics Letters **51**, 1357 (2015)

119. Lederer, S.; Akhmadaliev, S.; Forck, P.; Gütlich, E.; Lieberwirth, A.; Ensinger, W.
Thermal annealing behavior of α-Al_2O_3 scintillation screens
Nuclear Instruments and Methods in Physics Research B **365**, 548 (2015)

120. Lederer, S.; Akhmadaliev, S.; von Borany, J.; Gütlich, E.; Lieberwirth, A.; Zimmermann, J.; Ensinger, W.
High-temperature scintillation of alumina under 32 MeV $^{63}Cu^{5+}$ heavy-ion irradiation
Nuclear Instruments and Methods in Physics Research B **359**, 161 (2015)

121. Luan, Q.; Tan, Y.; Akhmadaliev, S.; Zhou, S.; Yu, H.; Zhang, H.; Chen, F.
Optical ridge waveguides in Nd:CNGG disorder laser crystal produced by combination of carbon ion irradiation and precise diamond blade dicing
Optical Materials **39**, 247 (2015)

122. Manova, D.; Díaz, C.; Pichon, L.; Abrasonis, G.; Mändl, S.
Comparability and accuracy of nitrogen depth profiling in nitrided austenitic stainless steel
Nuclear Instruments and Methods in Physics Research B **349**, 106 (2015)

123. Maryško, M.; Hejtmánek, J.; Laguta, V.; Sofer, Z.; Sedmidubský, D.; Šimek, P.; Veselý, M.; Mikulics, M.; Buchal, C.; Macková, A.; Malínský, P.; Wilhelm, R. A.
Ferromagnetic and paramagnetic magnetization of implanted GaN:Ho,Tb,Sm,Tm films
Journal of Applied Physics **117**, 17B907 (2015)

124. Meunier, C.; Vives, S.; Munnik, F.; Berthout, G.; Mikhailov, S.
Effect on microstructure and hardness of 1 MeV carbon ion implantation in Al, Co and W
Surface & Coatings Technology **262**, 191 (2015)

125. Minikayev, R.; Paszkowicz, W.; Piszora, P.; Knapp, M.; Bähtz, C.; Podsiadlo, S.
Thermal expansion of polycrystalline gallium nitride: an X-ray diffraction study
X-Ray Spectrometry **44**, 382 (2015)

126. Neelmeijer, C.; Roscher, R.
Gehört der Deckel zur Vase? Protonenstrahl-Analyse bringt Klarheit bei der Prüfung Meißener Deckelvase
Restauro **121** (4), 16 (2015)

127. Nekvindova, P.; Mackova, A.; Malinsky, P.; Cajzl, J.; Svecova, B.; Oswald, J.; Wilhelm, R. A.
Erbium-ion implantation into various crystallographic cuts of Al_2O_3
Nuclear Instruments and Methods in Physics Research B **365**, 89 (2015)

128. Nowak, S. H.; Bjeoumikhov, A.; von Borany, J.; Buchriegler, J.; Munnik, F.; Petric, A.; Renno, A. D.; Radtke, A.; Reinholz, U.; Scharf, O.; Strüder, L.; Wedell, R.; Ziegenrücker, R.
Examples of XRF and PIXE imaging with few microns Resolution using SLcam® – a Color X-Ray Camera
X-Ray Spectrometry **44**, 135 (2015)

129. Nowak, S. H.; Bjeoumikhov, A.; von Borany, J.; Buchriegler, J.; Munnik, F.; Petric, M.; Radtke, M.; Renno, A. D.; Reinholz, U.; Scharf, O.; Wedell, R.
Sub-pixel resolution with a color X-ray camera
Journal of Analytical Atomic Spectrometry **30**, 1890 (2015)

130. Satyarthi, P.; Ghosh, S.; Wang, Y.; Zhou, S.; Kumar, P.; Kanjilal, D.; Olivi, L.; Bürger, D.; Skorupa, I.; Schmidt, H.; Srivastava, P.
Probing defect driven tunable spontaneous magnetization in paramagnetic $Zn_{0.95}Co_{0.05}O$ epitaxial films by X-ray absorption investigations
Journal of Alloys and Compounds **649**, 891 (2015)

131. Schmidt, J.; Winnerl, S.; Seidel, W.; Bauer, C.; Gensch, M.; Schneider, H.; Helm, M.
Single-pulse picking at kHz repetition rates using a Ge plasma switch at the free-electron laser FELBE
Review of Scientific Instruments **86**, 063103 (2015)

132. Shang, Z.; Tan, Y.; Akhmadaliev, Sh.; Zhou, S.; Chen, F.
Cladding-like waveguide structure in Nd:YAG crystal fabricated by multiple ion irradiation for enhanced waveguide lasing
Optics Express **21**, 27612 (2015)

133. Shang, Z.; Tan, Y.; Zhou, S.; Chen, F.
Layer-to-layer compression and enhanced optical properties of few-layer graphene nanosheet induced by ion irradiation
Optical Engineering **55**, 081303 (2015)

134. Shen, X.; Qiu, X.; Su, D.; Zhou, S.; Li, A.; Wu, D.
Thickness-dependent metal-insulator transition in epitaxial $SrRuO_3$ ultrathin films
Journal of Applied Physics **117**, 015307 (2015)

135. Shlyk, L.; Vinnik, D. A.; Zherebtsov, D. A.; Hu, Z.; Kuo, C.-Y.; Chang, C.-F.; Lin, H.-J.; Yang, L.-Y.; Semisalova, A. S.; Perov, N. S.; Langer, T.; Pöttgeng, R.; Nemrava, S.; Niewa, R.
Single crystal growth, structural characteristics and magnetic properties of chromium substituted M-type ferrites
Solid State Sciences **50**, 23 (2015)

136. Smith, T.; Leya, I.; Hofmann, B.; Merchel, S.; Rugel, G.; Pavetich, S.
Exposure and terrestrial age of the Twannberg meteorite based on cosmogenic noble gases and radionuclides
Meteoritics & Planetary Science **50** (S1), A29-A414 (2015)

137. Sorger, C.; Preu, S.; Schmidt, J.; Winnerl, S.; Bludov, Y. V.; Peres, N. M. R.; Vasilevskiy, M. I.; Weber, H. B.
Terahertz response of patterned epitaxial graphene
New Journal of Physics **17**, 053045 (2015)

138. Su, Y.; Falgenhauer, J.; Polity, A.; Leichtweiß, T.; Kronenberger, A.; Obel, J.; Zhou, S.; Schlettwein, D.; Janek, J.; Meyer, B. K.
LiPON Thin Films with High Nitrogen Content for Application in Lithium Batteries and Electrochromic Devices Prepared by RF Magnetron Sputtering
Solid State Ionics **282**, 63 (2015)

139. Suschke, K.; Hübner, R.; Murmu, P. P.; Gupta, P.; Futter, J.; Markwitz, A.
High Energy Radial Deposition of Diamond-Like Carbon Coatings
Coatings **5**, 326 (2015)

140. Tan, Y.; Zhang, H.; Zhao, C.; Akhmadaliev, Sh.; Zhou, S.; Chen, F.
Bi_2Se_3 Q-switched Nd:YAG ceramic waveguide laser
Optics Letters **40**, 637 (2015)

141. Urbassek, H. M.; Bradley, R. M.; Nietiadi, M. L.; Möller, W.
Sputter yield of curved surfaces
Physical Review B **91**, 165418 (2015)

142. van Gastel, R.; Hlawacek, G.; Dutta, S.; Poelsema, B.
Backscattered helium spectroscopy in the helium ion microscope: Principles, resolution and applications
Nuclear Instruments and Methods in Physics Research B **344**, 44 (2015)

143. Veligura, V.; Hlawacek, G.; van Gastel, R.; Zandvliet, H. J. W.; Poelsema, B.
Investigation of ionoluminescence of semiconductor materials using helium ion microscopy
Journal of Luminescence **157**, 321 (2015)

144. Vlcek, M.; Lukác, F.; Vlach, M.; Wagner, S.; Uchida, H.; Baehtz, C.; Shalimov, A.; Pundt, A.; Cízek, J.
Influence of microstructure and mechanical stress on behavior of hydrogen in 500 nm Pd films
Journal of Alloys and Compounds **645**, 446 (2015)

145. Walus, S.; Barchasz, C.; Bouchet, R.; Leprêtre, J.-C.; Colin, J.-F.; Martin, J.-F.; Elkaïm, E.; Bähtz, C.; Alloin, F.
Lithium/Sulfur Batteries Upon Cycling: Structural Modifications and Species Quantification by In Situ and Operando X-Ray Diffraction Spectroscopy
Advanced Engineering Materials **5**, 1500165 (2015)

146. Weichsel, T.; Hartung, U.; Kopte, T.; Zschornack, G.; Kreller, M.; Philipp, A.
A hybrid electron cyclotron resonance metal ion source with integrated sputter magnetron for the production of an intense Al_+ ion beam
Review of Scientific Instruments **86**, 093301 (2015)

147. Wierzchowski, W.; Turos, A.; Wieteska, K.; Stonert, A.; Ratajczak, R.; Jóźwik, P.; Wilhelm, R.; Akhmadaliev, S.; Mazur, K.; Paulmann, C.
Ion implantation of the 4H-SiC epitaxial layers and substrates with 2MeV Se^+ and 1MeV Al^+ ions
X-Ray Spectrometry **44**, 371 (2015)

148. Wittenbrink, I.; Hausmann, A.; Schickle, K.; Lauria, I.; Davtalab, R.; Foss, M.; Keller, A.; Fischer, H.
Low-aspect ratio nanopatterns on bioinert alumina influence the response and morphology of osteoblast-like cells
Biomaterials **62**, 58 (2015)

149. You, Q.; Cai, H.; Gao, K.; Hu, Z.; Guo, S.; Liang, P.; Sun, J.; Xu, N.; Wu, J.
Highly transparent and conductive Al-doped ZnO films synthesized by pulsed laser co-ablation of Zn and Al targets assisted by oxygen plasma
Journal of Alloys and Compounds **626**, 415 (2015)

150. You, Q.; Cai, H.; Hu, Z.; Liang, P.; Prucnal, S.; Zhou, S.; Sun, J.; Xu, N.; Wu, J.
Blue shift in absorption edge and widening of band gap of ZnO by Al doping and Al–N co-doping
Journal of Alloys and Compounds **644**, 528 (2015)

151. Zatsepin, A. F.; Buntov, E. A.-; Mikhailovich, A. P.; Slesarev, A. I.; Schmidt, B.; von Czarnowski, A.; Fitting, H. J.
Relaxation of excited surface states of thin Ge-implanted silica films probed by OSEE spectroscopy
Journal of Luminescence **169**, 143 (2015)

152. Zatsepin, A. F.; Zatsepin, D. A.; Zhidkov, I. S.; Kurmaev, E. Z.; Fitting, H. J.; Schmidt, B.; Mikhailovich, A. P.; Lawniczak-Jablonska, K.
Formation of Ge^0 and GeO_x nanoclusters in Ge^+-implanted SiO_2/Si thin-film heterostructures under rapid thermal annealing
Applied Surface Science **349**, 780 (2015)

Patents

1. Bürger, D.; Du, N.; Schmidt, H.; Skorupa, I.; You, T.
P1505 - Komplementärer Widerstandsschalter
EP15166520.5 - offengelegt am 04.11.2015

2. Facsko, S.; Ou, X.
P1404 - Strukturierungsverfahren
DE102014107458.0 - offengelegt am 03.12.2015; Nachanmeldung: CN

3. Schmidt, H.; Selvaraj, L.; Bogusz, A.; Bürger, D.; Prucnal, S.; Skorupa, I.
P1403 - Kapazitätsdiode, Verfahren zum Herstellen einer Kapazitätsdiode, sowie Speicher und Detektor mit einer solchen Kapazitätsdiode
DE102014105639 - Erteilung 13.01.2015; Nachanmeldung: WO

Concluded scientific degrees

PhD theses

1. Banholzer, A.
   Magnetische Charakterisierung von Vortex-Dreifachlagen mittels Röntgentransmissionsmikroskopie, Magnetowiderstand und ferromagnetischer Resonanz
   TU Dresden, 14.12.2015
2. Endler, R.
   Ionenstrahlgestützte Fasertexturierung und Kornwachstum in polykristallinem Dünnschichtsilizium
   TU Dresden, 13.03.2015
3. Germer, S.
   Design and analysis of integrated optical waveguide structures and their coupling to silicon based light emitters
   TU Dresden, 26.06.2015
4. Osten, J.
   Auswirkung lokaler Ionenimplantation auf Magnetowiderstand, Anisotropie und Magnetisierung
   TU Dresden, 17.12.2015
5. Pavetich, S.
   Determination of non-routine radionuclides by medium-energy accelerator mass spectrometry
   TU Dresden, 06.10.2015
6. Pelic, B.
   Nanoscale surface engineering for improved corrosion resistance of CuZn, PbSn and TiAl alloys
   TU Chemnitz, 27.11.2015
7. Reichel, D.
   Ripple pyrometry during millisecond annealing on shallow boron-doped silicon wafers
   TU BA Freiberg, 06.02.2015
8. Sendler, T.
   Leitwertkontrolle einzelner elektrisch kontaktierter Moleküle
   TU Dresden, 02.10.2015
9. Wang, Y.
   Defect-induced ferromagnetism in SiC
   TU Dresden, 30.01.2015
10. Wündisch, C.
    Das Diffusions- und Aktivierungsverhalten von Arsen und Phosphor in Germanium
    TU Dresden, 19.11.2015
11. Zybell, S.
    Relaxation dynamics in photoexcited semiconductor quantum wells studied by time-resolved photoluminescence
    TU Dresden, 28.08.2015

Master/Diploma theses

1. Andric, S.
   Investigation of Ge nanolayers for low-dimensional electronics
   TU Dresden/KU Leuven, 31.08.2015
2. Hähnel, M.
   Optimierung eines zeitaufgelösten THz-Spektroskopieaufbaus zur Untersuchung von Halbleiternanostrukturen
   TU Dresden, 03.07.2015
3. Hentschel, H.
   Ferromagnetic GaMnP: Co-doping with shallow acceptors
   TU Dresden, 20.08.2015
4. Katkoju, N. K.
   Electrical characterisation of single organic molecules via mechanically controllable break junction
   TU Dresden, 05.08.2015
5. Manjunath, K.
   Investigation of faceted structures induced by ion irradiation
   TU Dresden, 21.07.2015

Appointments and honors

Appointments

1. **Schultheiß, Helmut**
   Leader of the **Emmy Noether Junior Research Group** “Magnonics: Spin waves bridging Spintronics and Photonics” was appointed as **TU Dresden Young Investigator** to the Faculty of Science of the TU Dresden.

Awards and honors

1. **Bakaev, Alexander**
   PostDoc in the division “Structural Materials” won the **First Price** of the 2015 Young Generation Scientific Contest of the Belgian Nuclear Society (BNS), March 26, 2015, Brussels, for his PhD thesis 'Radiation effects in structural steels for nuclear applications: an atomistic study' defended 2014.
2. **Deb, Dipjyoti**
   PhD student in the division “Scaling Phenomena” and fellow of the International Research School NanoNet was invited to the **“Falling Walls 2015“-conference** by the Alexander von Humboldt foundation in Berlin on November 08 – 09, 2015.
   The **1st Prize** at the Science Slam of the 70th United Nations Day celebration in Dresden, Germany (October 23, 2015) was awarded to him for his presentation „Communication“.
   He won a **Cfaed Inspire Grant** by the Center for Advancing Electronics Dresden (cfaed) to collaborate with Prof. Justin Holmes and Dr. Yordan M. Georgiev at Tyndall National Institute, Cork, Ireland on the fabrication of sub-20 nm silicon nanowires in May 2015.
   He received the **2nd Poster Prize** for his contribution "Top-down fabrication and characterization of silicon nanowire FETs" at the IHRS NanoNet Annual Workshop 2015, Berghotel Bastei, Germany, September 30 – October 02, 2015.
   He was awarded the **3rd Prize** at the Science Slam of the Graduate Academy at TU Dresden for his presentation „Transport phenomena simplified“ on July 08, 2015.
   In addition, he received a **DAAD-RISE Grant** to host Ms. Nikol Lambeva, MSc student in physics at the University Birmingham, U.K. in June 2015.
3. **Götze, Tom**
   Master student in the division “Scaling Phenomena” and at TU Chemnitz successfully applied for **DAAD Funding** to attend the DAAD-organized Go East Summer School in Jekaterinburg, Russian Federation, to strengthen the cooperation with Dr. Andrey N. Enyashin, Russian Academy of Sciences, Ural Branch, on electronic properties of nanostructures.
4. **Günther, Florian**
   PhD student in the division “Scaling Phenomena”, fellow of the Center for Advancing Electronics Dresden (cfaed), and member of the International Research School NanoNet acquired an **Cfaed Inspire Grant** by the Center for Advancing Electronics Dresden (cfaed) to collaborate with the group of Prof. Ubirajara Rodrigues Filho at the University Sao Paolo, Campus Sao Carlos, Brazil on molecular dielectrics in October/November 2015.
5. **Kelling, Jeffrey**
   PhD student in the division “Scaling Phenomena” and member of the International Research School NanoNet won an **Erasmus+ Fellowship** to visit the group of Dr. Martin Weigel at the University Coventry, U.K. for cooperative work on the efficient implementation of GPU-based codes from November 2015 to January 2016.
6. **Khalid, Muhammad**
   PostDoc in the Helmholtz Young Investigator Group "Functional Materials" of the division “Semiconductor Materials” received the **Best Poster Prize** for his contribution “Dilute ferromagnetic InMnP“ at the 20th International Conference on Magnetism, Barcelona, Spain, July 05 – 10, 2015.

7. **Lokamani**
PhD student in the division “Scaling Phenomena” and fellow of the International Research School NanoNet successfully applied for a **3-month Travel Grant** by the Graduate Academy of the TU Dresden to cover expenses related to his research stay at the Virtual Institute MEMRIOX partner site ETH Zürich with Prof. N. A. Spaldin from October to December 2015.

8. **Schultheiß, Helmut; Wagner, Kai; Henschke, Andreas; Sebastian, Thomas**
Members of the Emmy Noether Junior Research Group “Magnonics: Spin waves bridging Spintronics and Photonics” received the **HZDR Research Award 2015** for their investigations of generating and detecting reconfigurable spin wave channels.

9. **Schultheiß, Helmut**
Head of of the Emmy Noether Junior Research Group “Magnonics: Spin waves bridging Spintronics and Photonics” was elected as **Treasurer of the German Chapter** and as member of the **Technical Committee** of the **IEEE Magnetics Society**.

10. **Sebastian, Thomas; Schultheiß, Helmut**
Members of the Emmy Noether Junior Research Group “Magnonics: Spin waves bridging Spintronics and Photonics” received a **Helmholtz Enterprise Grant** from the Initiative and Networking Fund of the Helmholtz Association for the development of the spin-off company 'GridLab'.

11. **Teschome, Bezu**
PhD student in the division “Ion beam Center” and fellow of the International Research School NanoNet won the **3rd Poster Prize** for his contribution "Arrangement and characterization of functional DNA origami nanostructures for nanoelectronics" at the IHRS NanoNet Annual Workshop 2015, Berghotel Bastei, Germany, September 30 – October 02, 2015.

12. **Wagner, Kai**
Member of the Emmy Noether Junior Research Group “Magnonics: Spin waves bridging Spintronics and Photonics” obtained the **Ken Hass Outstanding Student-Paper Award** (Runner-up) in recognition of his outstanding research “Magnetic domain walls as reconfigurable spin-wave nano-channels” presented by an invited talk at the American Physical Society (APS) March Meeting 2016 in Baltimore, USA.
In addition, he obtained an **IEEE Travel Grant** for the IEEE Magnetics Society Summer School at Tohoku University, Sendai, Japan in July 2015.

13. **Yuan, Ye**
PhD candidate in the Helmholtz Young Investigator Group "Functional Materials" of the division “Semiconductor Materials” received the **Best Poster Prize**: “Spin-glass behavior of Fe doped InAs prepared by ion implantation and pulsed laser annealing“ at the 20th International Conference on Magnetism, Barcelona, Spain, July 05 – 10, 2015.

14. **Yildirim, Oguz**
PostDoc in the Helmholtz Young Investigator Group "Spintronics” received the **LOT-Quantum Design User Award on Magnetometry** from LOT-QuantumDesign GmbH, Darmstadt, Gertmany on the DPG Spring Meeting 2015, Berlin, Germany.

Invited conference contributions, colloquia, lectures and talks

Invited conference talks

1. Bali, R.; Wintz, S.; Meutzner, F.; Hübner, R.; Boucher, R.; Ünal, A. A.; Valencia, S.; Neudert, A.; Potzger, K.; Bauch, J.; Kronast, F.; Facsko, S.; Lindner, J.; Fassbender, J.
   Ion induced magnetic patterning using chemical disordered induced ferromagnetism
   International Conference on Nanostructuring by Ion Beams, 23.-25.11.2015, Agra, India
2. Berencen, Y.; Braun, M.; Garrido, B.; Hiller, D.; Liu, B.; Ramirez, J. R.; Sun, J.; Wutzler, R.; Helm, M.; Skorupa, W.
   Strong electroluminescence from terbium-doped metal-insulator-semiconductor structures
   Freiberg Silicon Days 2015, 18.-19.06.2015, Freiberg, Germany
3. Bischoff, L.; Böttger, R.; Heinig, K.-H.
   Surface Modification with heavy Mono- and Polyatomic Ions
   The 22nd International Conference on Ion-Surface Interactions (ISI–2015), 20.-24.08.2015, Moscow, Russia
4. Deac, A. M.
   Spin-based nanoelectronic devices for mobile Information-Communication Technology
   SEMICON Europa 2015, 06.-08.10.2015, Dresden, Germany
5. Deac, A. M.
   Spin-Torque Devices Based on MgO-Based Magnetic Tunnel Junctions
   Spin Dynamics in Nanostructures- Nanoscale Spintronics with Magnons, Phonons, and Photons Gordon Research Conference (GRC), 26.-31.07.2015, The Hong Kong University of Science and Technology, China
6. Deac, A. M.
   International research environment and career development
   Spin Dynamics in Nanostructures- Interplay of Spin, Charge and Lattice Dynamics Gordon Research Seminar (GRS), 25.-26.07.2015, The Hong Kong University of Science and Technology, China
7. Deac, A. M.
   Spin-based nanoelectronic devices for mobile Information-Communication Technology
   The 12th Japanese-German Frontiers of Science (JGFoS) Symposium, 01.-04.10.2015, Kyoto, Japan
8. Engler, M.; Michely, T.; Facsko, S.
   Reverse Epitaxy on Elemental Semiconductors
   International Conference on Nanostructuring with Ion Beams (ICNIB2015), 23.-25.11.2015, Agra, India
9. Facsko, S.; Ou, X.; Hübner, R.; Grenzer, J.; Heinig, K.-H.
   Reverse Epitaxy on Semiconductor Surfaces
   8th International Workshop on Nanoscale Pattern Formation at Surfaces, 12.-16.07.2015, Krakow, Poland
10. Facsko, S.; Ou, X.; Wang, X.; Hübner, R.; Grenzer, J.
    Spontaneous pattern formation on ion irradiated semiconductor surfaces
    22nd International Conference on Ion-Surface Interactions, 19.-22.08.2015, Moskow, Russia
11. Facsko, S.; Wilhelm, R. A.; Gruber, E.; Ritter, R.; Heller, R.; Aumayr, F.
    Interaction of Highly Charged Ions with Surfaces and Nanomembranes
    MRS Spring Meeting, 06.-10.04.2015, San Francisco, USA

12. Fassbender, J.
Nanomagnets - created and tailored by ions
Eigth International Meeting on Recent Developments in the Study of Radiation Effects in Matter, 20.-23.09.2015, Kerteminde, Denmark

13. Fassbender, J.
Ion beam technology
High resolution diagnostics and ion beam technology, 01.-02.10.2015, Bratislava, Slovakia

14. Fassbender, J.
European Ion Beam Infrastructures for Materials and Transdisciplinary Research
INARIE - Integrating Access to Pan-European Research Infrastructures in Central and Eastern Europe, 30.11.-02.12.2015, Debrecen, Hungary

15. Heller, R.
Modern Approaches in Ion Beam Analysis - Challenges and ongoing Developments
50th Zakopane School of Physics, 18.-23.05.2015, Zakopane, Poland

16. Hlawacek, G.
Exploiting channelling in Helium Ion Microscopy
EBSD 2015, 30.-31.03.2015, Glasgow, United Kingdom

17. Hlawacek, G.
Helium Ion Microscopy
mmc2015, 29.06.-02.07.2015, Manchester, United Kingdom

18. Hlawacek, G.
High resolution surface patterning with the Helium Ion Microscope
XXII International Conference on Ion-Surface Interactions, 20.-24.08.2015, Moscow, Russia

19. Hlawacek, G.
Materials analysis using channeling and ionoluminescence in a helium ion microscope
IBA2015, 14.-19.06.2015, Opatija, Croatia

20. Hlawacek, G.
Applications of Helium Ion Microscopy
49th Annual Meeting of the Israel Society for Microscopy, 17.-18.05.2015, Bar Ilan, Israel

21. Hlawacek, G.
He-ion Microscopy
Physics boat 2015, 08.06.2015, Helsinki, Finland

22. Hlawacek, G.; Veligura, V.; Jankowski, M.; van Gastel, R.; Wormeester, R.; Zandvliet, H. J. W.; Poelsema, B.
Application of Helium Ion Microscopy to surface science problems
1st International Conference on Applied Surface Science, 27.-30.07.2015, Shanghai, China

23. Hübner, R.
Morphology and Microstructure of Si-SiO_2 Nanocomposite Layers
EFDS-Workshop Morphologie und Mikrostruktur dünner Schichten und deren Beeinflussung, 12.03.2015, Dresden, Germany

24. Kákay, A.; Hertel, R.
Spin Waves going 3D - Chiral Effects in Curved Magnetic Nanowires
International Workshop on Magnetic Nanowires and Nanotubes, 17.-20.05.2015, Meersburg/Lake Constance, Germany

25. Kelling, J.
C++11/14 features relevant in GPGPU APIs
GPU Day 2015 - The Future of Many-Core Computing in Science, 20.-21.05.2015, Budapest, Hungary

26. Kelling, J.; Ódor, G.; Heinig, K.-H.; Gemming, S.
Efficient Large Scale Simulation of Stochastic Lattice Models on GPUs
GPU Day 2015 - The Future of Many-Core Computing in Science, 20.-21.05.2015, Budapest, Hungary

27. Kowalska, E.; Sluka, V.; Fowley, C.; Kákay, A.; Aleksandrov, Y.; Lindner, J. ; Fassbender, J.; Deac, A. M.
Zero-field precession and suppression of the output power due to the bias dependence of the TMR in MgO-based spin-torque oscillators
20th International Conference on Magnetism, 06.-10.07.2015, Barcelona, Spain

28. Posselt, M.; Murali, D.
First-principles calculation of defect free energies: General aspects illustrated in the case of bcc-Fe
MRS 2015 Fall Meeting, Symposium YY: Advanced Atomistic Algorithms in Materials Science, 29.11.-04.12.2015, Boston, USA

29. Potzger, K.
Tuning physical properties by introducing defects: Applications in magnetic data storage and sustainable energy materials
50th Zakopane School of Physics Breaking Frontiers: Submicron Structures in Physics and Biology, 18.-23.05.2015, Zakopane, Poland

30. Prucnal, S.
Millisecond range liquid phase processing of nanowire structures
NATO Advanced Workshop Functional Nanomaterials and Devices for Electronics, Sensors, Energy Harvesting, 13.-16.04.2015, Lviv, Ukraine

31. Redondo-Cubero, A.; Palomares, F. J.; Lorenz, K.; Mücklich, A.; Hübner, R.; Vázquez, L.
Nanoripple patterning under medium energy implantation using metal foreign atoms
2015 MRS Spring Meeting, 06.-10.04.2015, San Francisco, USA

32. Schmidt, B.; Wetzig, K.
Ionenstrahlanalyseverfahren in der Materialforschung
18. Tagung Festkörperanalytik, 06.07.2015, Vienna, Austria

33. Schneider, H.
Terahertz spectroscopy at HZDR
International consortium on terahertz photonics and optoelectronics conference, 16.-17.12.2015, Moscow, Russia

34. Semisalova, A. S.; Rylkov, V. V.; Nikolaev, S. N.; Tugushev, V. V.; Zhou, S.; Potzger, K.; Smekhova, A.; Perov, N.; Granovsky, A.
Making SiMn and TiO_2 ferromagnetic at room temperature
9th International Conference on Magnetic and Superconducting Materials, 01.-03.05.2015, Antalya, Turkey

35. Skorupa, W.
Subsecond thermal processing for nanostructured semiconductors
28th International Conference on Defects in Semiconductors (ICDS 2015), 27.-31.07.2015, Aalto, Finland

36. Skorupa, W.
Thermal processing within milliseconds: semiconductors and beyond
Gettering and Defect Engineering in Semiconductor Technology 2015 - 30 Years of GADEST, 20.-25.09.2015, Erlangen, Germany

37. Skorupa, W.
Subsecond thermal processing for nanomaterials and beyond
NATO Advanced Workshop Functional Nanomaterials and Devices for Electronics, Sensors, Energy Harvesting, 13.-16.04.2015, Lviv, Ukraine

38. Wilhelm, R. A.; Gruber, E.; Kozubek, R.; Smejkal, V.; Schleberger, M.; Facsko, S.; Aumayr, F.
Charge Exchange and Energy Loss of Slow Highly Charged Ions in Graphene
International Workshop on Inelastic Ion-Surface Collisions (IISC), 18.-23.10.2015, San Sebastian, Spain

39. Winnerl, S.
Einblick in die Relaxationsdynamik von Graphen mittels Infrarot-Kurzzeitspektroskopie: Überraschende Coulomb-Streueffekte
26. Edgar Lüscher Seminar 2015, 07.-10.02.2015, Klosters, Switzerland

40. Winnerl, S.
Coulomb scattering in the vicinity of the Dirac point in graphene
International workshop on many-body phenomena in graphene, 26.-27.10.2015, Gothenburg, Sweden

41. Wintz, S.
Topological Spin Textures in Magnetic Multilayers
DPG Frühjahrstagung der Sektion Kondensierte Materie, 15.-20.03.2015, Berlin, Germany

42. Zhou, S.
Application of ion beams to fabricate and tune ferromagnetic semiconductors
2015 E-MRS Fall Meeting, 14.-18.09.2015, Warsaw, Poland

Colloquia

43. Gemming, S.
Microscopic processes in data and energy storage - considerations based on multiscale modeling
Friedrich Schiller University, 23.01.2015, Jena, Germany

44. Facsko, S.; Wilhelm, R.; Gruber, E.; Heller, R.; Aumayr, F.
Pre-equilibrium Dynamics of Highly Charged ions at Surfaces and Carbon Nanomembranes
Colloquium, 12.11.2015, University Leipzig, Germany

45. Fassbender, J.
Nanomagnets - created and tailored by ions
Physics Colloquium, 13.10.2015, University Leipzig, Germany

Lectures and Talks

46. Gemming, S.
Dynamic processes in materials for energy conversion and storage
International Colloquium on the Simulation of Energy Materials, 12.06.2015, Jülich, Germany

47. Gemming, S.
Materialien für morgen: Energieeffiziente Prozesse in der Informationstechnologie
Kolloquium “20 Jahre Helmholtz“, 25.06.2015, Berlin, Germany

48. Helm, M.
THz spectroscopy of solids using a free-electron laser
Shanghai Institute for Applied Physics (SINAP), 10.03.2015, Shanghai, China

49. Kelling, J.; Ódor, G.; Heinig, K.-H.; Gemming, S.
Efficient Large Scale Simulation of Stochastic Lattice Models on GPUs
Seminar Topical Problems TU Chemnitz, 06.05.2015, Chemnitz, Germany

50. Kelling, J.; Ódor, G.; Heinig, K.-H.; Gemming, S.
Efficient Large Scale Simulation of Stochastic Lattice Models on GPUs
Seminar Coventry University, 18.11.2015, Coventry, United Kingdom

51. Krause, M.
New energy materials - concepts, structure formation and in situ analysis
Honory Colloquium for Prof. Hans Kuzmany, 10.09.2015, Vienna, Austria

52. Liu, Y.
Defect-induced magnetism in SiC: The new opportunity in spintronics
Seminar, State University of New York at Buffalo, 13.10.2015, Buffalo, USA

53. Schneider, H.
Terahertz spectroscopy of 0D and 2D semiconductors with a free-electron laser
Seminar, Xi'an University of Technology, 04.05.2015, Xi'an, China

54. Schneider, H.
Terahertz spectroscopy of 0D and 2D semiconductors with a free-electron laser
Seminar, CAEP, 07.05.2015, Mianyang, China

55. Schneider, H.
High-field terahertz spectroscopy at HZDR
Seminar, Institut Saint-Louis (ISL), 18.09.2015, Saint-Louis, France

56. Schumann, E.
Solarenergie und Photovoltaik - Nanostrukturen für mehr Leistungsfähigkeit
Lehrerfortbildung 2015, 13.02.2015, Dresden, Germany

57. Teschome, B.; Facsko, S.; Keller, A.; Kerbusch, J.
Functional DNA origami nanostructures for nanoelectronics and Photonics
Aarhus University, 22.05.2015, Aarhus, Denmark

58. Wilhelm, R. A.; Gruber, E.; Ritter, R.; Heller, R.; Facsko, S.; Aumayr, F.
Interaction of Slow Highly Charged Ions with Ultrathin Membranes
Institut für Angewandte Physik der TU Wien, 20.02.2015, Vienna, Austria

59. Winnerl, S.
Relaxation dynamics in graphene studied by THz radiation from the free-electron laser FELBE
Uni Manchester, 25.11.2015, Manchester, United Kingdom

Conferences, workshops, colloquia and seminars

Organization of conferences and workshops

1. Erbe, A.; Zahn, P.
   IHRS NanoNet Annual Workshop 2015
   30.09. – 02.10.2015, Lohmen, Germany
2. Helm, M.; Schneider, H.; Winnerl, S.; Pashkin, A.
   German THz Conference
   08. – 10.06.2015, Dresden, Germany
3. Krause, M.
   Workshop 'Craft meets research – ECEMP meets craft' ('Handwerk trifft Forschung – ECEMP trifft Handwerk')
   26.11.2015, Dresden, Germany
4. Skorupa, W.
   Workshop 'nanoKlang'
   09.10.2015, Dresden, Germany

Colloquia

1. Bouzerar, Georges
   Institut Lumière Matière, CNRS & Université Lyon, France
   Theory of dilute magnetic semiconductors
   03.12.2015
2. Esquinazi, Pablo D.
   Universität Leipzig
   Graphite and its hidden superconductivity
   30.01.2015
3. Kaindl, Robert
   Lawrence Berkeley National Laboratory, USA
   Tracking electronic dynamics and emergent correlations on ultrashort timescales
   17.07.2015
4. Kawano, Yukio
   Quantum Nanoelectronics Research Center, Department of Physical Electronics, Tokyo Institute of Technology, Japan
   Nanoscale Terahertz sensing and imaging with nanostructured semiconductor and carbon devices
   02.02.2015
5. Krasheninnikov, Arkady
   Aalto University School of Science, Department of Applied Physics, Aalto, Finland
   Native and irradiation-induced defects in two-dimensional materials
   05.03.2015
6. Makarov, Denys
   IFW Dresden
   3D curved architectures: From curvilinear magnetism to biomimetic microelectronics
   04.06.2015
7. Naaman, Ron
   Weizmann Institute of Science, Rehovot, Israel
   A new road to spintronics - The chiral induced spin selectivity (CISS) effect
   26.11.2016

8. Rushforth, Andrew
University of Nottingham, UK
Magnetic nanostructures under strain
03.09.2015

9. Tajmar, Martin
Institut für Luft- und Raumfahrttechnik, TU Dresden
Space propulsion and spin-off applications with highly miniaturized ion sources at TU Dresden
30.04.2015

10. Thomas, Andy
IFW Dresden
Atomic layer deposited HfO_2-based magnetic tunnel junctions
12.11.2015

11. Wang, Yongqiang
Los Alamos National Laboratory, USA
Ion beam materials research in nuclear energy applications
25.06.2015

Seminars

1. Amorim, Teresa
Universidade de Lisboa, Portugal
Science challenges and life
27.11.2015

2. Arstila, Kai
Department of Physics University of Jyväskylä, Finland
Ion beam analysis with low-energy heavy ions
08.07.2015

3. Bauer, Peter
Johannes Kepler Universität Linz, Institut für Experimentalphysik, AOP, Linz, Austria
Quantitative Low Energy Ion Scattering: achievements and challenges
24.11.2015

4. Berencén, Yonder
University Barcelona, Spain
Rare earth- and Si nanostructure-based light emitting devices for integrated photonics
27.04.2015

5. Berkov, Dmitry
General Numerics Research Lab e.V., Jena
Large-scale modern micromagnetic simulations: state of the art and applications to magnetic nanocomposites and spin transfer induced phenomena
03.02.2015

6. Chen, Feng
Shandong University, China
2d materials: applications in ion-beam formed waveguides
20.08.2015

7. Crandles, David
Brock University, St. Catharines, Ontario, Canada
A search for ferromagnetism in $SrTiO_3$
07.05.2015

8. Crandles, David
Brock University, St. Catharines, Ontario, Canada
Infrared spectroscopy of dilute magnetic semiconductors
20.05.2015

9. Croy, Alexander
MPI-PKS Dresden
Nanomechanics and strain engineering in 2D materials
28.01.2015

10. Deldar, Shayan
Universität Kiel
Simultaneous magneto-optical domain observation and magnetoelectric measurement of 2-2 ME composite sensors
04.05.2015

11. Erb, Denise
Deutsches Elektronen-Synchrotron DESY, Hamburg
In-situ x-ray scattering reveals morphology and magnetism in self-assembling nanopatterns
25.02.2015

12. Fröhlich, Katja
Helmholtz-Zentrum Berlin für Materialien und Energie
Direct writing of truly three-dimensional nanostructures for optical applications by focused electron beam induced deposition
16.09.2015

13. Georgiev, Yordan
Tyndall National Institute/University College Cork, Ireland
Top-down fabrication and characterisation of ultrasmall nanostructures and nanodevices
11.02.2015

14. Ghorbani Asl, Mahdi
Department of Materials Science and Metallurgy, University of Cambridge, UK
Electronic transport through two-dimensional transition-metal chalcogenides
02.11.2015

15. Giner, Ignacio
Technical and Macromolecular Chemistry, University of Paderborn
Fundamental understanding of the dissolution behavior of MgO single crystalline surfaces- an in-situ AFM study
23.07.2015

16. Gradzka, Iwona
Poznan University of Technology, Poland
Thin layers of perylene derivatives for optolectronic applications
11.08.2015

17. Haglund, Richard J.
Vanderbilt University, Nashville/Tennessee, USA
New wine in an old bottle: the insulator-to-metal transition in vanadium dioxide
25.11.2015

18. He, Pan
Institute of Physics and Chemistry of Materials of Strasbourg, CNRS, Strasbourg, France
Tuning of spin-orbital coupling and its effect
05.03.2015

19. Hosemann, Peter
Department of Nuclear Engineering, UC Berkeley, USA
Small scale mechanical testing on irradiated and He implanted materials for nuclear application
27.11.2015

20. Hovius, Niels
GFZ Potsdam
Erosion in the earth system
19.02.2015

21. Johannes, Andreas
Institut für Festkörperphysik, Friedrich-Schiller-Universität Jena
High-fluence implantation into nanostructures
27.03.2015

22. Joshi, Purvee
Institute for Plasma Research, Gandhinagar, India
Interplay between energetic ion flux and re-deposition of sputtered atoms during sputter erosion at normal incidence
20.07.2015

23. Kantorovich, Sofia
Fakultät Physik, Universität Wien, Austria
Magnetic colloids in theory and simulations - away from dipolar hard spheres
30.01.2015

24. Khan, Saif A.
Inter-University Accelerator Centre, Aruna Asaf Ali Marg, New Delhi, India
Embedded nanostructures under energetic ion irradiation
13.08.2015

25. Kolesar, Vladimir
Nanocenter Slovakion, Trnava, Slovakia
Magnetic microwires for MEMS applications
28.01.2015

26. Li, Changhui
MPI Halle
Electron pair emission from surfaces upon He^{2+} impact
11.02.2015

27. Lubk, Axel
TU Dresden
Pushing the limits electron tomography: Towards 3D mapping of electric, magnetic fields and chemical composition at atomic resolution
09.06.2015

28. Lukac, Frantisek
Charles University Prague, Czech Republic
Point defects in Fe-Al alloys
06.03.2015

29. Marchetto, Helder
Elmitec GmbH und Fritz-Haber-Institut Berlin
Introduction to Low Energy Electron Microscopy and surface science applications
22.05.2015

30. Mertzig, Robert
CERN, Geneva, Switzerland
Optimization of the REXEBIS charge breeder towards a high compression electron-gun
26.02.2015

31. Ney, Andreas
Johannes Kepler Universität Linz, Abteilung für Festkörperphysik, Linz, Austria
Space and time resolved x-ray detected ferromagnetic resonance
15.12.2015

32. Ojanperä, Ari
Aalto University, Finland
Ehrenfest dynamics and its applications to ion stopping calculations
25.11.2015

33. Queisser, Friedemann
Universität Duisburg-Essen
Giant magneto-photoelectric effect in graphene
30.11.2015

34. Primetzhofer, Daniel
Department of Physics and Astronomy, Uppsala University, Sweden
Time-of-flight medium energy ion scattering (ToF-MEIS) with light and heavy ions: fundamentals and some applications
07.08.2015

35. Raoux, Simone
EMIL/Helmholtz-Zentrum Berlin für Materialien und Energie
Energy Materials in-situ Laboratory (EMIL)
28.08.2015

36. Reinert, Tilo
Ion Beam Modification and Analysis Laboratory, Department of Physics, University of North Texas, Denton, USA
High-throughput PIXE for high-definition elemental imaging
15.12.2015

37. Rode, Karsten
AMBER Centre, Trinity College Dublin, Ireland
Site-specific magnetic properties of zero-moment Mn_2Ru_xGa
04.08.2015

38. Sawicki, Maciej
Institute of Physics, Polish Academy of Sciences, Warsaw, Poland
Interplay between ferromagnetism and localization in (Ga, Mn)As
17.12.2015

39. Scharf, Andreas
Universität Erlangen
Accelerator Mass Spectrometry with the Erlangen EN Tandem
29.05.2015

40. Scherz, Andreas
European XFEL GmbH, Hamburg
Revealing ultrafast spin dynamics on the nanoscale using X-FELs
11.11.2015

41. Schmidt, Marek
Japan Advanced Institute of Science and Technology (JAIST), Nomi, Japan
Fabrication and imaging of graphene-based nanostructures by helium and nitrogen ion beam
18.08.2015

42. Selim, Farida
Department of Physics and Astronomy, Bowling Green State University and Center for Photochemical Sciences, Bowling Green, Ohio, USA
Hydrogen in semiconducting and insulating oxides
06.03.2015

43. Silva, Thomas
National Institute of Standards and Technology (NIST), Physical Measurements Laboratory, Boulder, Colorado, USA
Resolving the controversy of a possible relationship between perpendicular magnetic anisotropy and the magnetic damping parameter
17.04.2015

44. Skeren, Tomas
Czech Technical University Prague, Czech Republic
Ion induced pattern formation on metals
27.02.2015

45. Srivastava, Sanjeev Kumar
Department of Physics, Indian Institute of Technology Kharagpur, India
Exploiting ion beams to synthesize nanostructures and to study microscopic properties of solids
26.11.2015

46. Streubel, Robert
Institute for Integrative Nanosciences, IFW Dresden
Imaging spin textures on curved magnetic surfaces
18.06.2015

47. Velisan, Gihan
CEA Montbéliard, France
Patterning nanoprecipitate dispersion in model substrates by single and simultaneous dual beam ion implantation
28.05.2015

48. Weigel, Martin
Coventry University, UK
Simulating spin models on GPU
13.04.2015

49. Weiss, Christoph
Joint Quantum Centre (JQC) Durham–Newcastle, Dept. of Physics, Durham University, UK
Attractive Bose gases: From quantum reflection to decoherence-induced motion
21.12.2015

50. Woodcock, Thomas G.
IFW Dresden
The influence of atomic-scale microstructural features on the properties of permanent magnets
22.04.2015

51. Zandvliet, Harold
University of Twente, The Netherlands
1D and 2D systems studied by scanning tunneling microscopy
06.10.2015

52. Zhurkin, Evgeny
St. Petersburg Polytechnic University Peter the Great, Russia
Atomistic Metropolis Monte Carlo techniques for modelling microchemistry of dislocation loops in ferritic alloys
18.08.2015

Exchange of researchers

FEL visitors

1. Bordacs, S.
   Budapest University of Technology and Economics, Budapest, Hungary; 08.-13.02.2015, 11.-16.03.2015
2. Bühler, J.
   Universität Konstanz, Konstanz, Germany; 28.04.-04.05.2015
3. Butykai, A.
   Budapest University of Technology and Economics, Budapest, Hungary, 08.-13.02.2015
4. Breitgoff, F.
   Universität Stuttgart, Stuttgart, Germany; 06.-08.08.2015
5. Cloves, S.
   University of Surrey, Guildford, U.K.; 31.07.-03.08.2015
6. Deßmann, N.
   Aerospace Center DLR, Berlin, Germany; 21.-24.02.2015; 15.-18.10.2015
7. Kovalevsky, K.
   Russian Academy of Sciences, Nizhny Novgorod, Russia; 21.02.-24.02.2015
8. *Li, J.*
   University of Surrey, Guildford, U.K.; 27.-30.07.2015
9. Mironov, O.
   University of Warwick, Coventry, U.K.; 22.04.-02.05.2015
10. Morozov, S.
    Russian Academy of Sciences, Nizhny Novgorod, Russia; 22.-30.3.2015
11. Murdin, B.
    University of Surrey, Guildford, U.K.; 13.-15.07.2015
12. Ortolani, M.
    Sapienza Universita' di Roma, Rome, Italy; 02.-06.02.2015
13. Pavlov, S.
    Aerospace Center DLR, Berlin, Germany; 21.-24.02.2015; 16.-18.10.2015
14. Pietka, B.
    Uniwersytet Warszawski, Warszawa, Poland; 26.-02.05.2015
15. Rava, C.
    University of Warwick, Coventry, U.K.; 22.04.-02.05.2015
16. Rechkemmer, Y.
    Universität Stuttgart, Stuttgart, Germany; 06.-08.08.2015
17. Sabbagh, S.
    Università Roma TRE, Rome, Italy; 02.-06.02.2015
18. Schmidt, C.
    Universität Konstanz, Konstanz, Germany; 01.-04.05.2015
19. Seletskiy, D.
    Universität Konstanz, Konstanz, Germany; 28.04.-04.05.15
20. van Slageren, J.
    Universität Stuttgart, Stuttgart, Germany; 06.-08.08.2015
21. Szczytko, J.
    Uniwersytet Warszawski, Warszawa, Poland; 26.-02.05.2015

22. Virgilio, M.
Universita' di Pisa, Pisa, Italy ; 02.-06.02.15

23. Zhukavin, R.
Russian Academy of Sciences, Nizhny Novgorod, Russia; 21.-24.02.2015; 15.-19.10.2015

Other guests

1. Arias, R.
Universidad de Chile, Santiago, Chile; 19.07.-02.08.2015

2. Baghban Khojasteh Mohammadi, N.
Tabriz, Iran; 15.09.-31.12.2015

3. Berencén, Y.
University Barcelona, Spain; 19.04.-31.12.2015

4. Cai, H.
Fudan University, Shanghai, China; 01.01.-08.04.2015

5. Canpolat, C.
Ankara University, Ankara, Turkey; 06.07.-07.09.2015

6. Chatterjee, S.
Indian Institute of Technology, Bhubaneswar, India; 06.06.-05.07.2015

7. Chen, F.
Shandong University, Shandong, China; 18.-25.08.2015

8. Cheng, F.
Beijing Normal University, Beijing, China; 30.08.-31.12.2015

9. Crandles, D.
Brock University, St. Catharines, Canada; 04.-27.05.2015

10. Ek-in, S.
Mahidol University, Bangkok, Thailand; 19.10.-20.12.2015

11. El-Said, A.
Mansoura University, Mansoura, Egypt; 28.05.-15.07.2015

12. Gallardo, R.
Universidad Tecnica Federico Santa Maria, Valparaiso, Chile; 12.07.-08.08.2015

13. Garcia Garcia, C.
Universidad Tecnica Federico Santa Maria, Valparaiso, Chile; 19.-27.07.2015

14. Hilliard, D.
Dublin Institute of Technology, Ireland; 01.02.-31.07.2015

15. Holybee, B.
University of Illinois, Urbana, USA; 17.05.-17.07.2015

16. Jia, J.
Shanghai Jiao Tong University, China; 16.10.-31.12.2015

17. Jia, Q.
SIMIT Shanghai, China; 08.07.-08.09.2015

18. Kim, D.
University Sejong, South Korea; 12.06.-11.07.2015

19. Landeros Silva, P.
Universidad Tecnica Federico Santa Maria, Valparaiso, Chile; 12.-25.07.2015

20. Mesko, M.
Nanocenter Slovakion, Trnava, Slovakia; 16.08.-04.09.2015

21. Mikhalevskiy, V.
Institute on Laser and Information Technologies, Shatura, Russia; 14.-23.12.2015

22. Purvee, J.
    Institute for Plasmaresearch, Gandhinagar, India; 01.06.-31.07.2015
23. Rhie, K.
    Universität Sejong, South Korea; 12.06.-11.07.2015
24. Sorensen, N.
    US Air Force Academy, Colorado, USA; 04.06.-04.07.2015
25. Wang, Y.
    Free University Berlin, Germany; 01.01.-31.12.2015
26. Wu, C.
    University of Chengdu, China; 01.01.-28.02.2015
27. You, T.
    TU Chemnitz, Germany; 08.-14.01.2015
28. Yu, Y.
    Harbin Institute of Technology, China; 12.09.-31.12.2015
29. Zhu, J.
    Shanghai Institute of Technical Physics, China; 01.11.-31.12.2015
30. Zhurkin, E.
    St. Petersburg Polytechnic University, St. Petersburg, Russia; 08.-23.08.2015

Projects

The projects are listed by funding institution and project starting date. In addition, the institute has several bilateral service collaborations with industrial partners and research institutions. These activities are not included in the following overview.

European Projects

1. 06/2012 – 05/2015 European Union EU
CALIPSO – Coordinated access to light sources
Prof. M. Helm Phone: 0351 260 2260 m.helm@hzdr.de

2. 01/2013 – 12/2016 European Union EU
SPRITE – Supporting postgraduate research
Dr. J. v. Borany Phone: 0351 260 3378 j.v.borany@hzdr.de

3. 11/2013 – 10/2017 European Union EU
MatISSE – Materials' Innovations for a Safe and Sustainable nuclear in Europe
Dr. E. Altstadt Phone: 0351 260 2276 e.altstadt@hzdr.de

4. 01/2015 – 12/2018 European Union EU
FRIENDS2 – Engineering of New Durable Solar Surfaces
Prof. S. Gemming Phone: 0351 260 2470 s.gemming@hzdr.de

5. 06/2015 – 05/2016 European Union EU
SlovakION – Supporting of Slovak Ion Beam Centre
Dr. J. v. Borany Phone: 0351 260 3378 j.v.borany@hzdr.de

6. 09/2015 – 08/2019 European Union EU
SOTERIA – Safe Long Term Operation of Light Water Reactors
Dr. E. Altstadt Phone: 0351 260 2276 e.altstadt@hzdr.de

7. 10/2015 – 12/2017 European Union EU
SMaRT (ERC Starting Grant) – Shapeable Magnetoelectronics
Dr. D. Makarov Phone: 0351 260 3273 d.makarov@hzdr.de

Helmholtz Association Projects

1. 03/2011 – 02/2016 Helmholtz–Gemeinschaft HGF
Functional Materials – Helmholtz Young Investigators Group
Dr. Shengqiang Zhou Phone: 0351 260 2484 s.zhou@hzdr.de

2. 07/2011 – 09/2018 Helmholtz–Gemeinschaft HGF
NanoNet – International Helmholtz Research School on Nanoelectronics
Dr. A. Erbe Phone: 0351 260 2366 a.erbe@hzdr.de

3. 10/2011 – 09/2016 Helmholtz–Gemeinschaft HGF
MEMRIOX – Virtual Institute – Memory Effects in Resistive Ion-beam Modified Oxides
Dr. P. Zahn Phone: 0351 260 3121 p.zahn@hzdr.de

4. 02/2012 – 01/2015 Helmholtz–Gemeinschaft HGF
Magnetic TiO_2 – HRJRG–DETI.2 – Helmholtz Russia Joint Research Group
Dr. K. Potzger Phone: 0351 260 3244 k.potzger@hzdr.de

5. 01/2013 – 12/2017 Helmholtz–Gemeinschaft HGF
W3-Professorship TU Chemnitz
Prof. S. Gemming Phone: 0351 260 2470 s.gemming@hzdr.de

6. 01/2014 – 12/2018 Helmholtz–Gemeinschaft HGF
Spintronics – Helmholtz Young Investigators Group
Dr. A.M. Deac Phone: 0351 260 3709 a.deac@hzdr.de

7. 03/2014 – 02/2017 Helmholtz–Gemeinschaft HGF
Functional Materials – HGF Postdoc Dr. Yu Liu
Prof. M. Helm *Phone: 0351 260 2260* *m.helm@hzdr.de*

8. 11/2014 – 10/2017 Helmholtz–Gemeinschaft HGF
Magnetism – HGF Postdoc Dr. K. Schultheiß
Prof. J. Faßbender *Phone: 0351 260 3096* *j.fassbender@hzdr.de*

German Science Foundation Projects

1. 02/2010 – 06/2015 Deutsche Forschungsgemeinschaft DFG
HybMagMat – Hybride magnetic materials
Prof. J. Fassbender *Phone: 0351 260 3096* *j.fassbender@hzdr.de*

2. 09/2010 – 07/2015 Deutsche Forschungsgemeinschaft DFG
TERATOP – Terahertz non–linear detection and quantum optical studies by resonant two–photon transitions in semiconductor quantum wells
Dr. H. Schneider *Phone: 0351 260 2880* *h.schneider@hzdr.de*

3. 11/2010 – 12/2016 Deutsche Forschungsgemeinschaft DFG
Relaxation dynamics in graphene
Dr. S. Winnerl *Phone: 0351 260 3522* *s.winnerl@hzdr.de*

4. 04/2011 – 06/2015 Deutsche Forschungsgemeinschaft DFG
FRUSTPART – Nucleation of spin order in low-dimensional colloidal particle systems
Dr. A. Erbe *Phone: 0351 260 2366* *a.erbe@hzdr.de*

5. 09/2012 – 09/2015 Deutsche Forschungsgemeinschaft DFG
ATOMIX – Atomic mixing in semiconductor layers
Dr. M. Posselt *Phone: 0351 260 3279* *m.posselt@hzdr.de*

6. 01/2013 – 12/2015 Deutsche Forschungsgemeinschaft DFG
MWN – Magnetization dynamics in nanostructures
Dr. J. Lindner *Phone: 0351 260 3221* *j.lindner@hzdr.de*

7. 01/2013 – 10/2017 Deutsche Forschungsgemeinschaft DFG
Cluster of Excellence – Center for Advancing Electronics Dresden (cfaed)
Prof. M. Helm *Phone: 0351 260 2260* *m.helm@hzdr.de*

8. 02/2013 – 01/2016 Deutsche Forschungsgemeinschaft DFG
Nanostructured thermoelectrics
Dr. P. Zahn *Phone: 0351 260 3121* *p.zahn@hzdr.de*

9. 04/2014 – 03/2016 Deutsche Forschungsgemeinschaft DFG
Dynano – Spin wave excitations in periodic nanostructures
Dr. K. Lenz *Phone: 0351 260 2435* *k.lenz@hzdr.de*

10. 05/2014 – 04/2019 Deutsche Forschungsgemeinschaft DFG
Emmy Noether Junior Research Group - Magnonics
Dr. H. Schultheiß *Phone: 0351 260 3243* *h.schultheiss@hzdr.de*

11. 07/2014 – 07/2015 Deutsche Forschungsgemeinschaft DFG
Time-resolved spectroscopy under high pressure
Dr. A. Pashkin *Phone: 0351 260 3287* *o.pashkin@hzdr.de*

12. 11/2014 – 10/2017 Deutsche Forschungsgemeinschaft DFG
Thermal spin-transfer torques
Dr. J. Lindner *Phone: 0351 260 3221* *j.lindner@hzdr.de*
Dr. A.M. Deac *Phone: 0351 260 3709* *a.deac@hzdr.de*

13. 11/2014 – 10/2017 Deutsche Forschungsgemeinschaft DFG
All Optical Switching
Dr. H. Schultheiß *Phone: 0351 260 3243* *h.schultheiss@hzdr.de*

14. 10/2015 – 09/2018 Deutsche Forschungsgemeinschaft DFG
Ferromagnetic Silicon
Dr. Shengqiang Zhou *Phone: 0351 260 2484* *s.zhou@hzdr.de*

Federally Funded Projects

1. 02/2013 – 07/2015 AG Industrieller Forschungseinrichtungen (AiF) BMWi
   CFD – Surface Coating
   Prof. A. Kolitsch Phone: 0351 260 3348 a.kolitsch@hzdr.de
2. 05/2013 – 04/2015 PT Jülich BMWi
   Analytical Ion-Microscope
   Dr. J. v. Borany Phone: 0351 260 3378 j.v.borany@hzdr.de
3. 06/2013 – 05/2015 PT Jülich BMWi
   AIDA – Apparatus for in-situ Defect Analysis
   Dr. K. Potzger Phone: 0351 260 3244 k.potzger@hzdr.de
4. 01/2014 – 06/2017 PT Jülich BMBF
   In-situ TEM
   Prof. J. Fassbender Phone: 0351 260 3096 j.fassbender@hzdr.de
5. 10/2014 – 09/2015 PT Jülich BMWi
   PolCarr – Electrically Polarizable Materials
   Dr. K. Wiesenhütter Phone: 0351 260 2065 k.wiesenhuetter@hzdr.de
6. 10/2014 – 09/2017 PT Jülich BMBF
   InTerFEL – High-Field Spectroscopy in the THz Regime
   Dr. H. Schneider Phone: 0351 260 2065 h.schneider@hzdr.de

Personnel Exchange Projects and Society Chairs

1. 01/2012 – 12/2016 Institute of Electrical and Electronics Engineers IEEE
   Magnetics Society German Chapter Chair
   Prof. J. Fassbender Phone: 0351 260 3096 j.fassbender@hzdr.de
2. 02/2015 – 04/2015 Deutscher Akademischer Austauschdienst DAAD
   Visit of Prof. Kawano
   Dr. S. Winnerl Phone: 0351 260 3522 s.winnerl@hzdr.de
3. 04/2015 – 03/2017 Deutscher Akademischer Austauschdienst DAAD
   Personnel exchange with Chile – ChileConMagnon
   Dr. K. Lenz Phone: 0351 260 2435 k.lenz@hzdr.de
4. 11/2015 – 04/2017 Deutscher Akademischer Austauschdienst DAAD
   Visit of Dr. Zhu
   Prof. M. Helm Phone: 0351 260 2260 m.helm@hzdr.de

Bilateral Projects

1. 07/2012 – 06/2016 Abengoa Research, Seville, Spain Industry
   AR Framework Collaboration
   Prof. S. Gemming Phone: 0351 260 2470 s.gemming@hzdr.de
2. 10/2012 – 12/2016 Carl–Zeiss Microscopy Industry
   Collaboration on analytical ion microscopy
   Dr. J. v. Borany Phone: 0351 260 3378 j.v.borany@hzdr.de
3. 10/2013 – 06/2015 TÜV Süd
   Education and Training CAMBO Bratislava
   Prof. A. Kolitsch Phone: 0351 260 3348 a.kolitsch@hzdr.de
4. 02/2015 – 12/2015 biosaxony e.V.
   Innovation Voucher - PolCarr
   Dr. K. Wiesenhütter Phone: 0351 260 2065 k.wiesenhuetter@hzdr.de

5. 06/2015 – 11/2015 TUD-Energietechnik TUD
Brittle Fracture Safety
Dr. H.–W. Viehrig *Phone: 0351 260 3246* *h.w.viehrig@hzdr.de*

6. 07/2015 – 09/2015 Industry
Flash Lamp Annealing
Dr. W. Skorupa *Phone: 0351 260 3612* *w.skorupa@hzdr.de*

7. 11/2015 – 06/2017 TU Hamburg-Harburg
ZETA Membrane
Dr. J. v. Borany *Phone: 0351 260 3378* *j.v.borany@hzdr.de*

8. 11/2015 – 01/2016 Industry
Ion Beam Analysis
Dr. J. v. Borany *Phone: 0351 260 3378* *j.v.borany@hzdr.de*

Doctoral training programme

International Helmholtz Research School NANONET

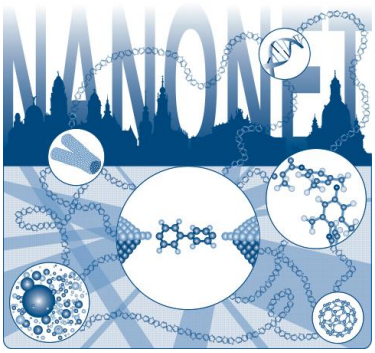

The Institute of Ion Beam Physics and Materials Research is coordinating the International Helmholtz Research School for Nanoelectronic Networks (IHRS NANONET) supported by the Initiative and Networking Fund of the Helmholtz Association. The project started in October 2012. The total funding is 1.2 Mio. € for a period of six years.

The IHRS NANONET is an international, interdisciplinary and thematically focused doctoral programme in the field of molecular electronics. The research school aims at attracting and promoting excellence by educating promising doctoral candidates with backgrounds in physics, chemistry, materials science and electrical engineering. During a period of three years PhD candidates benefit from well-structured, comprehensive training curricula and multiple mentorship, while performing cutting edge research projects within one of the 14 NANONET research groups. Under the supervision of outstanding scientists leading the field of nanoelectronics, the doctoral candidates have the unique opportunity to contribute to the advancement of molecular electronics by developing strategies for the integration of single nano-sized building blocks into large interconnected networks.

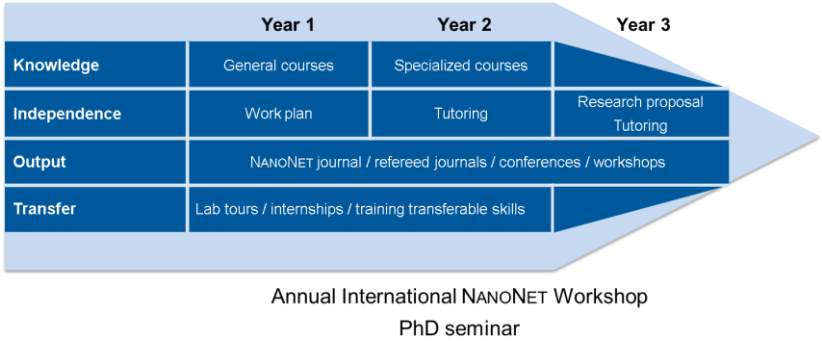

The period of doctoral studies is crucial in the academic career of young scientists. Therefore, the IHRS NANONET fosters not only professional qualification but also personal development by equipping young graduates with competencies for successful careers in a wide variety of positions in academia and industry. The training programme invests on professional competencies, such as the capability to work across disciplines and cultures by promoting networking and the exchange of ideas and knowledge with fellows, mentors and collaboration partners. The cooperation with international scientific and industrial partners complements and broadens the expertise of the IHRS NANONET by establishing a unique research and training network for its doctoral candidates.

The consortium

- Helmholtz-Zentrum Dresden-Rossendorf (HZDR)
- Technische Universität (TU) Dresden
- Leibniz Institute of Polymer Research (IPF) Dresden
- Fraunhofer Institute for Ceramic Technologies and Systems (IKTS) Dresden
- Nanoelectronic Materials Laboratory (NaMLab) gGmbH Dresden

For further information please contact the NANONET coordinator, Dr. Peter Zahn (nanonet@hzdr.de) or visit the IHRS NANONET website: www.ihrs-nanonet.de

Experimental equipment

Accelerators, ion implanters and ion-assisted-deposition

Van de Graaff Accelerator (VdG)	2 MV	*TuR Dresden, DE*
Tandetron Accelerator (T1)	3 MV	*HVEE, NL*
Tandetron Accelerator (T2)	6 MV	*HVEE, NL*
Low-Energy Ion Implanter	0.1 – 40 kV	*Danfysik, DK*
High-Current Ion Implanter	20 – 200 kV	*Danfysik, DK*
High-Energy Ion Implanter	20 – 500 kV	*HVEE, NL*
Plasma Immersion Ion Implantation	5 – 30 kV	*GBR, DE / Home-built*
Focused Ion Beam (15 nm, variable ions)	10 – 30 keV >10 A/cm^2	*Orsay Physics, FR*
Helium/Neon Ion Microscope (HIM)	10 – 35 kV	*Carl Zeiss, DE*
Highly-Charged Ion Facility	25 eV – 25 keV × Q Q = 1 … 40 (Xe)	*Home-built*
High-Power Impulse Magnetron Sputtering		*Melec, DE*
Ion-Beam Sputtering	200 – 2000 V	*Home-built*
UHV Ion Irradiation (Ar, He, etc.)	0 – 5 kV Scan 10×10 mm^2	*Cremer, DE; VG, USA*

Ion beam analysis (IBA)

A wide variety of advanced IBA techniques are available at the MV accelerators (see figure).

RBS	Rutherford Backscattering Spectrometry	(1), (10), (11), (12)	*VdG, T1, T2, HIM*
RBS/C	RBS + Channelling	(1), (11), (12)	*VdG, T1, T2*
HR-RBS	High-Resolution RBS	(10), (14)	*T1*
ERDA	Elastic Recoil Detection Analysis	(1), (4)	*VdG, T2*
PIXE	Particle-Induced X-ray Emission	(1), (5), (6), (12)	*VdG, T1, T2*
PIGE	Particle-Induced γ Emission	(6), (12)	*T1, T2*
NRA	Nuclear Reaction Analysis	(3), (7), (11), (12)	*T1, T2*
NRRA	Nuclear Resonance Reaction Analysis	(3), (7), (11)	*T1, T2*
NMP	Nuclear Microprobe	(12)	*T1*
AMS	Accelerator Mass Spectrometry (focused to long-lived radionuclides: ^{10}Be, ^{26}Al, ^{36}Cl, ^{41}Ca, ^{129}I)	(15)	*T2*

Some stations are equipped with additional process facilities enabling *in-situ* IBA investigations during ion irradiation, sputtering, deposition, annealing etc.

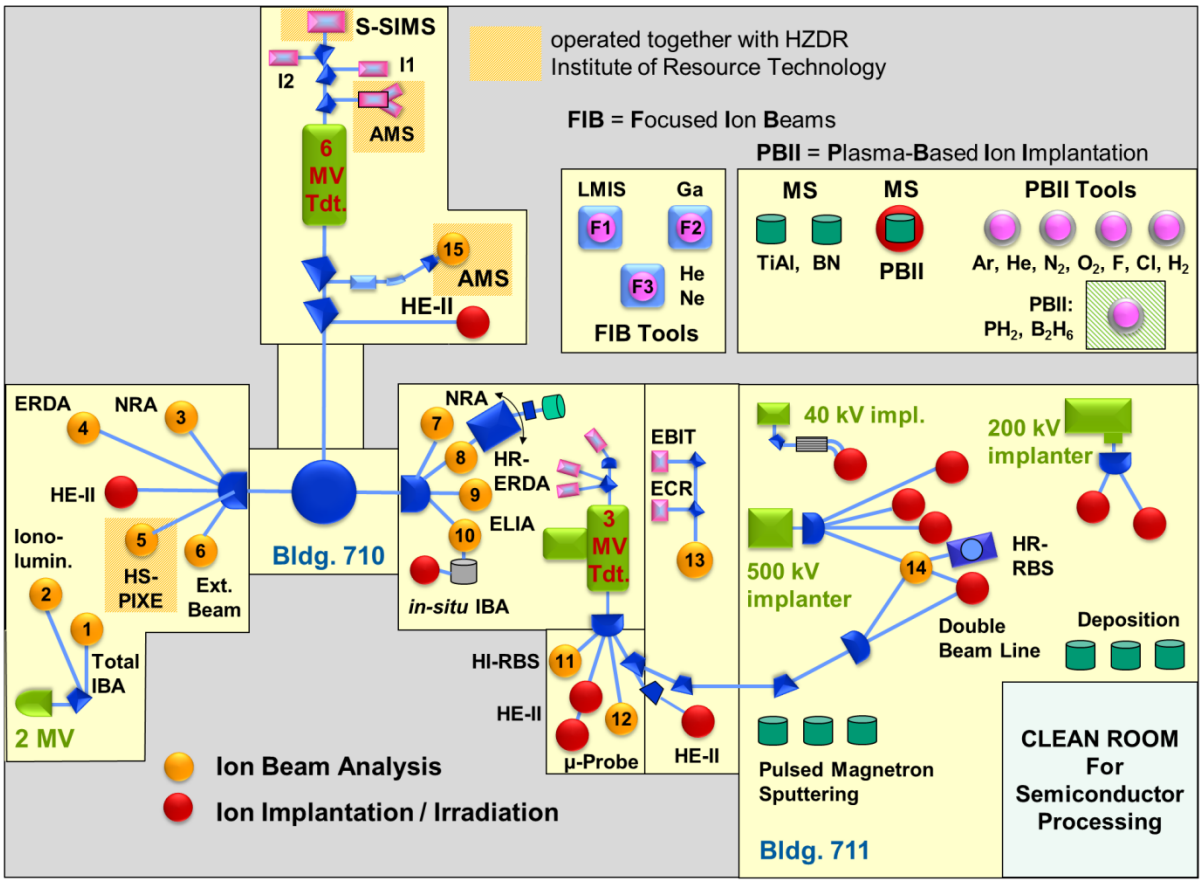

Schematic overview of the HZDR Ion Beam Center

Other particle-based analytical techniques

SEM	Scanning Electron Microscope (S4800 II)	1 – 30 keV + EDX	*Hitachi, JP*
TEM	Transmission Electron Microscope (Titan 80-300 with Image Corrector)	80 – 300 keV + EDX, +EELS	*FEI, NL*
	Transmission Electron Microscope (Talos F200X)	20 – 200 keV + SuperX EDS	*FEI, NL*
SIM	Scanning Ion Microscope (ORION NanoFab with He, Ne ions)	10 – 35 keV + GIS, Patterning	*Zeiss Microscopy, DE*
FIB/SEM	Focused Ion/Electron Cross Beam (NVision 40 with Elphy Plus Litho)	0.5 – 30 keV + EDX, EBSD	*Zeiss Microscopy, DE*
AES	Auger Electron Spectroscopy	+ XPS	*Thermo Fisher Scientific, UK*
CEMS	Mössbauer Spectroscopy	^{57}Fe source	*Home-built*
PAS	Positron Annihilation Spectroscopy	^{22}Na source 30 eV – 36 keV	*Home-built*

Photon-based analytical techniques

XRD/XRR	X-Ray Diffractometer	Cu-Kα	
	θ-θ Powder D8		Bruker, DE
	θ-2θ 4-Circle D5005		Siemens, DE
	θ-θ 4-Circle Empyrean		PANalytical, NL
	θ-2θ 4+2-Circle SEIFERT XRD3003-HR		General Electric, US
SE	Spectroscopic Ellipsometry	250 – 1700 nm	*Woollam, US*
UV-Vis	Solid Spec 3700 DUV	190 – 3300 nm	*Shimadzu, JP*
FTIR	Fourier-Transform Infrared Spectrometer	600 – 7000 cm^{-1}	*Nicolet, US*
FTIR	Fourier-Transform Infrared Spectrometer	50 – 15000 cm^{-1}	*Bruker, DE*
	Ti:Sapphire Femtosecond Laser	78 MHz	*Spectra Physics, US*
	Femtosecond Optical Parametric Osci.		*APE, DE*
	Ti:Sapphire Femtosecond Amplifier	1 kHz	*Coherent, US*
	Ti:Sapphire Femtosecond Amplifier	250 kHz	*Coherent, US*
	Femtosecond Optical Parametric Amplifier		*Light Conversion, LT*
THz-TDS	Terahertz Time-Domain Spectroscopy	0.1 – 4 THz	*Home-built*
Raman	Raman Spectroscopy	> 45 cm^{-1}	*Jobin-Yvon-Horiba, FR*
	In-situ Raman Spectroscopy	> 100 cm^{-1}	*Jobin-Yvon-Horiba, FR*
PL	Photoluminescence (10-300 K)	300 – 1600 nm	*Jobin-Yvon-Horiba, FR*
TRPL	Time-Resolved Photoluminescence	τ = 3 ps – 2 ns τ > 5 ns	*Hamamatsu Phot., JP* *Stanford Research, US*
EL	Electroluminescence	300 – 1600 nm	*Jobin-Yvon-Horiba, FR*
	Optical Split-Coil Supercond. Magnet	7 T	*Oxford Instr., UK*
PR	Photomodulated Reflectivity	300 – 1600 nm	*Jobin-Yvon-Horiba, FR*
PLE	Photoluminescence Excitation	300 – 1600 nm	*Jobin-Yvon-Horiba, FR*
OES	Optical Emission Spectroscopy	250 – 800 nm	*Jobin-Yvon-Horiba, FR*

Magnetic thin film deposition and analysis

PLD	Pulsed Laser Deposition		*SURFACE, DE*
MFM	Magnetic Force Microscope	~ 50 nm resol.	*VEECO / DI, US*
SQUID MPSM	Supercond. Quantum Interference Device	± 7 T	*Quantum Design, US*
SQUID VSM	Vibrating Sample Magnetometer	± 7 T	*Quantum Design, US*
MOKE	Magneto-Optic Kerr Effect (in-plane)	± 0.35 T	*Home-built*
MOKE	Magneto-Optic Kerr Effect (perpend.)	± 2 T	*Home-built*
FR-MOKE	Frequency-resolved Magneto-Optic KE	± 1.1 T	*Home-built*
SKM	Scanning Kerr Microscope		*Home-built*
	Kerr Microscope		*Evico Magnetics, DE*
TR-MOKE	Time-Resolved MOKE (Pump-Probe)		*Home-built*
VNA-FMR	Vector Network Analyzer Ferromagnetic Resonance		*Agilent, DE / Home-built*
ME	Magnetoellipsometer		*LOT, DE; AMAC, US*

Other analytical and measuring techniques

STM/AFM	UHV Scanning Probe Microscope (variable T)		*Omicron, DE*
AFM	Atomic Force Microscope (Contact, Tapping, Spreading)		*Bruker, US*
AFM	Atomic Force Microscope (with c-AFM, SCM-Module)		*Bruker, US*
	Dektak Surface Profilometer		*Bruker, US*
	Micro Indenter/Scratch Tester		*Shimatsu, JP*
MS	Mass Spectrometers (EQP-300, HPR-30)		*HIDEN, DE & US*
	Wear Tester (pin-on disc)		*Home-built*
LP	Automated Langmuir Probe		*Impedans, IE*
HE	Hall Effect Equipment	2 – 400 K, ≤ 9 T	*LakeShore, US*
RS	Sheet-Rho-Scanner		*AIT, South Korea*
DLTS	Deep Level Transient Spectroscopy	+ I-U/C-V 10 - 300 K, 1 MHz	*PhysTech, DE*
IV / CV	Photocapacitance (+I-V/G-V)	250 – 2500 nm	*Home-built*
IV / CV	I-V and C-V Analyzer		*Keithley, US*
IV / CV	I-V and C-V Semi-Automatic Prober	-60 – 300 °C	*Süss, DE; Keithley, US*
IV	I-V Prober	4.2 – 600 K	*LakeShore, Agilent, US*

Deposition and processing techniques

Physical Deposition	Sputtering DC/RF, Evaporation	*Nordiko, UK*
	Electron Beam Evaporation System	*Leybold Optics, DE*
	Thermal Evaporation	*Bal-Tec, LI*
Molecular Beam Epitaxy	III-V semiconductors	*Riber, FR*
Chemical Vapour Deposition	Plasma Enhanced CVD (for a-Si, a-Ge, SiO_2, SiON, Si_3N_4)	*Oxford Instr., UK*
Atomic Layer Deposition	Al_2O_3, HfO_2, SiO_2	*Ultratech, US*
Dry Etching	ICP-RIE, CF_4, SF_6, C_4F_8	*Sentech, DE*
	RIBE, ∅ 6”, Ar, CF_4	*Roth & Rau, DE*
Etching/Cleaning	incl. Anisotropic Selective KOH Etching	
Photolithography	Mask-Aligner, 2 µm-level	*Süss, DE*
Electron Beam Lithography	Raith 150-TWO: ∅ 6”, 10 nm res.	*Raith, DE*
	e-Line Plus: ∅ 4”, 10 nm res.	*Raith, DE*
Thermal Treatment	Room Temperature – 2000°C	
Furnace		*InnoTherm, DE*
Rapid Thermal Annealing (JETFIRST100)		*JIPELEC, FR*
Flash-Lamp Units (0.5 – 20 ms)		*Home-built; FHR, DTF, DE*
RF Heating (Vacuum)		*JIPELEC, FR*
Laser annealing (CW, 808 nm, 450 W)		*LIMO, DE*
Laser annealing (30 ns pulse,10 Hz, 308 nm, 500 mJ)		*COHERENT, USA*
Bonding Techniques	Ultrasonic Wire Bonding	*Kulicke & Soffa, US*
Cutting, Grinding, Polishing		*Bühler, DE*
TEM Sample Preparation	Plan View and Cross Section incl. Ion Milling Equipment	*Gatan, US*

Hot cells laboratory

Mechanical testing of neutron irradiated structural materials	max. total activity 5 TBq (Co-60), -150 ... +315 °C	
Fracture mechanics testing	Max. load ±50 kN	MTS, US
Charpy impact testing	300 J	WPM Leipzig, DE
Small punch test	10 kN	Hegewald & Peschke, DE
Specimen preparation	Electrical discharge machining	AGIE, DE
Depth sensing nanoindentation/ AFM	UNAT, load range 1 – 500 mN	ASMEC, DE

User facilities and services

Ion Beam Center (IBC)

The Ion Beam Center (IBC) at HZDR combines various machines (electrostatic accelerators, ion implanters, plasma-based equipment) into a unique facility primarily used for ion beam modification and ion beam analysis of materials. The available energy range spans from a few eV to almost 100 MeV with a respective interaction depth in solids between 0.1 nm to 10 µm. In addition to standard broad beams also focused (down to 1 nm) and highly-charged (charge state up to +45) ion beams are provided. In addition to these ion beam facilities, structural analysis (electron microscopy and spectroscopy, X-ray scattering techniques) and sample or device processing under clean-room conditions can be utilized at IBC to deliver a “complete” user service. A schematic overview of the IBC including the description of the main beam lines and experimental stations is given at page 92 of this Annual Report. In 2015 about 13.300 beam time hours were delivered to 480 users from 25 countries worldwide performing experiments at IBC or using the capabilities for ion beam services.

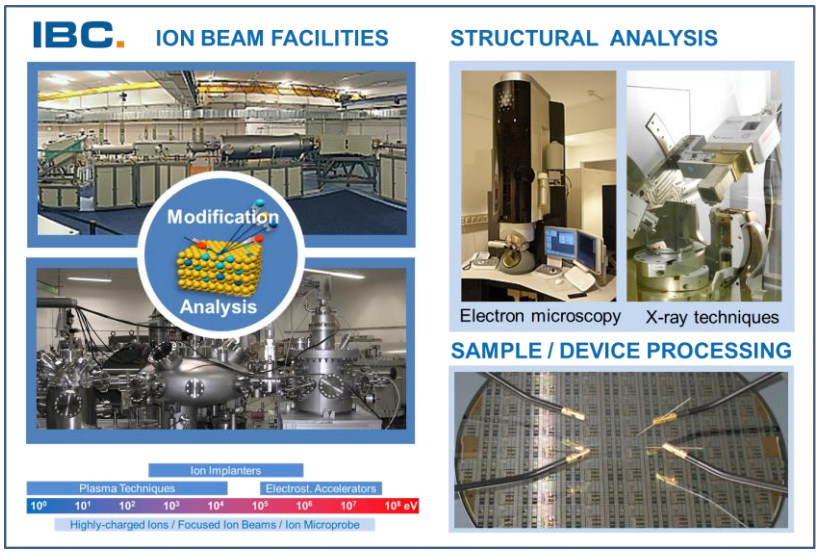

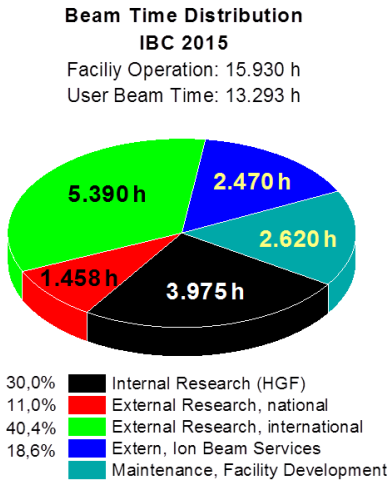

After HZDR joined the Helmholtz Association in 2011, IBC activities have been integrated efficiently into various Helmholtz programmes within the research field “Matter”, but also in the Helmholtz cross-programme activities “Mineral Resources”, “Helmholtz Climate Initiative” and “Materials Research for Energy Technologies”. From the beginning of 2015 the IBC has the status of a Helmholtz LK-II User Facility. Moreover, from 2013 the IBC has been recognized as a large-scale facility within the “BMBF Verbundforschung” programme promoting long-term collaborations with universities.

The IBC demonstrates its outstanding status in relation to other international ion beam facilities by the following features:

- The IBC has provided ion beam technology as a user and competence centre for ion beam applications for more than 30 years. With respect to user beam time hours the IBC is internationally leading and has been supported by numerous national and European grants and by industry.
- IBC activities cover both ion beam modification as well as ion beam analysis (IBA). Experienced staff is present to support IBC users and to enhance the experimental capabilities to their needs.

- Operation of IBC is accompanied by a strong in-house research at the affiliated host institute, both in experiment and theory. This allows in-depth research in targeted research areas as well as the exploration of new application fields for ion beam technology.

Following the rules of a European and national user facility, access for scientific experiments to IBC is provided on the basis of a proposal procedure (www.hzdr.de/IBC) via the common HZDR user facility portal **HZDR-GATE** (gate.hzdr.de). Due to the availability of multiple machines and versatile instrumentation, continuous submission of IBC proposals can be offered (no deadline). The scientific quality of the proposals is steadily evaluated and ranked by an external international User Selection Panel (USP). For successfully evaluated proposals, users get free access to IBC facilities for their experiments which can be often realized within three months after proposal submission. The use of the IBC facilities includes the scientific and technical support during planning, execution and subsequent evaluation of the experiments.

The IBC has a strong background in the commercial exploitation of ion beam technology with partners from industry which is essential for materials science applications. For ion beam services the HZDR Innovation GmbH (spin-off of the HZDR) – www.hzdr-innovation.de – provides a direct and fast access to the IBC facilities based on individual contracts. The close collaboration between IBC and HZDR Innovation GmbH is considered as a reference model aiming to develop innovative strategies for an effective contribution of Helmholtz large-scale facilities for economic innovation. Currently, about 20% of the total IBC beam time is used for commercial ion beam services.

The IBC pursues two strategic objectives for further development. On one hand, it is focused on the successful operation as an international user facility to sustain its position as a leading European ion beam center in the fields of materials and interdisciplinary research. This requires the continuous development and extension of ion beam technologies. Special emphasis is directed towards new R&D areas and communities which so far have not been aware of the advantages of ion technology. On the other hand, cutting edge scientific challenges, in particular for the modification and understanding of the function of materials at the nano-scale down to the atomic level, is addressed in order to achieve new functionalities and to design novel materials. These challenges comprise:

- the extended application of low-energy ions for modification and analysis of ultra-thin films, surfaces, 2D materials and molecular layers based on a new **L**ow **E**nergy **I**on **N**ano-**E**ngineering **F**acility (LEINEF) platform which is currently designed for first experiments in 2017,
- the investigation of material states and modifications far from equilibrium induced by high-energy density excitations with cluster and highly-charged ions,
- the exploration of new IBA approaches with unprecedented lateral resolution, ultimate detection limit and high sample throughput, e.g. for resource technology. In this context, a fruitful and close collaboration between the IBC and the Helmholtz Institute of Resource Technology (www.hzdr.de/fwg) has been developed during last years. With projects like “High-Speed-PIXE” and “Super-SIMS”, the interdisciplinary work of IBC will be substantially extended towards the application of ion beam analysis methods in geosciences and resource technology.

Recently, some new ion beam tools or end-stations have been commissioned which will attract new users by cutting-edge experimental instrumentation. In 2015, the routine operation of the ion microscope *ORION NanoFab* (He/Ne ions, 10 – 40 keV) has started enabling unique possibilities for surface imaging and nano-fabrication with feature sizes below 10 nm. Moreover, based on ion scattering technique, quantitative elemental analysis of surfaces with a spatial resolution of 50 nm became possible at *ORION NanoFab.* As another example, the nuclear reaction analysis end-station has been completed with a retarding field optics which allows fast hydrogen depth profiling measurements.

For more detailed information please contact Dr. Johannes von Borany (j.v.borany@hzdr.de) or Dr. Stefan Facsko (s.facsko@hzdr.de) and visit the IBC webpage: www.hzdr.de/IBC.

Free Electron Laser FELBE

ELBE is an acronym for the free-electron laser (FEL) at the Electron Linear accelerator with high Brilliance and low Emittance (ELBE) located at the Helmholtz-Zentrum Dresden-Rossendorf, Germany. The heart of ELBE is a superconducting linear accelerator operating in cw mode with a pulse repetition rate of 13 MHz. The electron beam (40 MeV, 1 mA max.) is guided to several laboratories where secondary beams (particle and electromagnetic) are generated. Two free-electron lasers (U27-FEL and U100-FEL) produce intense, coherent electromagnetic radiation in the mid and far infrared, which is tunable over a wide wavelength range (4 – 250 µm) by changing the electron energy or the undulator magnetic field. Main parameters of the infrared radiation produced by FELBE are as follows:

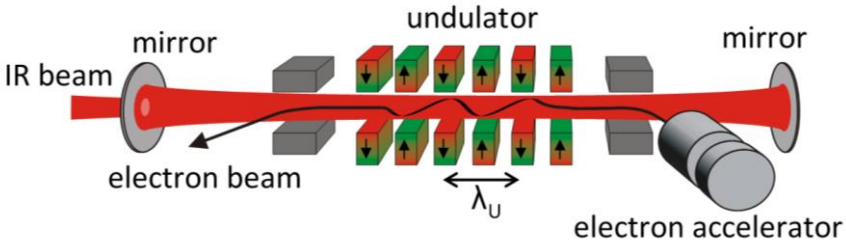

Wavelength λ	4 – 22 µm 18 – 250 µm	FEL with undulator U27 FEL with undulator U100
Pulse energy	0.01 – 2 µJ	depends on wavelength
Pulse length	1 – 25 ps	depends on wavelength
Repetition rate	13 MHz	3 modes: • cw • macropulsed (> 100 µs, < 25 Hz) • single pulsed (Hz … kHz)

The free electron laser is a user facility. Applications for beam time can be submitted twice a year, typically by April 15 and October 15. Users from EU countries have been able to receive support through the FP7 Integrated Infrastructure Initiative (I3) CALIPSO (**C**oordinated **A**ccess to **LI**ghtsources to **P**romote **S**tandards and **O**ptimization), which ended in May 2015.

Typical applications are picosecond pump-probe spectroscopy (also in combination with several other femtosecond lasers, which are synchronized to the FEL), near-field microscopy and nonlinear optics. The FELBE facility also serves as a far-infrared source for experiments at the High-Field Laboratory Dresden (HLD) involving pulsed magnetic fields up to 70 Tesla.

The statistics shows that the FEL used 1024 hours beam time of the ELBE accelerator. This corresponds to 20 % of total beam time, which is again distributed among internal and external users.

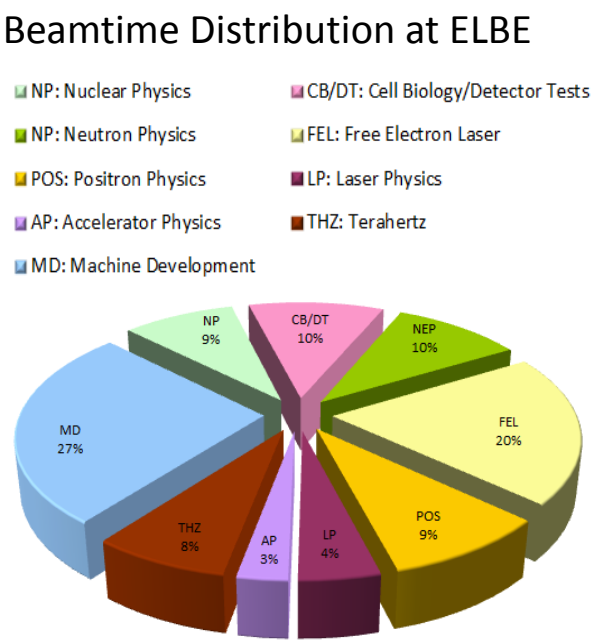

For further information please contact:
Prof. Manfred Helm (m.helm@hzdr.de)
or visit the FELBE webpage
www.hzdr.de/FELBE.

Organization chart

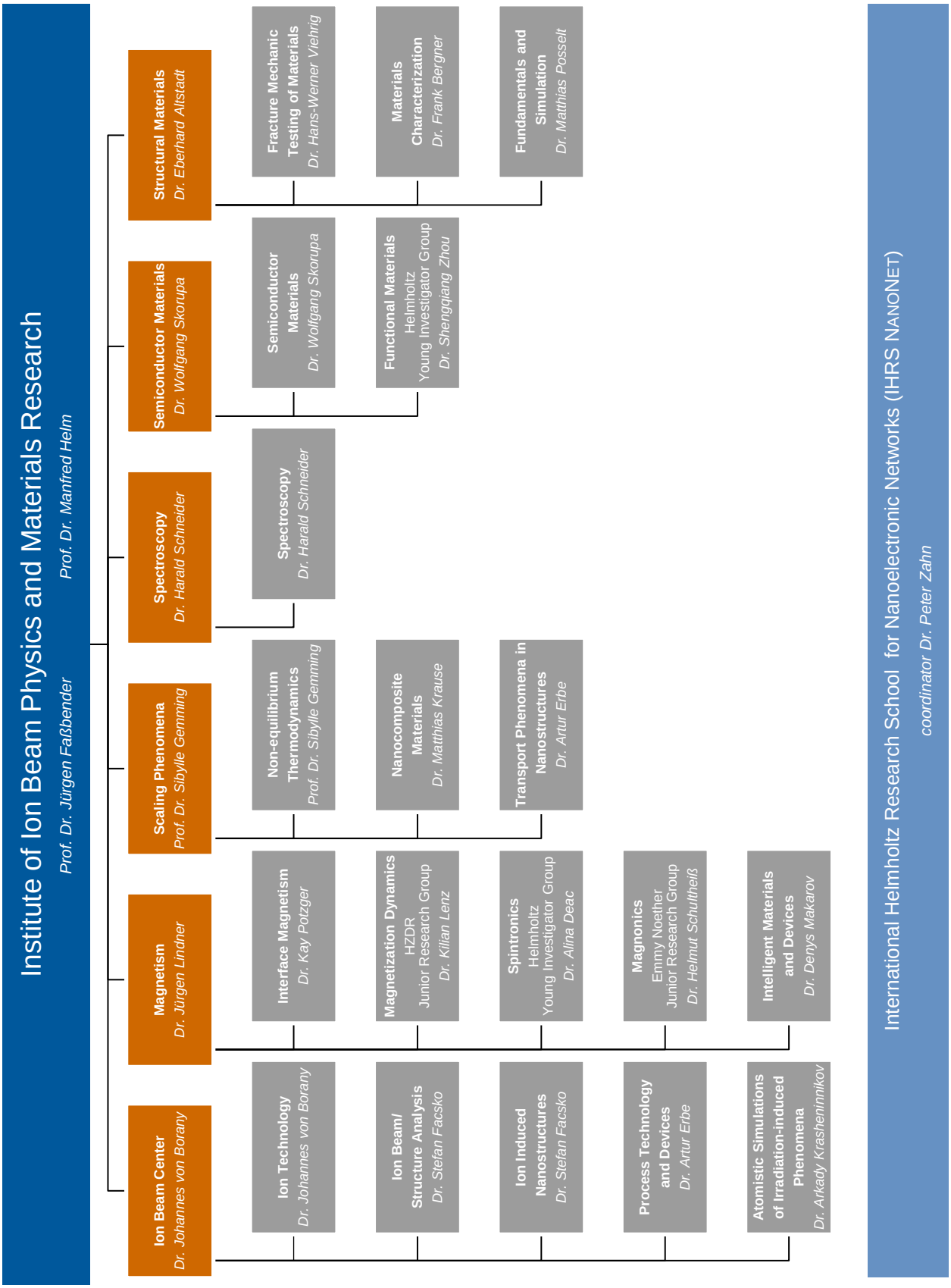

List of personnel 2015

DIRECTORS	OFFICE
Prof. Dr. M. Helm, Prof. Dr. J. Faßbender	S. Gebel, S. Kirch

SCIENTIFIC STAFF

Permanent staff

Dr. C. Akhmadaliev
Dr. E. Altstadt
Dr. C. Bähtz
Dr. F. Bergner
Dr. L. Bischoff
Dr. J. von Borany
Dr. E. Dimakis
Dr. A. Erbe
Dr. S. Facsko
Prof. Dr. S. Gemming
Dr. J. Grenzer
Dr. V. Heera
Dr. R. Hübner
Dr. M. Krause
Dr. J. Lindner
Dr. G. Müller
Dr. F. Munnik
Dr. C. Neelmeijer
Dr. M. Posselt
Dr. K. Potzger
Dr. L. Rebohle
Dr. H. Schneider
Dr. W. Skorupa
Dr. A. Ulbricht
Dr. H.-W. Viehrig
Dr. M. Voelskow
Dr. M. Werner
Dr. S. Winnerl
Dr. P. Zahn
Dr. S. Zhou

Non-permanent

Dr. A. Bakaev (P)
Dr. R. Bali
Dr. R. Böttger
Dr. V. Cantelli
Dr. S. Cornelius (P)
Dr. A. Deac
Dr. M. Devaraj (P)
Dr. M. Engler
Dr. J. Fiedler (P)
Dr. C. Fowley
Dr. Y. Georgiev
Dr. K.-H. Heinig
Dr. C. Heintze
Dr. R. Heller
Dr. G. Hlawacek (P)
M. Houska (P)
Dr. E. Josten
Dr. A. Kákay
Dr. J. Kerbusch (P)
Dr. M. Khalid (P)
Prof. Dr. A. Kolitsch (P)
T. Kosub
Dr. A. Krasheninnikov
Dr. K. Lenz
Dr. K. Li (P)
Dr. B. Liedke (P)
Dr. Y. Liu (P)
Dr. D. Makarov
Dr. P. Pandey (P)
Dr. A. Pashkin
Dr. S. Prucnal
Dr. R. Rana
Dr. A. Scharf
Dr. H. Schultheiß (P)
Dr. K. Schultheiß (P)
Dr. T. Sebastian (P)
Dr. A. Semisalova
Dr. A. Singh
Dr. S. Stienen (P)
Dr. K. Wiesenhütter (P)
Dr. R. Wilhelm
Dr. S. Wintz
Dr. R. Yankov (P)

TECHNICAL STAFF

Permanent staff

Rb. Aniol
Ry. Aniol
E. Christalle
S. Eisenwinder
B. Gebauer
H. Gude
D. Hanf
J. Haufe
A. Henschke
H. Hilliges
S. Klare
J. Kreher
A. Kunz
H. Lange
U. Lucchesi
F. Ludewig
R. Mester
M. Mißbach
Dr. R. Narkovic
C. Neisser
F. Nierobisch
J. Pietzsch
T. Putzke
A. Reichel
H. Richter
M. Roßner
S. Rott
B. Scheumann
G. Schnabel
A. Schneider
A. Scholz
T. Schumann
I. Skorupa
U. Skorupa
M. Steinert
A. Thiel
K. Thiemig
A. Vetter
J. Wagner
W. Webersinke
R. Weidauer
A. Weise
R. Weiss
J. Winkelmann
I. Winkler
L. Zimmermann
J. Zscharschuch

Non-permanent

T. Schönherr (P)
A. Weißig (P)

(P) Projects

PhD STUDENTS

Y. Aleksandrov
H. Arora
A. W. Awan
L. Balaghi
D. Blaschke
J. Braun
A. Bogusz
J. Buchriegler
H. Cansever
A. Das
D. Deb
B. Duan
J. Ehrler
F. Eßer
M. Fehrenbacher
C. Franke
F. Fuchs
K. Gao
F. Günther
A. Heidarian
I. Hilger
D. Janke
J. Kelling
N. Klingner
J. König-Otto
E. Kowalska
D. Lang
M. Langer
F. Liu
F. Lungwitz
J. Osten
B. Pelic
J. Schmidt
E. Schumann
T. Sendler
G. Steinbach
D. Stephan
T. Tauchnitz
B. Teschome
T. Voitsekhivska
K. Wagner
M. Wang
Y. Wang
R. Wenisch
R. Wutzler
C. Xu
O. Yildirim
Y. Yuan

STUDENTS (diploma / MSc / BSc)

J. Abdou
M. Braun
M. Hähnel
H. Hentschel
N.K. Katkoju
M. B. Khan
K. Manjunath
L. Ramasubramanian

HZDR
HELMHOLTZ
ZENTRUM DRESDEN
ROSSENDORF

Institute of Ion Beam Physics and Materials Research
P.O. Box 51 01 19 · 01314 Dresden/Germany
Phone +49 351 260-2345
Fax +49 351 260-3285
http://www.hzdr.de

Member of the Helmholtz Association